MSc Thesis

Spanwise wall oscillation as a drag reduction technique

Kushal Kempaiah

PIV-based evaluation of turbulent skin-friction drag reduction over a flat plate by spanwise wall oscillation

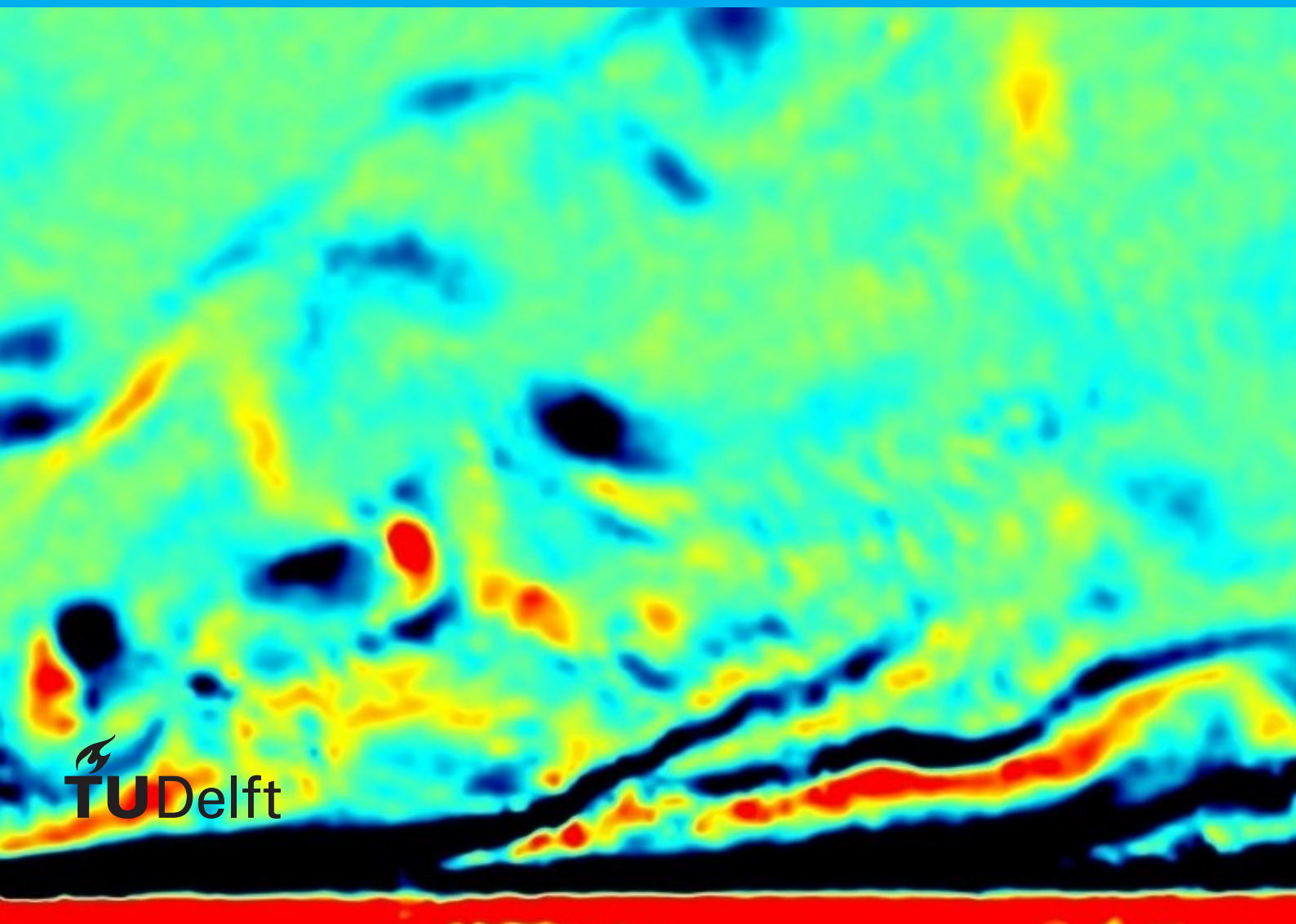

TUDelft

MSc Thesis

Spanwise wall oscillation as a drag reduction technique

by

Kushal Kempaiah

to obtain the degree of Master of Science
at the Delft University of Technology,
to be defended publicly on Wednesday August 28, 2019 at 09:00 AM.

Student number:	4718550	
Project duration:	December 1, 2018 – August 28, 2019	
Supervisors:	Prof. dr. F. Scarano,	TU Delft, supervisor and chair
	Dr. ir. B. W. van Oudheusden,	TU Delft, committee member
	Dr. ir. Gerrit Elsinga,	TU Delft, committee member

TU Delft

Preface

To start, I would like to thank my parents for their constant support, understanding and encouragement. The journey at TU Delft would not have been possible without their sacrifices. My sister *Bharani*, for showing a keen interest in my work, always asking the right, thought-provoking questions. My grandparents in Mandya for their unconditional love and teaching me to appreciate the little things in life and my family for always being supportive.

My thesis has come to an end, and I wish to express my appreciation to *Prof. Fulvio Scarano*, for his supervision, encouragement and advice he has provided throughout the thesis. *Dr. ir. B. W. van Oudheusden* is the next person I would like to thank, for always providing me with the right suggestions and ideas. Also, I would like to thank *Dr. ir. Gerrit Elsinga* for being involved in the project and sharing his expertise in the field which has been important for my current work.

The timely execution of the experiment would not be possible without the help of a great team at the high-speed lab and for that, I would like to thank *Frits Donker Duyvis* for designing and manufacturing the setup which was the heart of the project, *Dennis Bruikman* and *Peter Duyndam* for helping me in manufacturing the parts and helping in assembling the setup and *Nico van Beek, Henk-jan Siemer, Colette Russo* for their assistance.

Thanks to the basement inhabitants (*Valentin, Lucas, Maria, Yuyang, Tomas, Sven, Francesco, Niels, Jorge, Dorian, Kiran*) for keeping the atmosphere lively and conducive for productivity and *Gabriel*, for allowing me to be part of his experimental campaign, which helped me pick up some valuable skills.

I would like to thank all the aerodynamics boys (*Abhinand, Sid, KL, Sampath, Shubham, Athreya, Chakshu, Jatinder*) for making this experience memorable and to the team behind the scenes at 2brokescientists (*Ankith, Akshar, Sanjeet*) for being great roommates, providing the motivation, right amount of criticism and lots of delicious meals.

My gratitude to Yoga uncle and his family for always making me welcome and for the lunches and dinners over the last two years. Thanks to Roger aka *Karthik* for coming out to play tennis every weekend. You have shown that nothing is truly impossible (Well done on the victory). Another mention to all my friends for the great times (*Arya, Ashvij, Rajath, Pooja, Shrutika, Maria, Dimitri, Nick, Joyce, Eirini*). Thanks, *Sahana* for pushing me to experience new things, and not losing faith in my culinary abilities, It truly has been a great experience.

Finally, to the person who has been part of this masters journey at TU Delft from the start, *Nikhilesh*; it's been a great time which I will cherish, you have taught me that there is no substitute for hard work and dedication. Cheers to all the assignments and discussions over the last two years, one of which led us to become the famous science communicators we are today and piqued my curiosity and love for fluids even more. Have fun in Canada and hope you tone down the need to keep your surroundings clean.

Cheers,
Kushal Kempaiah
Delft, August 2019

Abstract

Reduction of skin-friction drag over a fully developed canonical zero-pressure gradient turbulent boundary layer (ZPGTBL) subjected to spanwise oscillation is measured using planar particle image velocimetry (PIV). The experiments are conducted at Re_θ of 1000 and 1800, the chosen range of spanwise oscillations amplitude and frequency are around the optimum reported in literature studies (T^+_{osc} = [100-700], A^+_{osc}= [50, 150]). A high-resolution planar PIV apparatus is employed to measure the drag reduction directly by wall shear stress estimates on the oscillating wall. The measurement uncertainty of the drag estimates from PIV measurements is examined. The results show drag reduction in the order of 15% after 6 boundary layer thicknesses from the beginning of the oscillating section. Variations of the drag reduction follow the trends reported in the literature. The PIV measurements enable the analysis in terms of Reynolds shear stresses, turbulence production and allow visualising vortex packets by vorticity. A pronounced drop of turbulence production in the range y^+ = [5, 30] is observed. The vorticity analysis indicates a distortion from the well-known hairpin-packet arrangement, suggesting that the mechanism of hairpin autogeneration may be inhibited by spanwise wall oscillations.

Contents

List of Figures

List of Tables

Nomenclature

Acronyms

HWA	Hot wire anemometry
PIV	Particle Image Velocimetry
TBL	Turbulent boundary layer
ZPGTBL	Zero pressure gradient turbulent boundary layer

Symbols

δ	Boundary layer thickness
δ^*	Displacement thickness
κ	Von-karman constant
ν	Kinematic viscosity
ω	Vorticity
ρ	Density of the fluid
τ_w	Wall shear stress
θ^*	Momentum thickness
H	Shape factor
M	Mach number
Q_x	Flow rate in the streamwise direction
Re_τ	Reynolds number based on wall friction velocity
Re_θ	Reynolds number based on momentum thickness
Re_x	Reynolds number based on length of the plate, for boundary layer flows
s	Speed of sound
T^+_{osc}	Non dimensionalized time period of wall oscillation
u	Velocity
u, v, w	Velocities along the cartesian coordinate system

U_∞ Free stream velocity

u_τ Wall friction velocity

W_m^+ Non dimensionalized maximum wall velocity

x, y, z Axis of the cartesian coordinate system

y^+ Inner variables scaled wall normal distance

Z_{osc}^+ Non dimensionalized amplitude of wall oscillation

$(\frac{du}{dy})_{y=0}$ Slope of the velocity profile near the wall

1

Introduction

Climate change, rising oil prices and affordable travel for the masses are some of the main drivers of the aerospace sector to develop new technologies to tackle the mentioned obstacles (IATA, 2018). The aviation industry has seen improvements in all its sectors starting from propulsion where better and more efficient geared turbofan engines are being used for their high fuel efficiencies and reduction in noise levels (Sheridan et al., 2010). Battery-powered aircraft are being considered as an alternative to the conventional fossil fuel-based propulsion. The design of structures and materials being used has received considerable attention with new composites being developed which offer improved strength to weight ratio when compared to conventional materials (Jeff, 2007). Air traffic management and scheduling are being optimized for maximum efficiency in terms of flying time and expenditure for the companies to stay profitable (SESAR, 2018). Apart from all this, the aerodynamic drag of aircraft is one of the main sources of fuel consumption and has received considerable attention (Schrauf, 2005).

Aerodynamic drag can be defined as the force that is exerted on a moving object by the surrounding fluid which opposes its motion. For subsonic flows with a Mach number (M)[1] less than 1, the drag on objects can be broadly classified as

1. Skin-friction drag: is the opposing force exerted on the object by the fluid that is close to its surface or in other words the boundary layer. The boundary layer can be described as a thin region close to the wall where velocity increases from zero[2] to a finite value corresponding to free stream velocity. In this region the flow is dominated by the effects of viscosity and the shear stress generated at the wall (τ_w) is the primary source for skin-friction drag.

2. Pressure drag: the boundary layer, tends to separate when the flow over a body creates an adverse pressure gradient due to its curvature. This causes the boundary layer to separate, leading to the formation of a low-pressure region behind the body called the wake. The force experienced due to this pressure distribution which opposes the motion is called pressure drag.

[1] Dimensionless quantity representing the ratio of flow velocity (u) to the local speed of sound (a).
[2] Due to the no-slip boundary condition

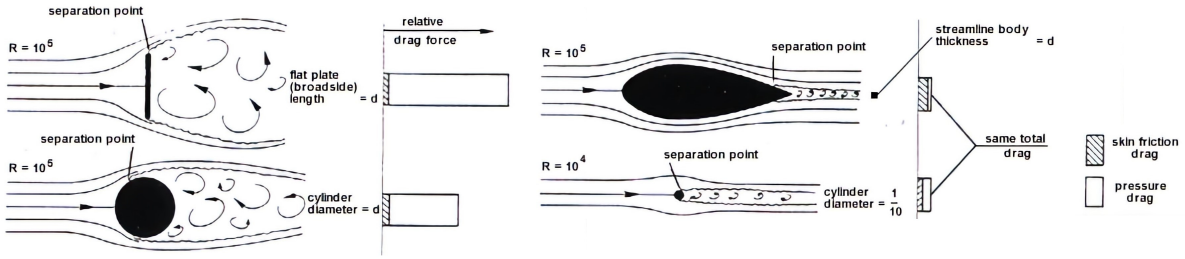

Figure 1.1: Contribution of skin-friction and pressure drag for different objects (Anderson Jr, 2010)

From Figure-1.1 it is clear that the contribution of skin-friction drag is more for streamlined objects like an airfoil where the flow tends to stay attached longer. Whereas, pressure drag is more for bluff bodies as they are prone to separation because of the high adverse pressure gradient. But it is important to note that both skin-friction and pressure drag accompany each other for flows around all objects. Skin-friction drag accounts for up to 50% of the drag and therefore fuel consumption of modern aircraft's (Schrauf, 2005), see Figure-1.2.

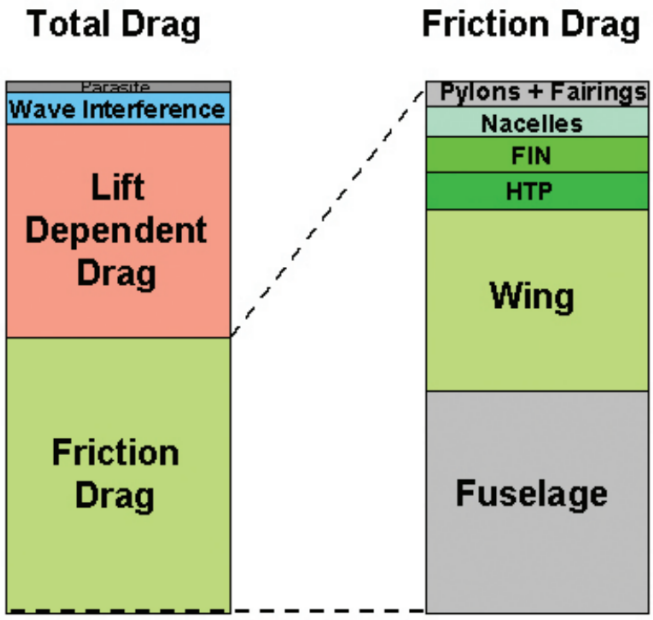

Figure 1.2: Drag contribution in a transport aircraft (Schrauf, 2005)

It is therefore imperative to understand the origins of this drag to be able to develop techniques to curtail it. As mentioned skin-friction drag arises due to the boundary layer, in which the flow can be laminar or turbulent. Turbulence is sometimes incorrectly termed as random fluid motion. However, it does have a degree of coherence that is associated with it as described from the works of Theodorsen (1952), Kline et al. (1967), Robinson (1991) and others (see Figure-1.3).

> *"Randomness is an admission of ignorance that should be avoided whenever possible"* -Voltaire(1764)

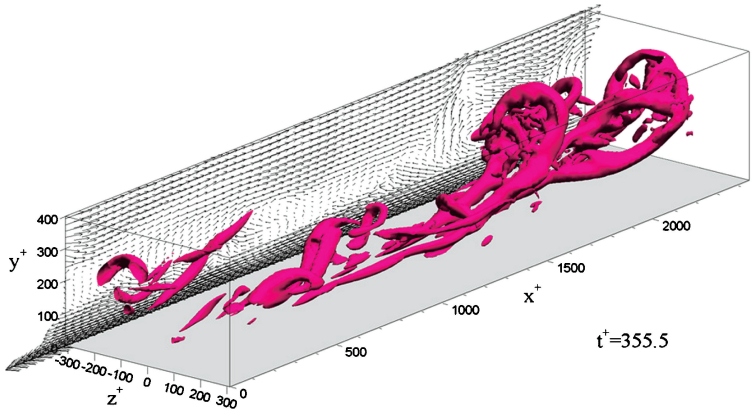

Figure 1.3: Chaotic packet of hairpins that evolves from an ejection event in a turbulent channel flow at $Re_\tau = 395$ (Adrian, 2007)

A direct consequence of turbulence in a boundary layer is turbulent skin-friction drag. Turbulent boundary layers (TBL)[3] due to its characteristics described in Chapter-2 produce more skin friction drag than its laminar counterpart. It is, therefore, necessary to develop techniques to curtail the negative impacts of skin friction drag. The consequences are not limited to the aerospace industry but rather far-reaching from pipe flows, automobiles, ships and any case where a there is relative velocity between a moving surface and the fluid.

Several studies attempting to control turbulent drag, have approached the problem using both passive and active techniques described in detail in Chapter-3. Among the active techniques discussed is spanwise wall oscillation, it involves oscillating the wall in the spanwise direction over which the turbulent boundary layer is present, more details about the current literature is provided in Chapter-4. Although the technique has already shown to produce reductions in skin friction drag, it is of practical relevance to study if Particle image velocimetry (PIV)[4] as a measurement technique, can be used to measure the reduction in skin friction drag.

Current experimental and numerical campaigns have been performed at relatively low Reynolds number (Re_τ) (Quadrio and Ricco, 2004). Experiments reported in the literature have widely employed hot wire anemometry (HWA), given the high accuracy, spatial and temporal resolution and the ease of placement along the wall-normal direction. Knowledge of Reynolds stresses would require X-wire probes and for the study of the velocity gradient (e.g. vorticity) several probes should be arranged to form an array. Studies with these types of arrangements have not been conducted, presumably due to the complexity of the apparatus.

To overcome the shortcomings described, an experimental setup is designed and manufactured to perform PIV measurements on a zero pressure gradient turbulent boundary layer (ZPGTBL)[5]. The apparatus used along with the data acquisition and reduction techniques are detailed in Chapter-5. Instantaneous field data can be obtained with particle image velocimetry (PIV), which delivers quantitative information on some components of the Reynolds shear stress tensor and the spanwise component of the vorticity vector.

[3]Hereafter referred to as TBL
[4]Hereafter referred to as PIV
[5]Hereafter referred to as ZPGTBL

Despite the incompleteness, these properties describe relevant processes in the boundary layer such as turbulent kinetic energy production and rate of shear. Provided that the spatial resolution matches the scale of the viscous layer, the PIV technique can be employed to measure the local wall shear. Moreover, an alternative approach to the measurement of skin-friction drag through the wall-shear is that of monitoring the momentum deficit across a chosen control-volume that encompasses the region of spanwise oscillations.

The present study investigates the applicability of planar PIV to detect skin friction drag reduction over a spanwise oscillating wall. The drag estimates are obtained by two different data reduction techniques: the near-wall velocity gradient yields an estimate of the wall shear; a control volume approach monitors the difference between the momentum at inflow and outflow. The results obtained through the experiment are detailed in Chapter-6. The velocity and vorticity visualisations are used to infer the large-scale organisation of the turbulent structures, with focus on hairpin packets and the modifications incurring when spanwise oscillations induce drag reduction. The relevant conclusions and recommendations for future work are provided in Chapter-7.

The findings and explanation will be provided in the right-hand coordinate system, where the x, y and z axis are chosen as the direction of free stream, wall-normal direction i.e. $y = 0$ at the wall and z being the spanwise direction respectively. The corresponding components of the velocity vector $\mathbf{V}$ are u, v and w.

2

Boundary layer turbulence

The boundary layer is a thin region of fluid flow close to the wall where the velocity increases from zero to a finite value corresponding to free stream velocity ($0.99U_\infty$). In Figure-2.1, uniform flow of fluid encounters a flat plate and a boundary layer starts to develop and grows in thickness as the flow progresses in the streamwise direction (x). This growth is because the effect of viscosity is transmitted (diffuse) to subsequent layers of the fluid.

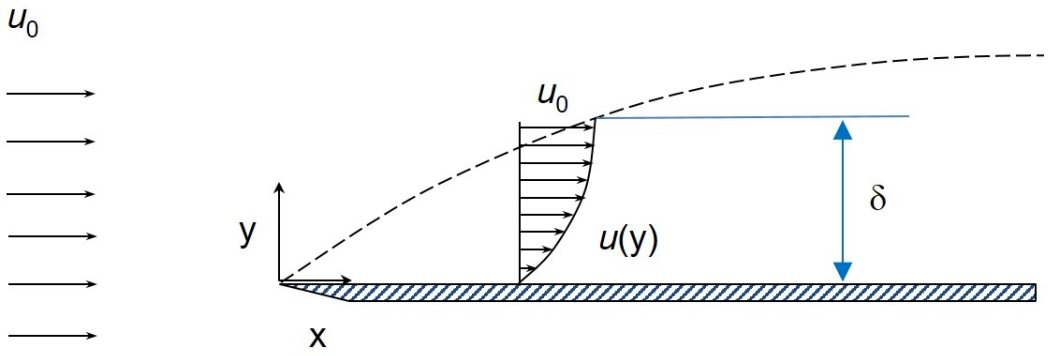

Figure 2.1: Schematic of a boundary layer over a flat plate at zero incidence (Schlichting and Gersten, 2016)

Fluid flow in the boundary layer can be either laminar or turbulent. In a laminar boundary layer, the flow is layered, meaning, that there is an exchange of mass and momentum only between the adjacent layers of the fluid. Whereas in a turbulent boundary layer, the exchange of mass and momentum is not layered anymore and there is an exchange across several layers of the fluid flow. The expression of shear stress at the wall (τ_w) is given by equation-2.1.

$$\tau_w = \mu\left(\frac{\partial u}{\partial y}\right)_{y=0} \tag{2.1}$$

A consequence of the exchange of mass and momentum across several layers is that the velocity profile of a turbulent boundary layer is fuller in comparison to its laminar counter-

part seen in Figure-2.2. This means the velocity gradient at the wall $\left(\frac{du}{dy}\right)_{y=0}$ is higher for a turbulent profile which translates to greater shear stress at the wall from equation-2.1.

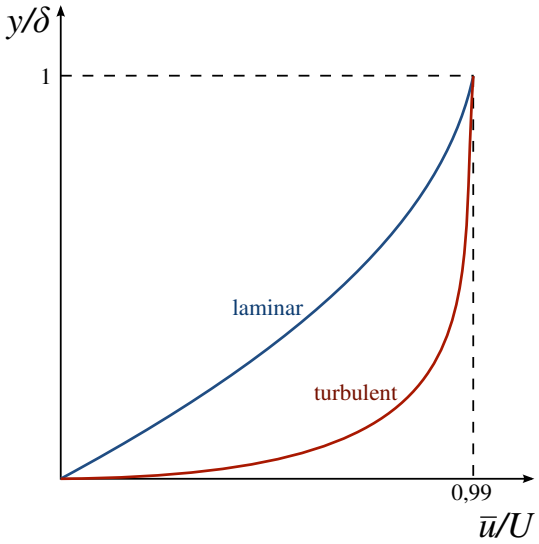

Figure 2.2: Laminar and turbulent velocity profiles, for illustration

The behaviour of a boundary layer over a flat plate is governed by a non-dimensional number called Reynolds Number (Re_x) which is defined as $Re_x = \frac{u_\infty x}{\nu}$, where x is the distance from the leading edge of the plate, u_∞ the freestream velocity and ν the kinematic viscosity. The critical value of Re_x after which the boundary layer can be considered as turbulent is 5×10^5 (Schlichting and Gersten, 2016). Flow behaviour in channel flows on the other hand is dependent on $Re_\tau = \frac{u_\tau . h}{\nu}$, where u_τ is the wall friction velocity defined by $u_\tau = \sqrt{\frac{\tau_w}{\rho}}$ and h is the jet half-width. The regimes of flows which are of interest in many real-life applications can to a good extent be considered as turbulent and from now only turbulent boundary layers will be referred. A boundary layer, whether laminar or turbulent, can be described using the following parameters, whose understanding is of paramount importance for this study.

- Boundary layer thickness (δ) : is the distance from the surface where the relative velocity is zero, to a point in the flow field where the velocity is $0.99 u_\infty$. The effects of viscosity decrease asymptotically to zero as the distance from the surface increases. This implies that the flow field can be divided into two regions, one, where viscosity is dominant and the other where the flow can be considered inviscid.

- Displacement thickness (δ^*): is defined using conservation of mass, δ^* is the distance by which the surface or the wall has to be moved in the direction perpendicular to its normal vector in an inviscid fluid stream to have the same deficit of mass flux as that in a boundary layer.

$$\delta^* = \int_0^\infty \left(1 - \frac{u(y)}{u_\infty}\right) dy \tag{2.2}$$

- Momentum thickness (θ^*): is defined in terms of conservation of momentum flux, θ^* is the thickness of an inviscid fluid flow with velocity u_∞ which has its momentum flux equal to the deficit of momentum flux through the boundary layer.

$$\theta^* = \int_0^\infty \frac{u(y)}{u_\infty}\left(1 - \frac{u(y)}{u_\infty}\right) dy \tag{2.3}$$

- Shape factor (H): the ratio of the displacement thickness (δ^*) to momentum thickness (θ^*) is defined as the shape factor. Typical boundary layer shapes have known shape factors which can be used to identify the type of boundary layer, i.e. $H = 2.59$ for a laminar (Blasius) profile versus $H = 1.3$–1.4 for a turbulent profile.

2.1. Scaling in turbulent boundary layer

Boundary layers fall under the regime of similarity flows, this means the spatial coordinates and velocity can be scaled either by inner or outer variables. Inner variable (ν, u_τ) scaling considers the lower values associated with the spatial and velocity information in the boundary layer. The use of outer variables(δ, u_∞) in scaling will lead to these properties being very small and is not enough to extract the necessary information. The scaling is achieved using inner variables as follows.

$$y^+ = \frac{y u_\tau}{\nu} \quad \mathbf{V}^+ = \frac{\mathbf{V}}{u_\tau} \tag{2.4}$$

where ν is the kinematic viscosity and u_τ is the wall friction velocity defined as $u_\tau = \sqrt{\frac{\tau_w}{\rho}}$ where τ_w is the wall shear stress explained in Equation-2.1 and ρ being the density of the fluid. A turbulent boundary layer over a flat plate is depicted in Figure-2.3. The corresponding velocity profile can be divided into two regions where the velocity is dependent on different parameters.

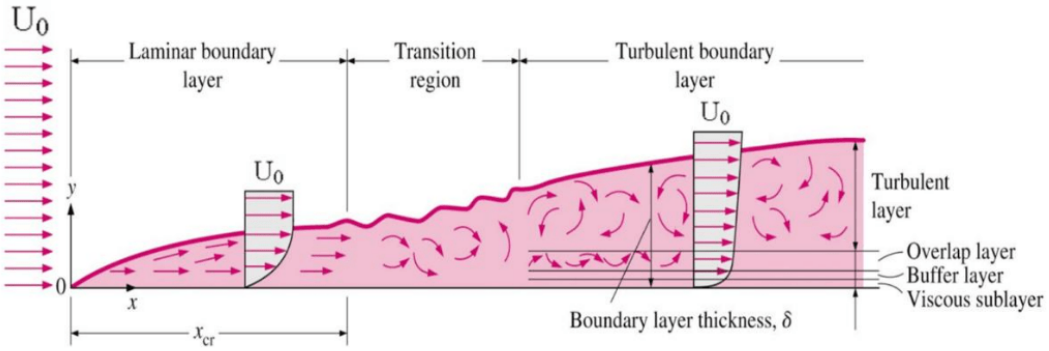

Figure 2.3: Laminar and turbulent boundary layer (Cengel, 2010)

- Inner layer ($y/\delta < 0.1$): Mean streamwise velocity ($\bar{u}$) is a function of τ_w, ρ, μ, y. The equation obtained upon non-dimensionalizing the velocity is $u^+ = f\left(y^+\right)$.

- Outer layer ($y/\delta > 0.1$): where $u_\infty - \bar{u} = g\left(\tau_w, \rho, \delta, y, \frac{dp_\infty}{dx}\right)$ and the resultant expression on non-dimensionalizing the velocity is $\frac{u_\infty - \bar{u}}{u_\tau} = g\left(\eta, \xi\right)$. where $\eta = \frac{y}{\delta}$ and ξ relates to the pressure gradient.

The inner region is also further subdivided into the following layers based on the non-dimensional wall units (y^+).

- Viscous sublayer ($y^+ < 5$): The corresponding velocity profile for the inner scaled velocity is $u^+ = y^+$.
- Buffer layer ($5 < y^+ < 30$): An analytical expression for the dependence of u^+ with y^+ is not defined.
- Logarithmic layer ($y^+ > 30$): The region where that outer and inner layer overlap and both sets of equations need to be satisfied, also called as overlap region.

For the two regions of the velocity profile described, the equations can be satisfied only with a logarithmic expression, which for inner layer is obtained as

$$u^+ = \frac{1}{\kappa}\ln(y^+) + B \tag{2.5}$$

where $\kappa = 0.41$ is the von-Karman constant and B is a constant which accommodates for the wall conditions. For the outer layer, the resulting expression is

$$\frac{u_\infty - \bar{u}}{u_\tau} = -\frac{1}{\kappa} ln\left(\frac{y}{\delta}\right) + A(\xi) \tag{2.6}$$

A is a constant which depends on the external flow conditions like pressure.

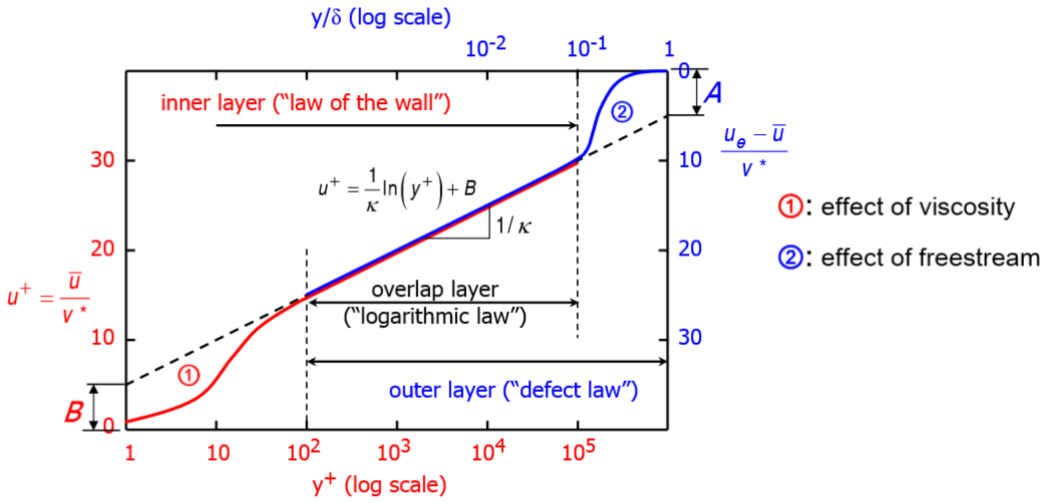

Figure 2.4: Scaled velocity profiles (van Oudheusden, 2017)

The velocity profiles corresponding to the different layers are shown in Figure-2.4 with the inner and outer scaling along with all the layers. This is a good description for a boundary layer and the values from these expressions are used to compare with the experimental data for validation. The flow in a fully developed turbulent boundary layer is unsteady, this unsteadiness is due to the presence of small-scale fluctuations and coherent structures. A more detailed analysis of the coherent structures is performed in the following section.

2.2. Coherent structures in wall-bounded turbulent flows

The energy cascade in a turbulent boundary layer is defined as the transfer of energy from large scales of motion (free stream) to the small scales, which is then dissipated by the smaller scales due to viscosity. This transfer of energy from the higher to lower scales is called an energy cascade. This transfer of energy is a self-sustaining property of a turbulent boundary layer. To get an understanding of this self-sustaining process, research has been done on the internal structure of turbulence. In the early years (1910-1930) of turbulence research, statistical analysis was the most common, where fluctuations in velocity field were superimposed on the mean-field. But statistics did not provide a complete view of the quasi-periodic patterns that are associated with the coherent structures in the flow. From the 1960s, contemporary studies gained interest and research on coherent structures began. These coherent motions play a vital role in maintaining the energy cascade. It is therefore imperative to obtain a clear understanding of the structures. Turbulent boundary layer flows are very common in engineering applications and for developing techniques which reduce skin friction drag.

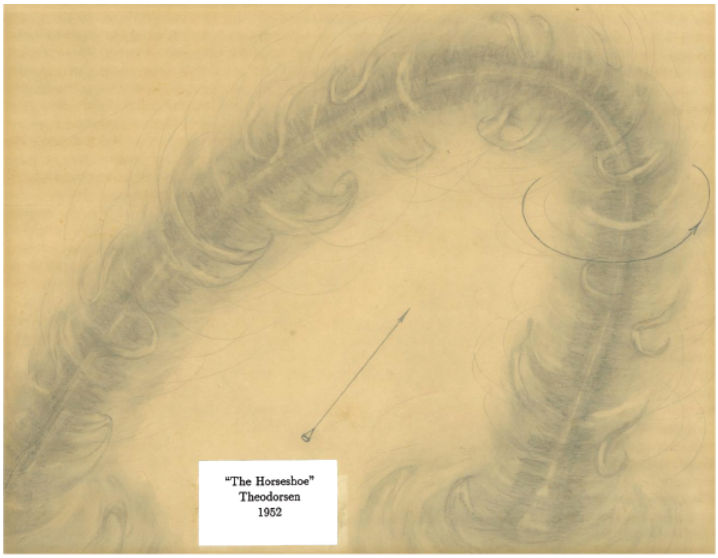

Figure 2.5: Depiction of a horseshoe vortex (Theodorsen, 1952)

Current knowledge on turbulence structures is from studies at relatively low Reynolds number when compared with real-life applications. Many parameters can be varied which affect the turbulent structures, like the curvature of the surface, pressure gradient etc. But this review deals with one of the most simplified cases, i.e. a flat-plate turbulent boundary layer subjected to zero pressure gradient. Most of the discussion in this chapter will be done with respect to this simplified case. The measurement technique used to observe the turbulent boundary layer plays a vital role in the structures that are seen. This has led to a wide variety of structures which have been reported in the literature. To remove the ambiguity, Robinson (1991) classified these coherent motions into classes which are stated as follows.

- Near wall low-speed streaks
- Ejection of low-speed fluid outward from the wall.

- Sweep of high-speed fluid inwards towards the wall.
- Vortical structures of various forms.
- Near-wall shear layers, exhibiting local concentrations of spanwise vorticity.
- Near-wall "pockets," visible in the laboratory as regions swept clean of marked near-wall fluid.
- Large scale motions capped by three-dimensional bulges in the outer turbulent interface.
- Shear layer (backs) of large-scale outer-region motions, consisting of sloping (δ-scale) discontinuities in the streamwise velocity

2.2.1. Development of near-wall turbulent structures

In wall-bounded flows a boundary layer exists near the wall. Due to its varying profile $u(y)$, each layer can be considered as a line of iso-vorticity in the spanwise direction ($\omega_z = \partial u/\partial y$). In an ideal world sans of a disturbance in the free stream and roughness of the surface, the boundary layer would be laminar. But due to these disturbances or perturbations which are unavoidable, the velocity profile gets disturbed, causing these lines of iso vorticity to curl/lift, leading to an initial formation of horseshoe or hairpin vortices. The head of these vortices gets pushed up due to the high-speed fluid and is convected faster, this causes the elongation in the legs and neck of the hairpin, thereby increasing its vorticity. This causes lower speed fluid to be pumped up from between the legs of the hairpin and high-speed fluid to be pushed in from the other side of the leg. This takes place until the head of the hairpin, bursts and the cycle continues. This cycle of a hairpin gives rise to varied structures near the wall and away from it. A clear illustration is provided in Figure-2.6

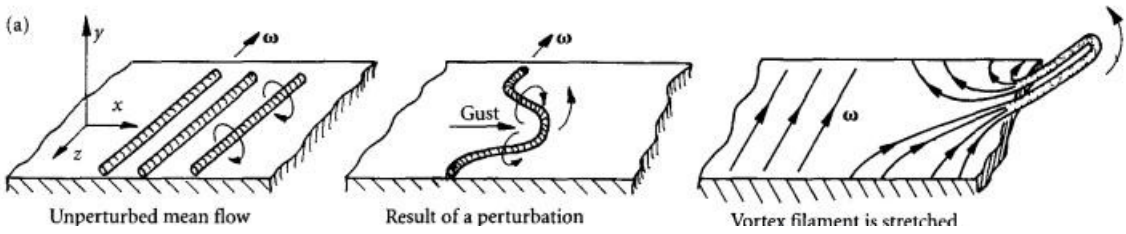

Figure 2.6: Development of hairpin in turbulent boundary layer (Davidson, 2004)

As mentioned in Section-2.1, a turbulent boundary layer can be classified as the inner and outer layer. Structures in the inner and outer layer will be discussed separately.

2.2.2. Structures in inner region

Kline et al. (1967), through their flow visualization experiments using hydrogen bubbles in a turbulent boundary layer, observed well-organized motion in the near-wall region. Very close to the wall ($y^+ = 2.7$), there is an organization of alternating high and low-speed regions which are unsteady and are aligned in the streamwise direction called streaks, shown in Figure-2.7. These streaks in the inner layer interact with the outer layer through the process of lift up, sudden oscillation and breakup.

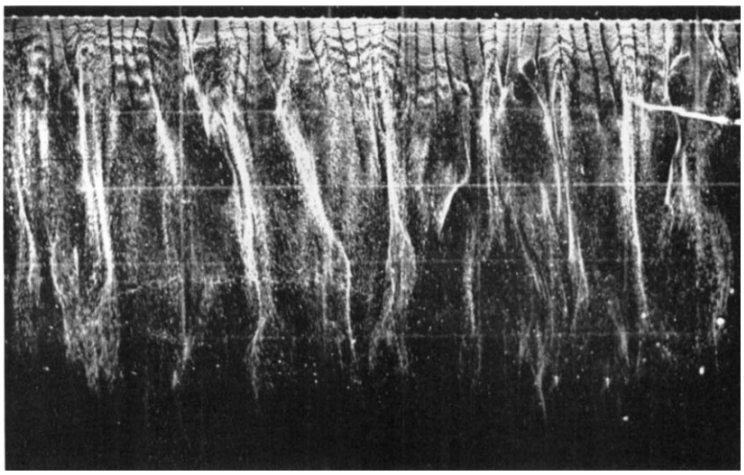

Figure 2.7: Streaks at $y^+ = 4.5$ (Kline et al., 1967)

This cycle of events is termed as the bursting process. Bursts are essential in the production of turbulent kinetic energy (TKE) and the transfer of energy between the outer and inner layer. Figure-2.8 depicts the production of turbulent kinetic energy as a function of the distance from the wall. About 50% of the total production happens in the region very close to the wall. Outer 80% of the boundary layer and the wake contribute close to 20% of the total production (Kline et al., 1967).

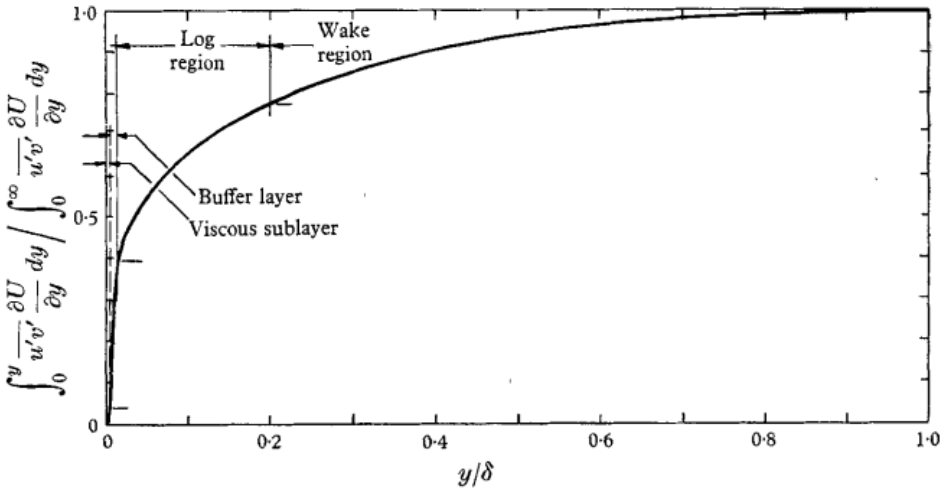

Figure 2.8: Production of TKE in a boundary layer (Kline et al., 1967)

The streak spacing is around 100 wall units (y^+) and is one of the most well-accepted numbers in turbulence. In the streamwise direction, the streaks extend up to 1000 wall units. The presence of the streaks near the wall is attributed by some authors to the pairs of counter-rotating vortices aligned in the streamwise direction (Ersoy and Walker, 1985). Panton (1997) stated that the current concept is that, relatively short streamwise vortices are convected over the wall, bring up the low-speed fluid and leave it behind in the long trails. The presence of these streamwise vortices can be observed as the legs of the hairpin vortices described in Section-2.2.1. Streaks are also considered as one of the coherent struc-

tures in a turbulent boundary layer. But streaks are not prominent away from the wall as many vortices with different scales, strengths and orientation appear. The takeaway is that streaks are more predominant in the inner layer and many vortical structures are present in the outer layer.

2.2.3. Structures in outer region

A common structure in the outer layers are the turbulent bulges having a length of order 2–3δ. The bursting process directly plays a role in the occurrence of large-scale motion in the outer layer.

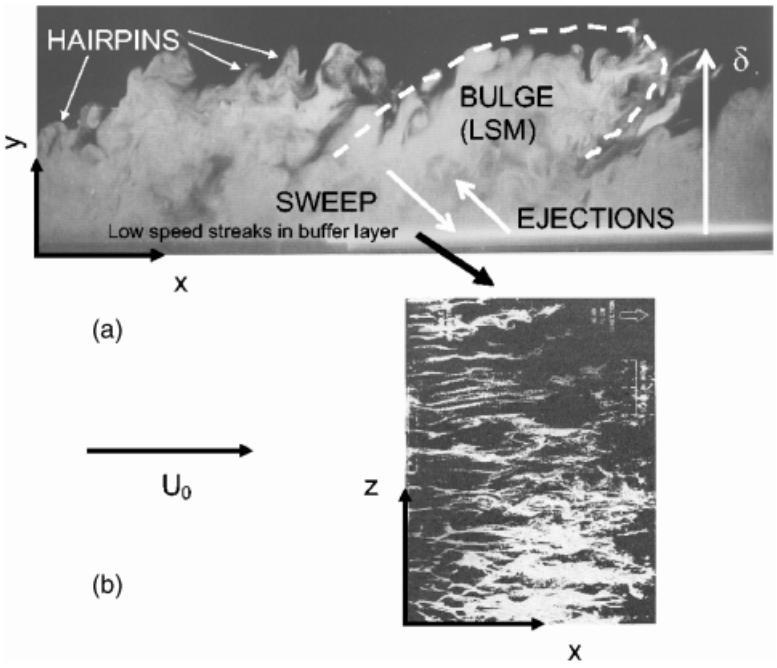

Figure 2.9: Turbulent bulges (Falco, 1977) and the streaks from Kline et al. (1967) and Adrian (2007)

The outer layer behaviour can be explained as follows, the turbulent bulges with the dimensions in the order of boundary layer thickness occur at the interface of the free stream and the boundary layer flow. Due to these bulges, the free stream fluid is entrained in the turbulent region. This high-speed fluid now impinges on the upstream bulge to create shear layers, leading to the formation of vorticity which is transmitted to the smaller scales. Also at high Reynolds numbers, structures identified as 'super-streaks' are present in the outer regions of the turbulent boundary layer, which interact with the near-wall streaks in the viscous sublayer (Hutchins et al., 2011).

2.2.4. Vortical structures

The discussions of the inner and outer layer structures are not complete without vorticity. Vorticity plays an important role in the understanding of the phenomena occurring in a turbulent boundary layer. A vortex is also a coherent structure, Robinson (1991) defined it as *"... feature of the flow such as the instantaneous streamlines projected on a plane normal to the vortex core exhibit a roughly circular or spiral pattern when viewed from a*

reference frame moving with the center of the vortex core ...". In other words, the tendency of a fluid to rotate about a center is called vorticity and is given by the curl of the velocity field $\left(\vec{\omega} = \nabla \times \vec{U}\right)$.

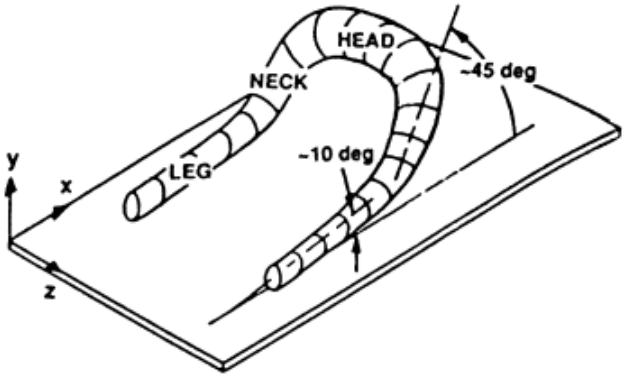

Figure 2.10: Sketch of a hairpin vortex (Adrian, 2007)

Theodorsen was one of the first to discuss vortices in a boundary layer and introduced the concept of a hairpin (horseshoe) vortex shown in Figure-2.5 and 2.10. A brief description of Theodorsens view is provided in Section-2.2.1. Robinson (1991) confirmed the existence of these structures through DNS results. The vortices that were detected were all not symmetric but both arches and streamwise vortices were observed. The vortices near the wall are closely related to the streaks that are observed. The legs of these vortices lead to the creation of these streaks as shown in Figure-2.11.

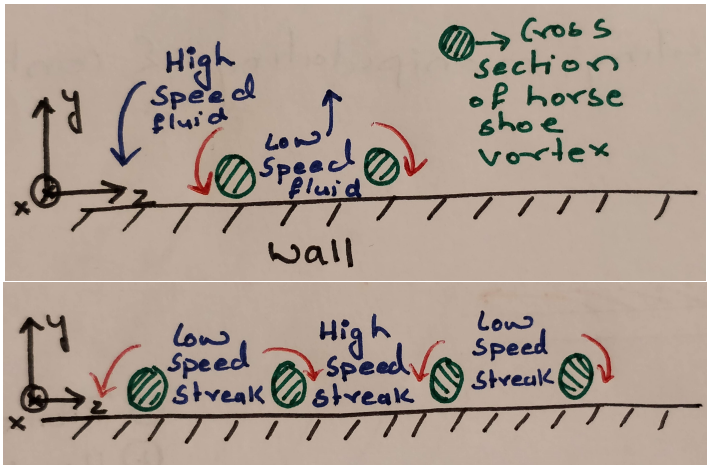

Figure 2.11: Cross sectional view of streak formation from the legs of the hairpin

Streaks are formed from all kinds of hairpins, i.e symmetric or asymmetric. But streaks will initiate only if a vortex is advected sufficiently close to the wall or a vortex leg penetrates through vortices of all other kinds, reaching the proximity of the wall. But if these vortices are not close to the wall the streaks will disappear due to viscosity. Streaks are also observed to meander, this is because of the vorticity in the wall-normal direction. Streaks near the wall are more dormant when compared to that of streaks that are lifted, this can

be observed in the Figure-2.12 where the streaks at $y^+ = 2.5$ weaver less than compared to that at $y^+ = 100$.

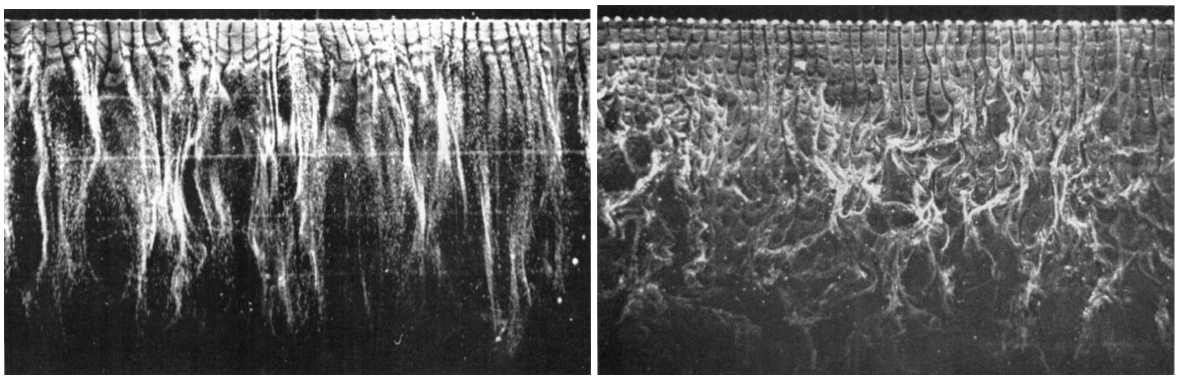

Figure 2.12: Comparison of streaks at $y^+ = 2.7$ and 100 (Kline et al., 1967)

As mentioned, the near-wall region is subjected to bursts, where the vorticity close to the wall is ejected outwards in this turbulence production mechanism. These ejections lead to the formation of shear layers ahead of it and these successive roll-ups create new hairpin vortices. The bursts are followed by sweep events where the high-speed fluid penetrates to regions close to the wall-this is a consequence of continuity. The bursts and sweep events are symbolic to any turbulent flow. The probability density function of the u and v fluctuations of a 2-dimensional turbulent channel shown in figure 2.13, allows evaluation of the contributions these events make to the total mean values of various quantities such as kinetic energy, dissipation, etc.

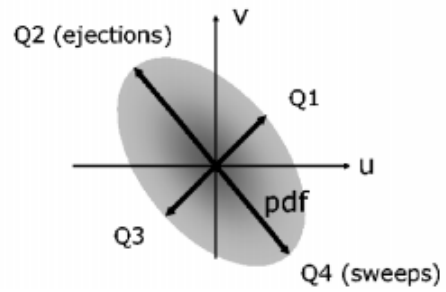

Figure 2.13: Probability density function of a 2D turbulent channel flow (Adrian, 2007)

The take away from this discussion is that all the coherent structures that occur in a turbulent boundary layer are interdependent. Starting from the structures near the wall and the ones that lie in the outer region. Changes either made to the large scales or the small scales will inevitably have an impact on the other. Because of the lack of a general theory of turbulence, a complete understanding of all the interactions is still not available. But, research is ongoing and pieces of the puzzle that is turbulence are coming together.

3

Turbulent drag reduction

The approach undertaken in turbulent boundary layer drag reduction techniques is to break the coherence of structures discussed in Section-2.2. Various techniques, both passive and active, have been investigated and implemented. Passive flow control techniques involve using geometric modifications which are always operational. Active flow control, on the other hand, imparts energy into the flow to obtain desirable characteristics. Unlike passive flow control techniques, active flow control is made operational only when required. In literature two broad techniques are used in turbulent drag reduction, them being

- Outer scale control: control technique which deals with the influence of outer-layer large-scale structures on the near-wall turbulence generation mechanism.
- Inner scale control: control technique which deals with the influence of near-wall mechanisms.

The following section will provide an insight into the various techniques for turbulent drag reduction which will be a good precursor to the technique used in this study, which is spanwise wall oscillations, discussed in detail in Chapter-4.

3.1. Large-eddy breakup devices

Large-eddy breakup devices (LEBU) is an outer scale control technique which uses thin flat plates aligned with the primary flow direction suspended at different heights above the wall in a turbulent boundary layer. The mechanism behind this technique is to inhibit wall-normal velocity fluctuations due to the presence of the plates. A schematic representation is shown in Figure 3.1.

Corke et al. (1981) performed flow visualization with the LEBU at various configurations shown in the Table 3.1. LEBU was observed to suppress the large scale events that occur in the boundary layer. The four-plate M-1 configuration produced complete suppression of the large-scale outer structure of the turbulent boundary layer seen in Figure-3.2. The other configurations were also successful in reducing the large scale structure, but it is important to note that minimizing the number of plates is an important factor to achieve net drag reduction. More plates directly relate to more drag that is produced, because of more wetted surface.

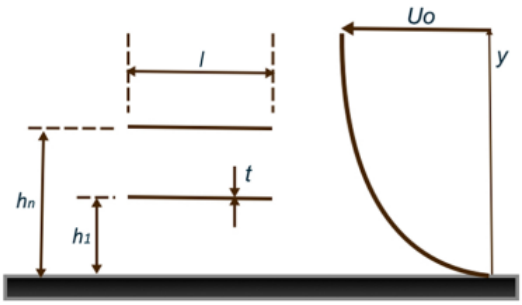

Figure 3.1: Schematic description of LEBU (Corke et al., 1981)

Designation	t/δ	l/δ	h/δ
M-0	-	-	-
M-1	0.002	0.8	0.7,0.4,0.2,0.1
M-2	0.002	0.8	0.6
M-3	0.002	0.8	0.6,0.2

Table 3.1: LEBU parameters (Corke et al., 1981)

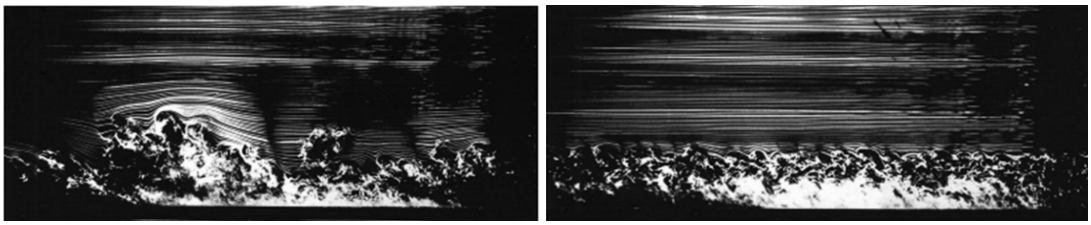

(a) TBL without LEBU **(b)** LEBU M-1 configuration

Figure 3.2: Visualization of LEBU (Corke et al., 1981)

A configuration not shown in Table 3.1, was found to produce a net drag reduction of 20% Corke et al. (1981). Following this, both numerical and analytical studies were performed to understand the underlying mechanisms of LEBU. Dowling (1985) performed a study to understand the effect of the vortex shedding behind the plate and how that impacts the drag reduction. It was found that the shedding from the plate leads to a significant reduction in the fluctuating velocity in the vicinity of the wall. Savill and Mumford (1988) stated that suppression of the large scale motions was indeed one of the mechanisms responsible for drag reduction but the primary reason was due to the interaction of vortices shed by the LEBU with the near-wall structures. Observations which consolidated this position was found when the maximum local drag reduction took place where the wall vortices reached the sublayer. The optimum wall-normal height of the device was found to vary inversely with the Reynolds number. A drawback of this technique is that additional elements need to be added which makes mechanical design and achieving overall drag reduction more complicated. But an understanding of this mechanism can lead to a more innovative design.

3.2. Riblets

Manipulating the near-wall structures to reduce turbulent boundary layer drag has received a lot of attention and riblets are the most common among them. Riblets are passive drag reduction devices which target the near-wall mechanisms. They consist of small v-shaped grooves placed over the surface. Figure-3.3 provides a schematic of these riblets. The two important parameters while designing a riblet are the height h and lateral spacing s of the groove. These are then non-dimensionalised with u_τ and ν to obtain h^+, s^+, the units for height and spacing. Studies have found that the the optimal values correspond to $h^+ = 8-12$ and $s^+ = 15-20$.

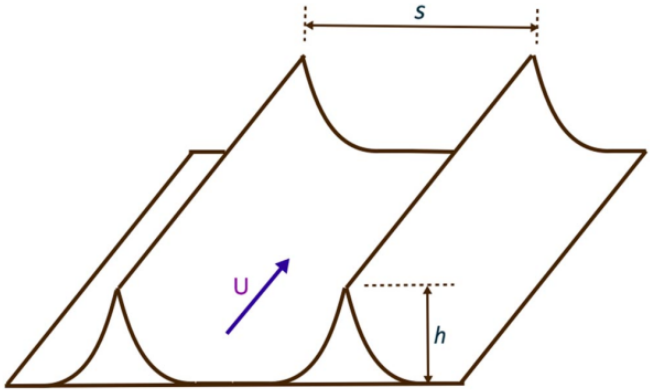

Figure 3.3: Schematic description of riblet (Corke and Thomas, 2018)

Bechert et al. (1997) performed experiments using riblets. The results shown in Figure-3.4 express the drag reduction in terms of change in the wall shear stress $\Delta\tau$, normalized by the actual smooth plate value τ_0 and varying with the riblet spacing(s^+). Optimum spacing is obtained at s^+ of 16 and with an increase in s^+, the drag increases, which is also the expected behaviour with a rough wall turbulent boundary layer.

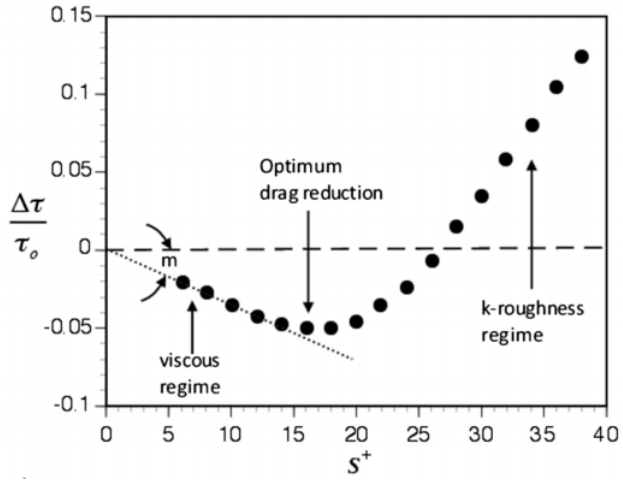

Figure 3.4: Riblet drag reduction as a function of spanwise spacing(s^+) (Bechert et al., 1997)

Several theories that explain the mechanism of drag reduction that is observed in riblets. A common theme that is observed in these explanations is that the presences of ri-

blets break the coherence of streaks, which are the most important structures in the process of turbulence production as explained in Chapter-2. García-Mayoral and Jiménez (2011) reported that vorticity generated in the valleys of riblets interacts with and weakens the coherent streamwise vortices which reduce the intensity of the streaks. Smith et al. (1990) postulated that the riblets interfere with the spanwise (sinuous) motion of the low-speed streaks. Full-scale tests involving riblets have revealed practical issues related to ice, dirt, wear and weight which accumulates on the surface and reduces its effectiveness.

3.3. Dimples

Dimples are very similar to the riblets in the fact that it is an inner scale technique. But have been implemented as both active (van Campenhout et al., 2018) and passive (Van Nesselrooij et al., 2016) mechanisms. The parameter of importance for these dimples is the depth to diameter ratio (d/D) and the portion of the surface covered by these dimples. d/D ratios of below 10% were found to produce drag reductions (Veldhuis and Vervoort, 2009). Various patterns of these dimpled surfaces were experimented as shown in Figure-3.5.

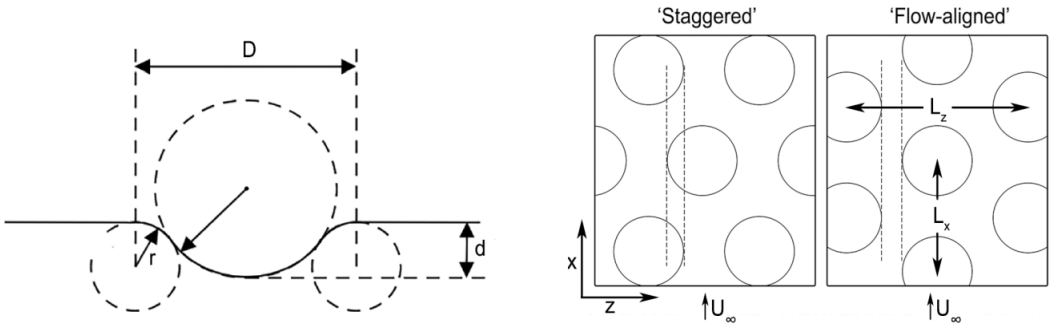

Figure 3.5: Cross sectional view of a dimple and the two patterns of placement (van Campenhout et al., 2018)

Through the study, it is proposed that the obtained drag reduction is due to the presence of spanwise velocity pattern which is caused by the interaction of the dimples of the staggered pattern. Whereas drag reduction was not obtained for the aligned pattern. Drag reduction of up to 4% was obtained from this experimental study. But more experimentation of this technique is required to better understand the effectiveness of this drag reduction mechanism.

3.4. Wall suction and blowing

Suction and blowing have been investigated for obtaining skin friction drag reduction. The action of suction or blowing is aimed at reducing the burst and sweep events which contribute to the Reynolds stress production term. Gad-el Hak and Blackwelder (1989) implemented a single streamwise-oriented suction slot to reduce bursts in a zero-pressure-gradient turbulent boundary layer. DNS studies were performed by Park and Choi (1999) where surface boundary conditions were to suppress dynamically significant coherent motions in the near-wall region. The data from the simulation led to drag reductions between 20 and 30% based on either wall-normal or spanwise wall velocity.

Rathnasingham and Breuer (2003) implemented a linear feed-forward active control scheme using a spanwise array of synthetic pulsed jet actuators located between the streamwise locations with a series of upstream and downstream flow sensors as depicted in Figure-3.6.

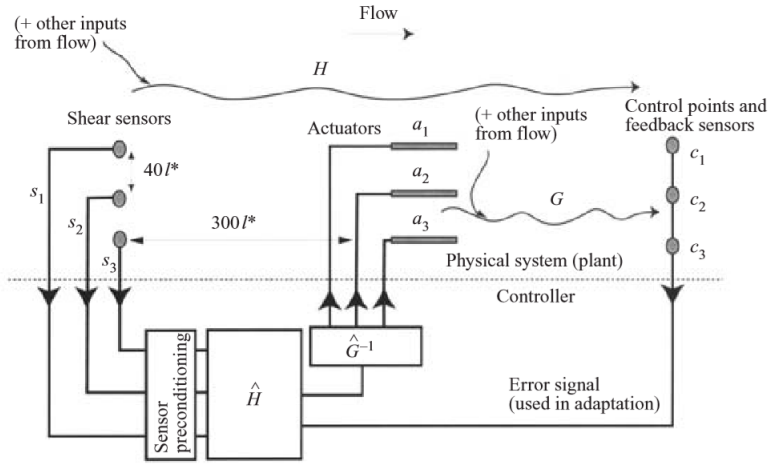

Figure 3.6: Schematic diagram of the setup (Rathnasingham and Breuer, 2003)

The actuator arrays produce streamwise vortices which interact with the naturally occurring near-wall structures similar to LEBU where the vortices from the wake of the thin plates were found to reduce the fluctuation in the velocity near the wall. This technique resulted in a reduction of mean wall shear by 7%. But a clear explanation on the impact of these vortices on the coherent structure is not provided. Another interesting observation was that the linear control scheme was able to provide reductions in the fully nonlinear and chaotic environment of the turbulent boundary layer.

3.5. Polymer additives

Another interesting drag reduction technique is the addition of long-chain polymers in the solvent (water). The presence of these long-chain molecules prevents the turbulent burst events that are observed in a turbulent boundary layer thus reducing the production of turbulent kinetic energy. This interaction of the polymer compounds with the turbulence occurs at $y^+ = 15$. White et al. (2004) performed PIV over a flat plate turbulent boundary layer, where long-chain polymer compounds were present in the solvent. Significant modification of the near-wall structures of turbulence was observed relative to its Newtonian counterpart. The spanwise distance between the low-speed velocity streaks was increased along with a reduction in the strength and number of near-wall vortices. The use of polymers finds application in transporting fluids through pipes over large distances($> 1Km$), where losses due to skin-friction need to be minimized.

3.6. Hydrophobic surfaces

In flows where the fluid is water, the use of hydrophobic coating has received considerable attention. The presence of these coatings causes a slip at the boundary which reduces the shear stress at the wall and leads to a reduction in skin friction drag, shown in figure 3.7. But applying these coatings on large ships is expensive and with the current advances in

nano and microtechnology, it is possible to apply these coatings for small regions (micron lengths). Min and Kim (2004) have performed a study to estimate the minimum slip length which can reduce the skin-friction drag of turbulent flows in much larger devices. But when slip was applied to the spanwise component of the flow, an increase in drag was observed. This is because the streamwise vorticity is increased, which makes the process of turbulent production more enhanced as the streaks become stronger and the number of burst events increases.

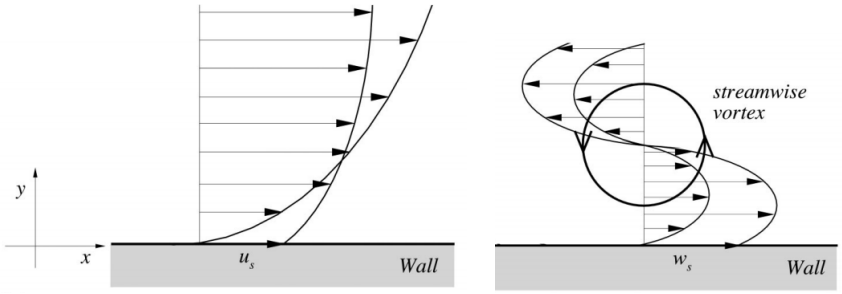

Figure 3.7: Effect of slip in both streamwise and spanwsise direction (Min and Kim, 2004)

3.7. Comments on turbulent drag reduction techniques

From the few techniques discussed for turbulent skin friction drag reduction, it is clear that understanding of the mechanism of interaction between inner and outer turbulent boundary layer structures is very essential in the development of an optimized drag reduction technique. To do so, a very methodological study has to be performed to understand the response of these turbulent boundary layer flows. Hence one can study the time-resolved data through particle image velocimetry of the structure after the disturbance from the drag reduction technique is induced. This kind of experiment can help understand the effect of the smaller scales near the wall to the outer scales in the boundary layer. One of the aims through this thesis will be to understand the effect of the near-wall oscillations on the larger scale events that occur, by obtaining quantitative data downstream of the actuation.

4

Spanwise wall oscillation

Early studies of turbulent boundary layers (Bradshaw and Pontikos (1985), Driver and Hebbar (1987), Sendstad (1992), Eaton (1995), Howard and Sandham (2000)) showed that a fully developed turbulent boundary layer when subjected to sudden spanwise pressure gradient resulted in the reduction of turbulence production and Reynolds stresses. The DNS study of Sendstad (1992) showed that skewing motion is necessary to weaken the quasi-streamwise vortices. After these preliminary studies, it was clear that steady-state reductions in drag can be obtained only due to the unsteady transverse motion of the wall (Touber and Leschziner, 2012). Following which, spanwise wall oscillations received much attention, given the possibility of achieving a significant skin friction reduction. Spanwise wall oscillations involve oscillating sideways the wall where the turbulent boundary layer develops.

Before a detailed description of the literature is provided, some preliminary terms which are a common theme in the subsequent discussion will be explained. The oscillations provided to the wall are sinusoidal. The displacement of the plate is given by the following equation.

$$z = A_{osc} sin(\omega t + \phi) \tag{4.1}$$

where z is the location on a plate which is being oscillated (In accordance with the right-hand Cartesian system described in Chapter-1). A_{osc} is the amplitude of oscillation, ω the angular velocity and ϕ being the phase difference. Amplitude(A_{osc}) and Time period ($T_{osc} = \frac{2\pi}{\omega}$) of oscillation are the two parameters which govern the oscillating system. They are non-dimensionalised with the wall friction velocity (u_τ) and the kinematic viscosity (ν) as follows

$$T^+_{osc} = \frac{T_{osc}.u^2_\tau}{\nu} \quad Z^+_{osc} = \frac{A_{osc}.u_\tau}{\nu} \tag{4.2}$$

and the new units are depicted as T^+_{osc} and Z^+_{osc}. In literature, non-dimensionalized frequency ($f^+ = \frac{f\nu}{u^2_\tau}$ or f^+_{osc}) is sometimes used instead of T^+_{osc}.

4.1. Literature on spanwise wall oscillation

The literature regarding spanwise wall oscillations is classified into experimental and numerical studies. This to done to aid a better comparison between the two data sets. Table-

4.1 contains all the specifications of the boundary layer and oscillation parameters from the literature. The discussion of experimental and numerical results will be followed by a section on the comparison of these data sets to find relevant points of investigation in the thesis.

Direct Numerical Simulation					
Author	T^+_{osc} (Min,Max)		Z^+_{osc} (Min,Max)		Re_θ
Baron and Quadrio (1995)	100(f=6.75Hz)		0.25($\frac{Q_x}{2h}$)	1.0($\frac{Q_x}{2h}$)(35mm)	$Re_\tau = 200$
Jung et al. (1992)	25(27Hz)	200(3.37Hz)	0.8($\frac{Q_x}{2h}$)(28mm)		$Re_\tau = 200$
Experimental					
Author	T^+_{osc} (Min,Max)		Z^+_{osc} (Min,Max)		Re_θ
Laadhari et al. (1994)	10Hz	2Hz	160(25mm)	160(25mm)	950
Choi et al. (1998)	$f = 1,3,5,7Hz$		$\Delta Z = 70mm$ [peak-peak]		1190
Choi et al. (2011)	Depend on $\lambda^+_p, T^+_p, t^+_p$				1000
Gouder et al. (2013)	$f = 42Hz$		$\Delta Z = 4,6,8mm$ [peak-peak]		2430

Table 4.1: Data from literature

4.1.1. Experimental studies

Experimental investigations into spanwise wall oscillation have been performed starting from the works of Laadhari et al. (1994) in a channel whose experimental setup is shown in Figure-4.1. The boundary layer over the plate was tripped by a tripwire placed $3cm$ from the leading edge. Boundary layer details are shown in Table-4.1. Hotwire anemometer was used to obtain quantitative information. The parameters, when converted to dimensional units correspond to a frequency range of $2-10Hz$ and amplitude of $25mm$. The Reynolds number based on momentum thickness (Re_θ) was 950.

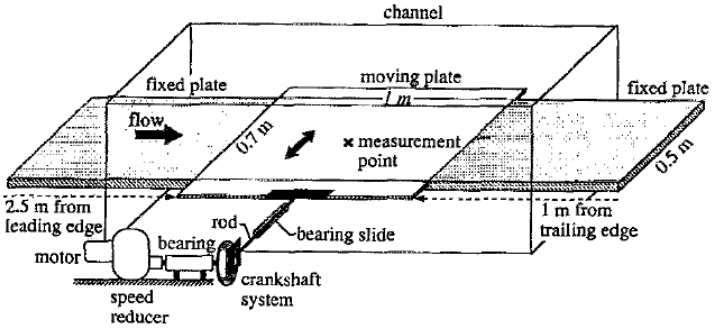

Figure 4.1: Setup used by Laadhari et al. (1994)

The mean streamwise velocity profile (u^+) is reduced when compared to the unperturbed case and also decreased with the increase in the frequency of wall oscillation. This reduction was observed only up to $y^+ < 30$ after which it increased due to the conservation of mass flux. During this study, reductions in the fluctuating components of velocity by

45% in u', 50% in $\overline{uv}$, 34% in v' and 16% in w' were recorded. In addition, the Reynolds stress was observed to be a decreasing function with frequency. Experimental studies of Choi et al. (1998) in addition to measuring the velocity profile and turbulence statistics using hot wire anemometer, skin-friction drag coefficient was also measured which could be used to confirm the findings of the numerical studies being performed. 45% reduction in skin friction drag coefficients were observed for the wall with oscillation (Choi et al., 1998). The graph showing the reductions in C_f over the oscillating plate is shown in figure 4.2a. Although the curve fit is questionable, due to the trend that is depicted. The frequencies at which the wall oscillates for both the campaigns are between 2 and 10 Hz as can be observed from table 4.1. Following these experimental studies, Choi et al. (2011) conducted experiments using plasma actuators which mimicked the spanwise flow that is expected from wall oscillations. The effect of spanwise travelling waves was also studied. Spanwise wall oscillations using the plasma actuator caused a large reduction in the mean velocity for the region $y^+ < 200$. Fluctuations in the oscillating region ($y^+ < 30$), u'^+ was reduced by 36% with an increase in v'^+, w'^+ by 100 and 20%. The configuration implementing spanwise travelling wave, on the other hand, showed weaker reductions in the mean velocity profile.

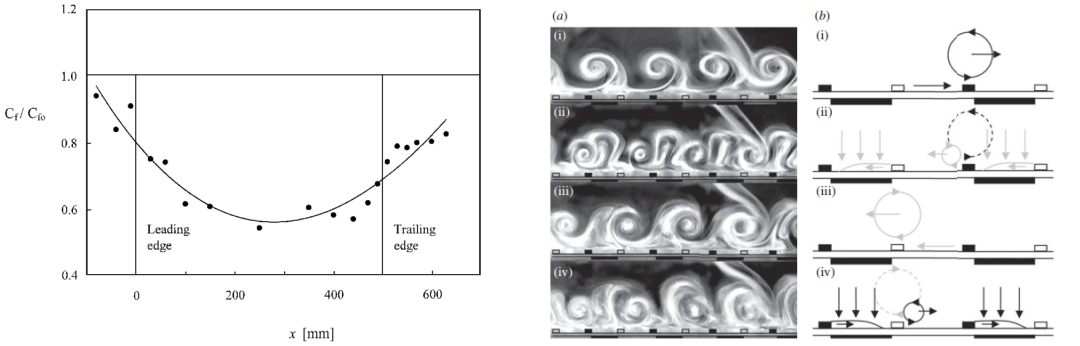

(a) Skin-friction drag Coefficient(C_f) reductionsChoi et al. (1998)

(b) Flow visualisation with plasma actuation Choi et al. (2011)

Figure 4.2: Mechanical wall oscillation and plasma actuation

Recent experimental studies by Gouder et al. (2013) showed the implementation of two spanwise-oscillating surfaces manufactured from electroactive polymers (EAPs) in the dielectric form of actuation and an electromagnetic-driven linear motor. The results obtained were in accordance with the previous studies discussed. A maximum drag reduction of 11.5% was obtained for a frequency of $43.9Hz$ ($T^+_{osc} = 90$) and a peak-to-peak amplitude of $8mm$ equivalent to approximately 130 wall units. In Figure 4.3, all the mean velocity profiles in wall units are superimposed. It should be noted that the data from Laadhari et al. (1994) is non-dimensionalised with the wall velocity from the non-oscillating case whereas that of Choi et al. (1998) is done with u_τ from the oscillating case. It can be observed that the extent of the viscous sublayer is increased up to $y^+ \simeq 10$. The curve of Gouder et al. (2013) also exhibits the same trend and drag reductions are recorded. The plot of Choi et al. (2011) using plasma actuators shows large reductions in the mean streamwise velocity. The wall velocity used for scaling, in this case, is the canonical u_τ. This is because of the core of the vortex from the plasma actuator is at $y^+ \simeq 50$ shown in Figure 4.2b and this leads to low-speed fluid from below $y^+ = 50$ being pumped upwards causing a decrease in the

streamwise velocity. No data was provided on drag reductions. With drag reductions being obtained from literature through experiments, the scaling used by different authors can lead to confusions. A holistic approach to measure drag reduction would then be to measure the momentum deficit in the wake. The need for using the right wall friction velocity can be done away with and drag reductions can be reported with much more conviction.

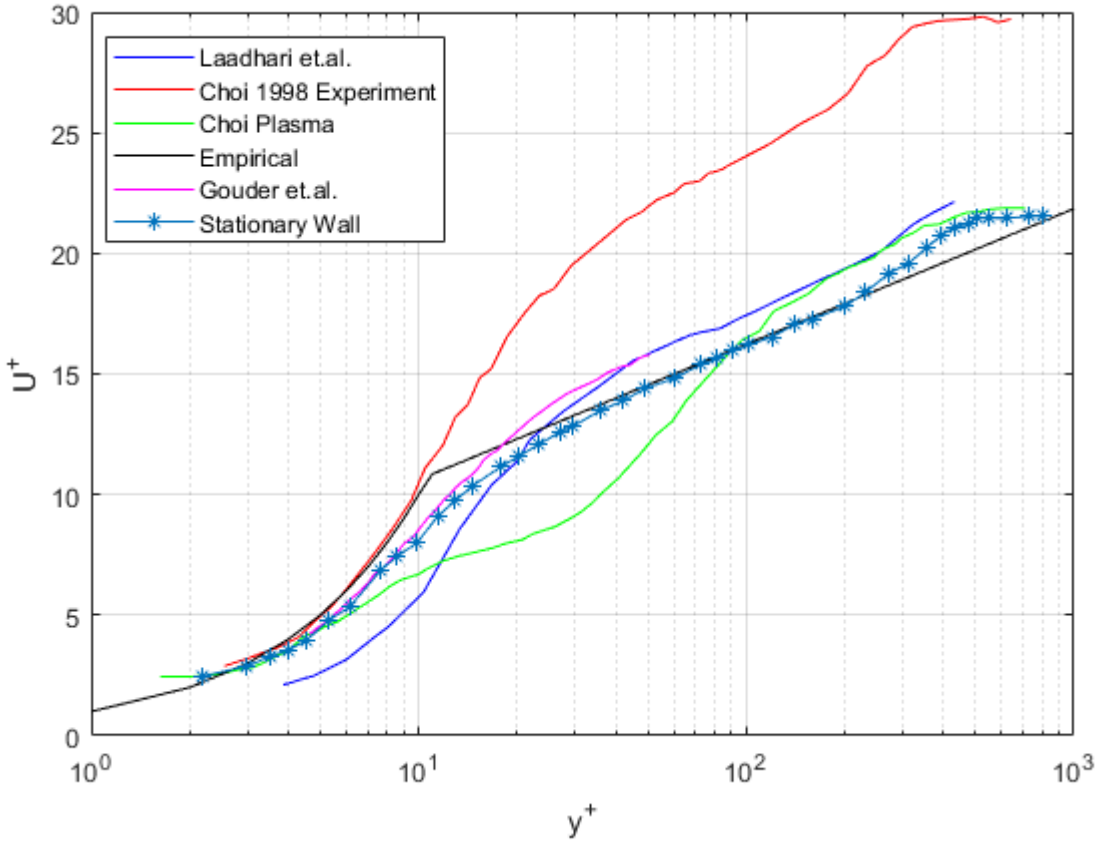

Figure 4.3: Non dimensionalised velocity profiles (U^+ vs y^+) from experimental data

4.1.2. Numerical studies

Jung et al. (1992) conducted the first numerical studies of spanwise wall oscillations in a turbulent channel flow. The oscillations were obtained by superimposing a spanwise cross-flow with specified flow rate except for the 100W case in Figure 4.4a where the wall was oscillated. The specifications of the oscillations are mentioned in Table 4.1, reductions of 40% were observed in wall shear stress for the oscillating wall case shown in Figure 4.4. A reduction in mean streamwise velocity was also recorded with a drop in turbulent fluctuations. The scaling used in the plots is from wall velocity of the unperturbed case.

Baron and Quadrio (1995) took this DNS study forward by analyzing the energy balance of turbulent channel flow subjected to spanwise wall oscillation. The T^+_{osc} of the oscillation was fixed to 100, which corresponds to a frequency of $6.75Hz$ and the effect of amplitude was analyzed on the overall energetic balance. It was found that for an amplitude of $0.25(\frac{Q_x}{2h})$, net positive energy savings were obtained. The inner variable scaled mean streamwise velocity profile when scaled with actual wall velocity shows the behaviour of

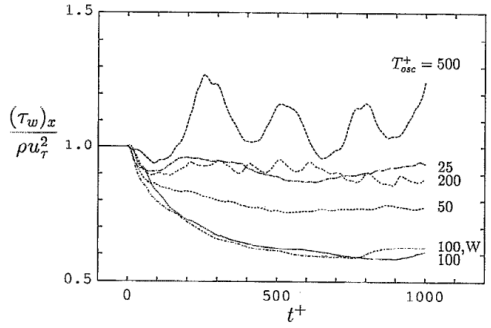

(a) Wall shear stress variation with time

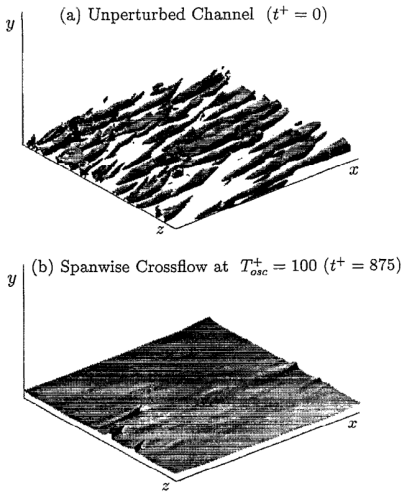

(b) Turbulent structures represented by constant vorticity magnitudes

Figure 4.4: Plots from Jung et al. (1992)

drag-reducing flows. The fluctuations in velocity are also reduced, A more interesting plot from this study is that of the turbulent kinetic energy budget with and without wall oscillation (Figure 4.5).

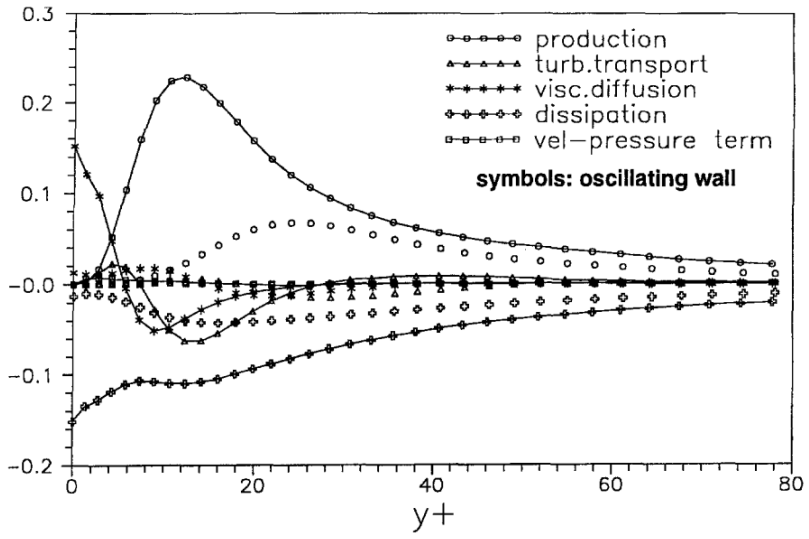

Figure 4.5: Terms in the turbulent kinetic energy budget with and without oscillation (Baron and Quadrio, 1995)

A Reynolds number (Re_τ) of 140 is set to enable a detailed visualization. Quadrio and Ricco (2004) then performed a critical analysis of the spanwise oscillation numerically. Both T^+_{osc} and Z^+_{osc} are varied and all drag reductions are recorder, figure 4.6 gives a complete overview of the reductions obtained. This study is performed at Reynolds number(Re_τ) of 200.

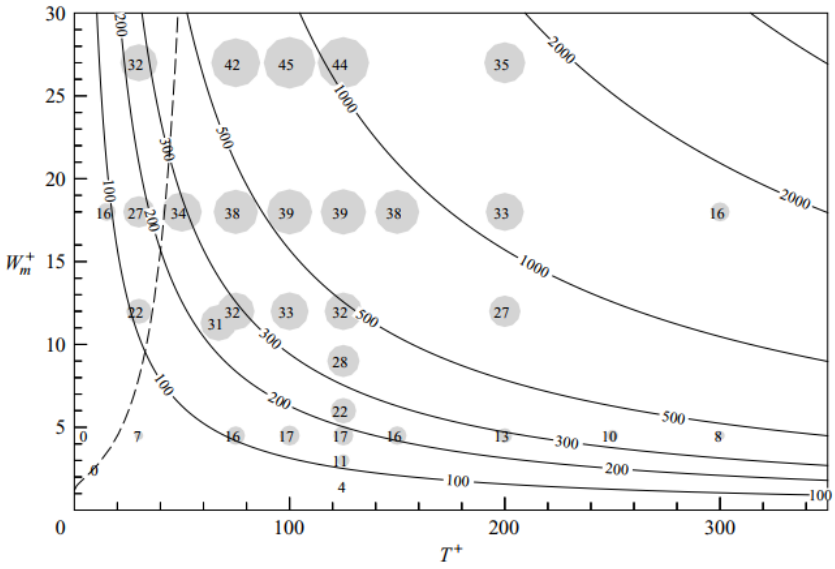

Figure 4.6: Drag reductions(enclosed circles) obtained for varying maximum wall velocity(W_m^+) and time period(T_{osc}^+) (Quadrio and Ricco, 2004)

It is interesting to note that maximum wall velocity is used as the non-dimensional parameter instead of amplitude. A lot of numerical studies on wall oscillations followed from the works of Yudhistira and Skote (2011) where DNS on turbulent boundary layer was performed and the drag reductions were in accordance to that obtained by Ricco and Wu (2004) in their experimental study. Skote (2012) through the DNS results showed that there is a dependence of drag reduction on the Reynolds number of the flow. A plot of the velocity profiles is shown in figure 4.7 where reductions can be observed for the scaling.

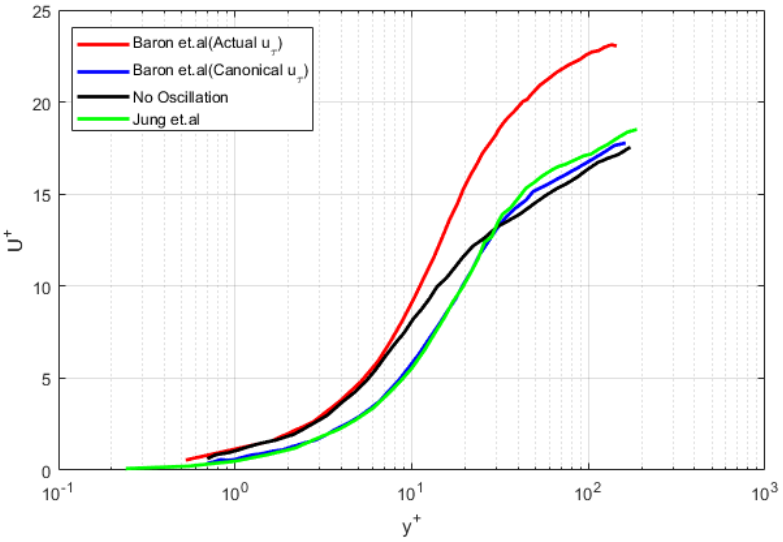

Figure 4.7: Non dimensionalised velocity profiles (U^+ vs y^+) from numerical data

4.2. Observations

The literature explained in the previous sections covers all the specifications and results that were obtained upon analysis. But it is imperative to pick out the main outcomes and explanations of all these texts and summarize them to find points of similarity and departure. This will aid the development of necessary research questions which can be answered through the course of this thesis.

4.2.1. Reynolds number of the studies

Most practical flows fall in the high Reynolds number regimes where the flow is completely turbulent. The shortcoming of these studies is that they are performed at Re which cannot be considered fully turbulent. This is because direct numerical simulations at high Reynolds number is till very computationally intensive (Table-4.1). The experimental studies performed do not provide a good flow visualization of the structures and its response to the wall oscillations. More recent numerical studies by Touber and Leschziner (2012) at higher Reynolds number suggest that the drag reduction is dependent on the Reynolds number of the flow. As the Re increases the peak reductions reduces, this is attributed to the additional effects of the outer scaled structures on the near-wall phenomenon of wall oscillation.

4.2.2. Drag reductions observed

Experimental and numerical studies project different values in terms of maximum drag reduction observed. Numerical studies indicate that maximum drag reductions of 40% can be achieved (Baron and Quadrio, 1995). But experimental studies indicate a lower percentage of drag reductions of 35%. But it is accepted from the data that is available that spanwise oscillations do reduce the skin friction from a turbulent boundary layer when compared to the non-oscillating case.

4.2.3. Scaling of drag reduction

There are three views on the parameters that determine the drag reduction that is observed. They are as follows

1. The amplitude (Z^+_{osc}) and time period of oscillations (T^+_{osc}), these two are the most fundamental parameters which when varied, drag reductions are observed.

2. Trujillo et al. (1997) and others stated that the drag reductions do not depend on Z^+_{osc} and T^+_{osc} independently but on the maximum wall velocity ($W^+_m = \frac{\pi Z^+_{osc}}{T^+_{osc}}$)

3. Jung et al. (1992) and others haven't found the scaling parameter but mention that an optimal time period exists for drag reduction which is around 100-125 viscous scale units (T^+_{osc}). The optimum time period corresponds to the thickness of the stokes layer which maximizes the interaction with the turbulent structures.

4. Choi et al. (2002) explained the drag reduction with the help of two parameters, first one being the wall-normal distance to which the spanwise oscillation diffuses due to viscosity. This length can be obtained from the stokes solution and structures which are within this distance get affected by the spanwise oscillations. The second parameter is the acceleration of the stokes layer.

4.2.4. Mechanism of drag reduction

From chapter 2 it is clear that streaks play a central role in the production of turbulence. The working mechanism of this technique is provided by many authors. Jung et al. (1992) did not explain the mechanism completely but stated that the underlying mechanism is still under study, but a reason for the reduction observed was attributed to the decrease in the number and intensity of turbulent bursts. Laadhari et al. (1994) explained the reduction observed in turbulence statistics to the interaction between longitudinal vortices and the streaks near the wall. Due to the oscillatory motion of the wall, these streamwise vortices are convected in the spanwise direction and break the coherence that is present in the streaks, which reduces the production of turbulence.

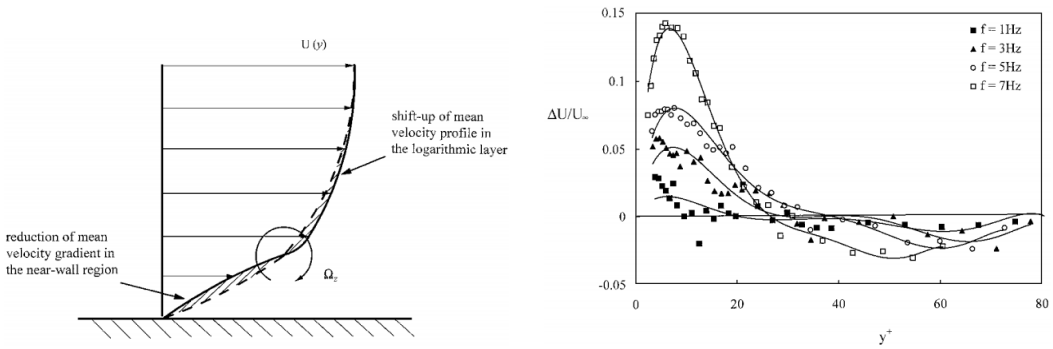

(a) Spanwise vorticity(ω_z)created by the periodic Stokes layer

(b) Velocity reductionsΔu in the boundary-layer

Figure 4.8: Plots from Choi et.al.Choi et al. (1998), velocity reductions were measured from the trailing edge of the oscillating plate for different frequencies of wall oscillation ($\Delta z = 70mm$)

Choi et al. (1998) take a slightly different approach. It is considered that due to the oscillatory motion a periodic stokes layer is created at the wall, which is then convected downstream. From the numerical studies of Baron and Quadrio (1995), at $y^+ = 15$ a maximum in vorticity fluctuation is observed. A consequence of this would be a decrease in the mean velocity gradient in the near-wall region ($y^+ < 15$) and an increase in the mean velocity outside the viscous sublayer ($y^+ > 15$) followed by an upward shift in the logarithmic velocity profile. But from the measured data, the crossover point was found to be $y^+ = 25$.

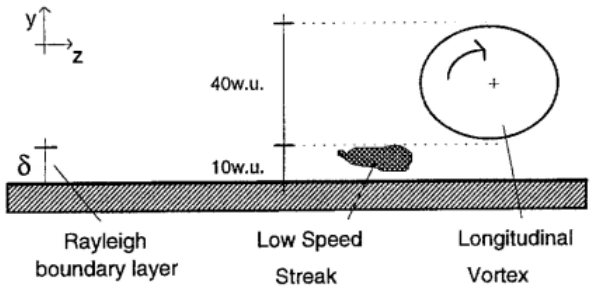

Figure 4.9: Conceptual model of Baron and Quadrio (1995)

Baron and Quadrio (1995) have developed a simplified model, which follows the explanation provided by Laadhari et al. (1994). The oscillations of the plate create a boundary layer which in wall units is equal to $\delta^+ = \sqrt{4\pi T^+_{osc}}$. The effect of wall oscillations is felt up to the edge of this boundary layer. For this to be effective in reducing skin friction drag, the relative displacement of the"*low speed streaks and the above longitudinal vortices, the transverse boundary layer must embed as much of the streaks as possible without influencing the vortices, allowing the maximum relative displacement*" (Baron and Quadrio, 1995). With this, the optimum amplitude of $T^+_{osc} = 100$ was determined.

From these discussions, a common thread is that the reason for the effectiveness of this technique is because the coherence in the streaks is disturbed which has a cascading effect of the whole turbulence production process. Also, all the explanations provided by the authors revolve around the same mechanism but has been explained from different vantage points. One of the goals of this study is to come up with a coherent explanation of the mechanism of the process, with the correct description of the parameters that govern this process along with the correct scaling parameters.

4.3. Aims and objective of current work

In conclusion, it is quite certain that the field of turbulence research is very vast. Through this thesis, the aim will be to start small and focus on creating, understanding, explaining one of the drag reduction technique that is spanwise wall oscillation. With the relevant literature already discussed, it is clear that there are varying explanations, parameters that drive this technique. It is therefore essential to state the main research questions which will be addressed in the thesis.

1. Quantify reductions in skin friction drag through near-wall measurements, Spalding's law of wall and momentum deficit with data from planar particle image velocimetry.

2. Quantify the trends in quantities such as Reynolds stress, turbulent kinetic energy production, quadrant decomposition.

3. Using velocity and vorticity visualizations to infer the large-scale organization of the turbulent structures.

4. Provide a coherent theory to explain the turbulence reduction observed through spanwise oscillations.

5. Provide suggestions about data points and conditions which can be researched in the future.

All these research questions will be tackled by manufacturing the right setup, performing the necessary background study, conducting the experimental campaign and accurate post-processing of the data. Through this study, the aim is to provide experimental data in a regime which can be considered fully turbulent and asses the developed setup for its applicability for future experiments. The final research objective can be stated as

"PIV-based evaluation of turbulent skin-friction drag reduction by spanwise wall oscillation"

5

Experimental setup and procedures

To achieve the aims and objectives described in Chapter-4, an experimental campaign has been performed in the open-return wind tunnel (W-Tunnel) at TU Delft. In this chapter, the specifications of the apparatus used i.e. the wind tunnel, actuating mechanism and flat plate are described. Planar PIV was used to obtain quantitative information, the techniques along with the acquisition procedure and the reduction strategies are discussed in detail, in the following sections.

5.1. Wind tunnel: W-tunnel

To perform the experiments to measure the reduction in skin-friction drag, the setup described in Section-5.2 is placed in the W-tunnel at the High-speed laboratory at TU Delft, shown in Figure-5.1. The wind tunnel is an open-return low-speed with a closed test section. The W-tunnel features a contraction ratio of $9:1$ with exit cross-section of $40 \times 40 cm^2$. The wind tunnel is powered by a centrifugal fan driven by a $16.5 KWh$ motor. Velocities up to 25 m/s can be reached, the current experiments are performed at velocities of 3 and 5 m/s. The velocity is measured and adjusted based on the information of dynamic pressure in the nozzle measured using a pitot tube.

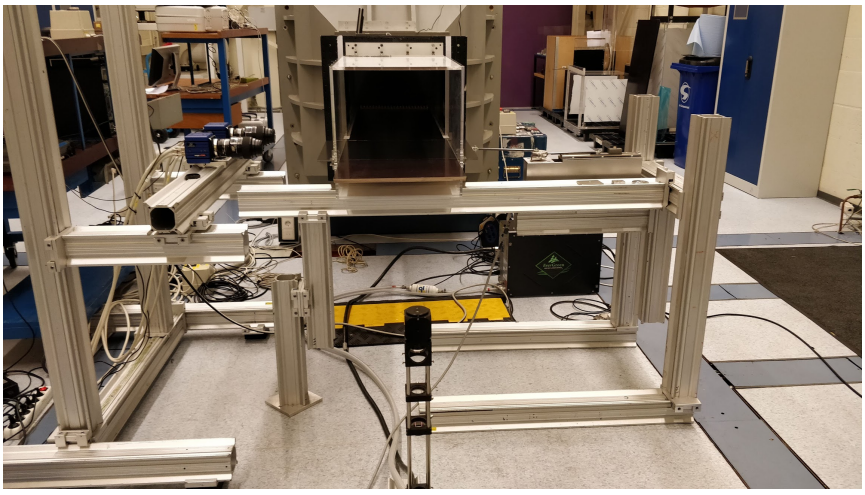

Figure 5.1: Experimental setup in the W-tunnel

The freestream turbulence past the contraction is less than 0.3% for a free stream velocity below 15m/s. Hotwire measurements were performed to obtain the above results. Although the turbulent intensity is not directly relevant for the TBL under investigation, it important to be aware that the flow outside the boundary layer is not turbulent.

5.2. Test section and flat plate

The flow at the exit of the contraction is confined within a rectangular channel 160 cm long. A flat plate is installed 10 cm above the channel floor and the boundary layer is tripped 5 cm after the leading edge of the plate with distributed roughness elements (LEGO strip) of 15 mm height, this is done to obtain a thicker boundary layer to aid better measurements near the wall due to the thickening of the log-layer in the TBL as described in Chapter-2. The schematic layout of the experiment is illustrated in Figure-5.2.

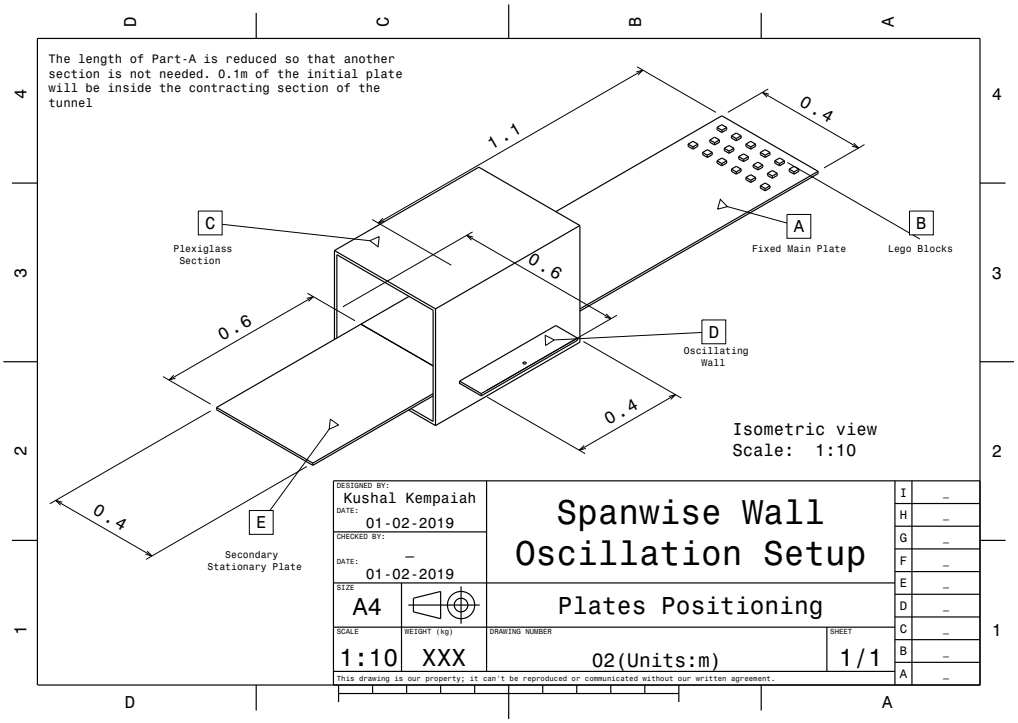

Figure 5.2: Schematic of test section

The fixed and oscillating plate are set flush to the adjacent surface. The inclination of the plate at different points is measured using an inclinometer and is 0.0°±0.2°. The leading and trailing edge were manufactured with an angle of 30°, to avoid large separation and any adverse pressure gradients. The requirement for an elliptical leading edge was not satisfied as the developing boundary layer is forced to transition by the LEGO blocks as detailed. Provisions were also made to place a flat plate underneath the oscillating plate to prevent flow through the gaps of the stationary and oscillating sections. A sketch of the flat plate used for manufacturing is detailed in Figure-5.3.

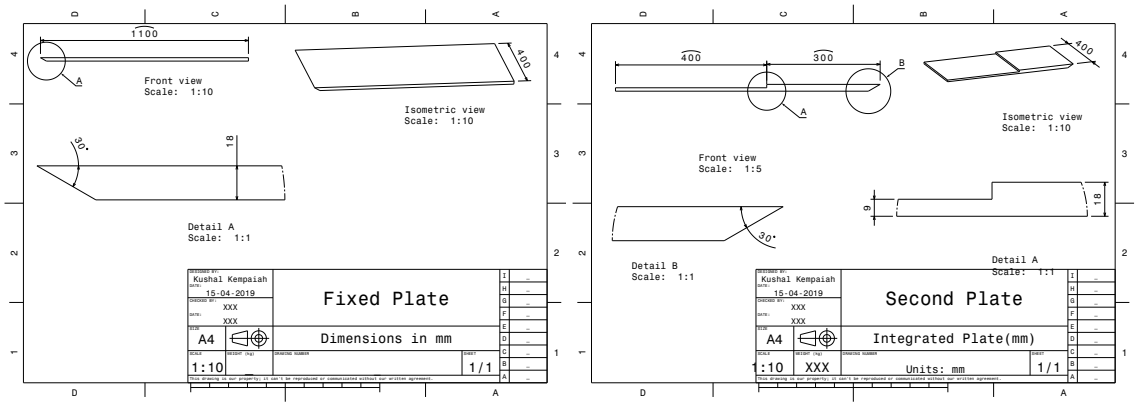

Figure 5.3: Schematic of flat-plates

5.3. Oscillating setup

The oscillations were obtained using a slider-crank mechanism (Figure-5.4) with the system reaching up to 15Hz oscillation frequency and peak-to-peak amplitude of 20 mm. A DC motor manufactured by Maxon (Part number:138690) is used to drive the mechanism. It is designed to operate up to 6000 rpm. A gear of ratio 4.8 : 1 is attached to the motor to produce uniform torque. Frequency of oscillation up to 20 Hz can be achieved, although only 15 Hz is attempted in the current experimental campaign.

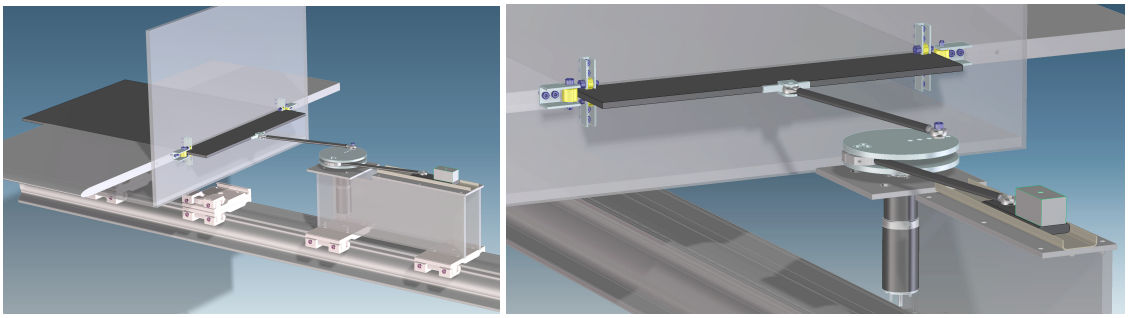

Figure 5.4: Illustration of the oscillating mechanism (not to scale)

It is essential to minimize the unnecessary vibrations arising from the crank mechanism. A counterweight is necessary to stabilize the imbalance, undesired vibrations can hamper the mechanism at play which reduces skin-friction drag. The force experienced by the oscillating mechanism can be approximated as $m\omega^2 r$, where m is the mass of the plate, ω the angular frequency of oscillation and r the eccentricity or the amplitude of oscillations. A preliminary calculation for the force experienced is performed for the optimum oscillating conditions($T^+_{osc} = 100$, Chapter-4) and amplitude of 20 mm is detailed in Table-5.1. As the free stream velocity increases the required frequency for optimum drag reduction increases quadratically and so does the force produced. This means building a mechanical mechanism to handle forces upward of 1400 N and procuring actuators that can reach such frequencies is economically not viable.

u_∞ **[m/s]**	u_τ **[m/s]**	**Frequency** $T^+ = 100$**[Hz]**	y^+**[mm]**	**Force** $m\omega^2 A$ **[N]**
11.2	0.45	135	0.033	1439
9.74	0.4	106.67	0.0375	887
7.3	0.3	60	0.05	284.2
4.87	0.2	26.67	0.075	57.5
2.5	0.1	6.67	0.15	2.84

Table 5.1: Force experienced due to oscillations

5.4. Particle image velocimetry

The instantaneous flow in a zero pressure gradient flat-plate turbulent boundary layer is highly 3-dimensional with vortex structures ranging from all shapes and sizes (Figure-5.5a), more details refer to Chapter-2. But the averaged flow field is 2-dimensional in the streamwise and wall-normal direction, Figure-5.5b shows the instantaneous profiles and the averaged profile. The primary goal (refer to Chapter-4) of the study is to measure the reduction in skin friction drag which can be quantified using high-resolution 2D2C (2-dimension,2-component) planar PIV measurements (double frame, single exposure). The following section discusses, in brief, the fundamentals of PIV and the specifications of the experiment performed.

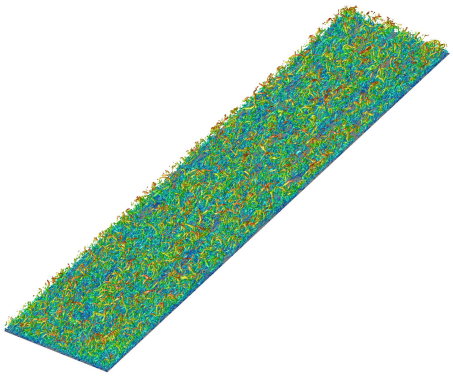

(a) Isocontours of λ_2 (colour proportional to the wall distance) around approximately $Re_\theta = 1400$ (Schlatter et al., 2014)

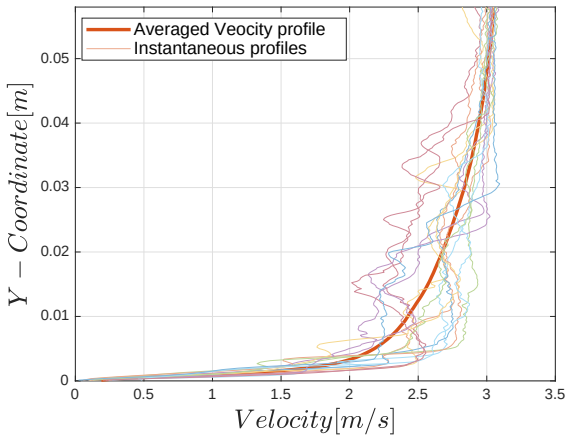

(b) Average and instantaneous streamwise velocity fields in a turbulent boundary layer

Figure 5.5: Structures in TBL and the depiction of velocity profiles

Particle image velocimetry is a non-intrusive optical flow measurement technique based on the evaluation of the displacement of tracer particles between subsequent image frames recorded by an imaging system (Raffel et al., 2018). Figure 5.6 provides a clear schematic of a 2D PIV setup. Particles called as seeders(tracers) are added to the flow which follows the flow faithfully. A thin laser sheet, generated by a pulsed light source, illuminates the seeding particles in two instants with a small gap of Δt. This Δt depends on the flow velocity and the magnification of the image. During the illumination of the domain with laser

light, a camera with either a CCD or CMOS sensor captures the two images in two subsequent frames. The obtained images are then divided into interrogation windows, which are then cross-correlated with the interrogation window of the subsequent frame to obtain the displacement vectors. These displacement vectors are then divided with by the time between the subsequent frames Δt and the magnification of the imaging system to obtain the velocity vectors.

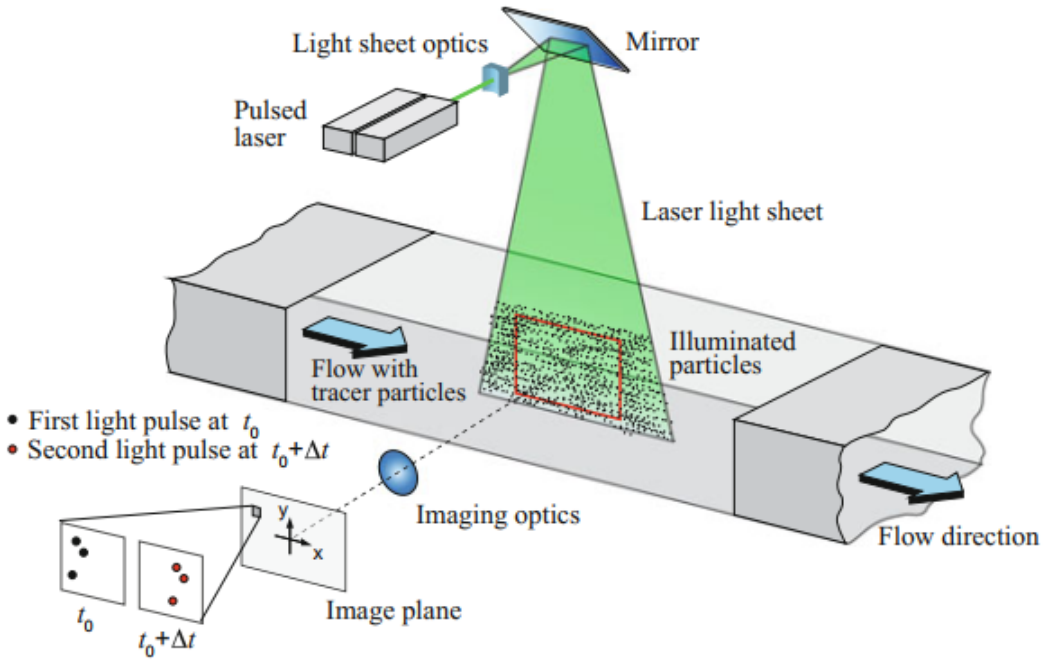

Figure 5.6: 2D PIV setup in a wind tunnel (Raffel et al., 2018)

PIV provides instantaneous data over the whole domain, which enables the use of this technique in many practical applications. The resulting vector field with data at high resolution can be used to compute vorticity and rate of strain. With these resolutions, it is possible to detect coherent structures in the flow field. As a result, PIV provides a powerful approach for turbulence interpretation in terms of structural elements (Adrian, 2007). Table-5.2 provides the technical specifications of the current experimental campaign. A brief description of the components used is provided.

5.4.1. Illumination

The illumination is obtained with a double pulse Nd:YAG Evergreen 200 laser from Quantel (Figure-5.7a). The laser produces light at a wavelength of 532nm, with a maximum pulse energy of 200mJ and repetition rate limited to 15Hz. The laser head is placed under the test section, the laser produces a 6.35mm circular light beam which is then reflected and reshaped into a sheet using mirrors and lenses. The laser sheet expands from the lens and is projected into the wind tunnel and over the plate. The thickness of the laser sheet is approximately equal to 3 mm at the measurement locations (Fig-5.7b).

Flow geometry	Parallel to light sheet
Illumination	Nd:YAG, $2 \times 200mJ$, $540nm$
Seeding material	Fog droplets ($d_p = 1\mu m$)
Recording method	Double frame/single exposure
Ambiguity removal	Frame separation (frame-straddling)
Recording medium	Low speed sCMOS
Pixel size	$6.5\mu m$
Recording lens	$105mm/f_\# = 8.0$
Magnification	0.22
Observation distance	$0.4m$
Maximum in-plane velocity	$U_\infty = 3.0$ m/s, 5m/s
Field of view	$7.4 \times 6.2cm^2$
Interrogation area	16×4, 6×1.5
Acquisition rate	$f_{acq} = 15Hz$
Number of Samples	2000
Dynamic spatial range	135 (Wall normal direction)
Dynamic velocity range	100 : 1 (Streamwise direction)
Pulse delay	$200\mu s$, $150\mu s$

Table 5.2: Specifications of PIV setup

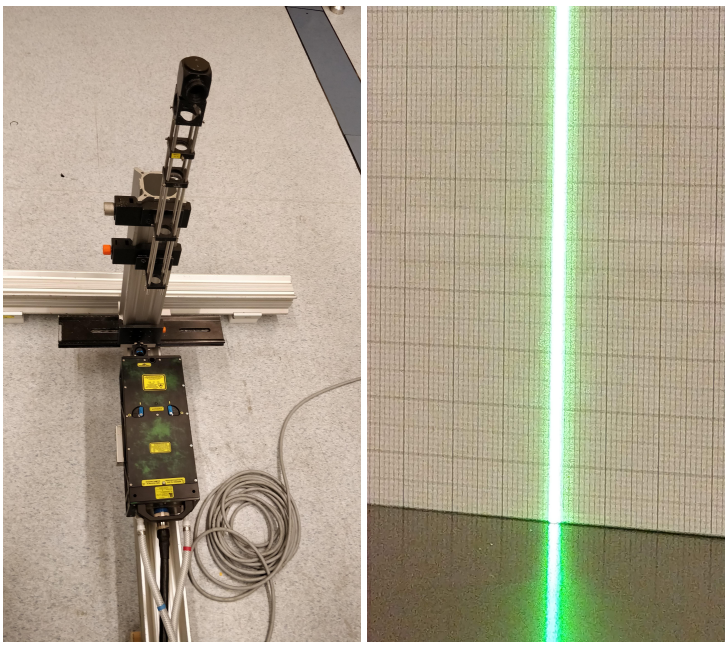

(a) Quantel evergreen laser head **(b)** Thickness of the laser sheet

Figure 5.7: Illumination used

5.4.2. Seeding

Seeding particles in the form of fog are employed as tracers, which scatter the laser light and consequently captured by the imaging system employed. The fog particles are spherical

with a diameter of 1µm. The particles used are known to not affect the flow and are also expected to follow the flow faithfully. The *SAFEXs* fog generator is placed upstream of the fan which drives the flow.

5.4.3. Imaging system

The acquisition is performed using two scientific CMOS cameras. The camera is capable of recording at 50 Hz at a full resolution of $2560px \times 2160px$. Each pixel can store 16-bit information, which means 65536 intensity levels can be distinguished. The size of the pixel i.e. pixel pitch is 6.5μm and the size of the sensor is 16.6 mm ×14.0 mm.The cameras are equipped with a Nikon objective of 105mm focal length and an F-stop ($F_\# = 8.0$).

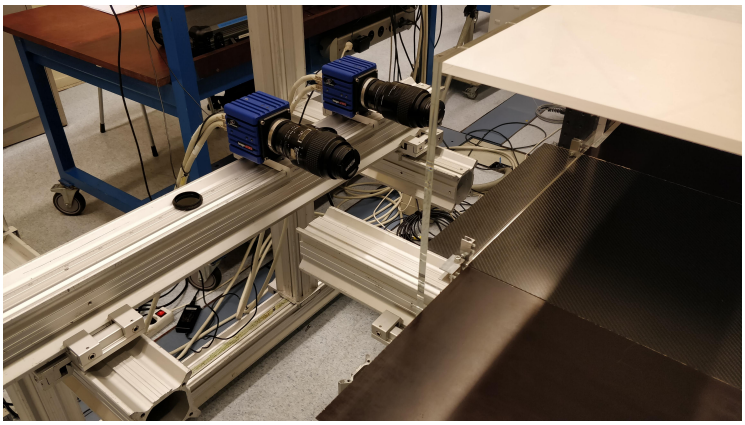

Figure 5.8: Imaging system with the described lens

5.5. Data acquisition procedure

As detained in Chapter-4, the thesis aims to measure the reduction in skin-friction due to spanwise wall oscillation. The quantification is performed using three techniques.

1. Direct wall measurements where the slope $\left(\frac{\partial u}{\partial y}\right)_{y=0}$ is measured, gradient of the mean streamwise velocity at the wall provides a quantitative description of the shear stress (τ_w).
2. Spalding's law of wall relation is used to determine the wall friction velocity.
3. Control volume analysis, where the momentum deficit across the control volume encompassing the boundary layer thickness is adopted. First, mass conservation is confirmed following which the momentum lost between the inlet and the outlet of the CV was measured and an estimate of C_f is obtained.

To achieve this, experiments are performed at free stream velocities of 3m/s and 5m/s. Data acquisition is performed keeping the three techniques in mind, to obtain the required information.

5.5.1. Position of measurements

The position over the flat plate where data is obtained should satisfy the techniques that will be adopted (Sec-5.5) For the control volume approach two locations one upstream

(Inlet) and the other downstream (Outlet) of the oscillating plate are chosen. Also, data acquisition is performed at a third location (Over plate) which is used to infer wall shear measurements. Figure-5.9 provides a schematic of the acquisition location to the complete flat plate configuration.

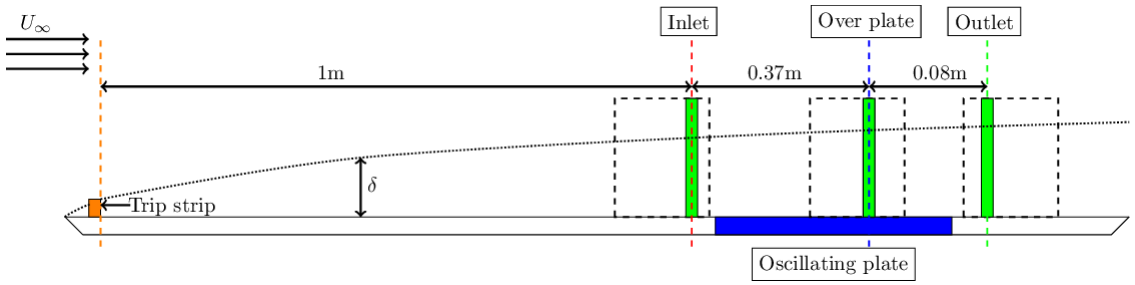

Figure 5.9: Schematic drawing of the flow facility with oscillating section and regions of interest aimed at in the PIV experiments (not to scale)

5.5.2. Selection of sampling strategy

Low-speed PIV is performed in the current experiment, the acquisition frequency is limited to that of the Evergreen laser which operates up to a frequency of 15 Hz. The field of view (FOV) in the wall-normal direction is desired to be about 6 cm to capture the entire boundary layer, this is obtained by using a lens of focal length 105 mm and placing it at a distance of 0.4m from the laser sheet which is present over the mid-plane of the flat plate. Base on the above specifications, FOV obtained for the full sensor is 7.4 cm × 6.0 cm which translates to a magnification of 0.22 based on equation-5.1.

$$M = \frac{pixel\ size \times number\ of\ pixels}{FOV} = \frac{6.5 \times 10^{-6} \times 2560}{7.4 \times 10^{-2}} = 0.225 \tag{5.1}$$

While performing planar PIV two important aspects to be implemented for the acquisition are

- Obtaining the particle image diameter of at least two pixels, this is essential to prevent pixel locking which introduces errors in the cross-correlation algorithm.
- Pulse separation time should be chosen such that the maximum in-plane displacement of the particle should be $1/4^{th}$ the interrogation window size. This should be calculated at the free stream velocity. Also, a rule of thumb would be to choose a displacement distance of 10-15 pixels.

Based on the magnification obtained, the geometric particle image diameter ($d_{geom} = Md_p = 0.225 \times 1\mu m$) is $0.225\mu m$. The geometric effect is not the only influence on the diameter, rather diffraction limits the diameter of the particle and is given by equation-5.2.

$$d_{diff} = 2.44\lambda(1+M)f_\# \tag{5.2}$$

where λ is the wavelength of the illumination source i.e $532nm$ and $f_\#$ is the f-stop which is a property of the imaging system defined as ratio of focal length(f) to the aperture diameter(D). The effective particle image diameter (d_τ) is given by $d_\tau = \sqrt{(Md_p)^2 + d_{diff}^2}$.

For the requirement stated above the $f_{\#}$ is set to 8. The pulse separation chosen for free stream velocities of 3 and $5m/s$ are $200\mu s$ and $150\mu s$. Additional details are provided in Table-5.2.

Full sensor images are not required for computing statistics and the average velocity field. The time required for acquisition and post-processing of the full sensor images is high. Therefore, the sensor is cropped to a size of 300 pixels ×2160pixels. This enables quicker acquisition and data reduction. Full images are also obtained for qualitative studies of hairpin packets. The number of images for the statistical convergence is chosen to be 2000. 200 full sensor images are also obtained.

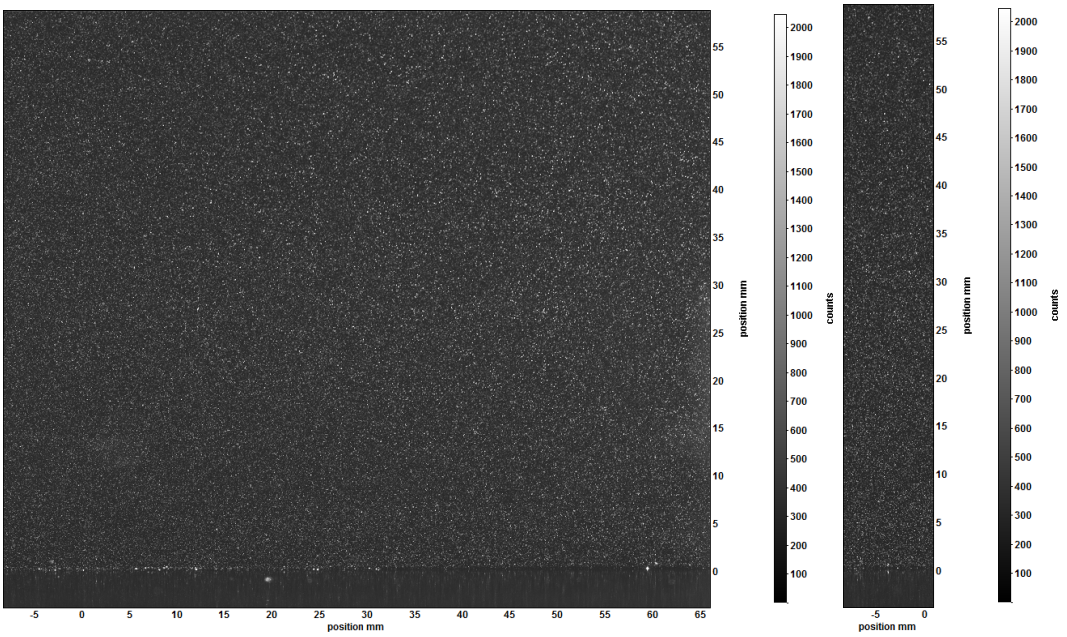

Figure 5.10: Image comparison between the full sensor and a cropped one

5.6. Data reduction technique

The images (Raw data) acquired during the experiment need to be processed to obtain the velocity data and its derivatives like vorticity, Reynolds stresses, turbulence production. The path undertaken to extract the velocity fields is detailed in the following section.

5.6.1. Velocity field reduction

The following steps are employed to obtain the velocity fields.

1. Reorganize frames: since the acquisition is performed by two cameras are simultaneous, to process the images the image pairs need to be separated. This is accomplished using the reorganize frames.

2. Extract Volume: for near-wall measurements, it is not feasible to perform cross-correlation of small windows throughout the whole FOV, therefore regions of interest near the walls are extracted.

3. Subtracting time filter: time filters are primarily used to remove the background noise that is present in the raw images. For the current experiment as the plate is oscillating the oscillations are unsteady. Therefore, the butter-worth filter is used to remove the unsteady reflections. Butterworth filter works by applying a high pass filter through the images. As the reflections occur at frequencies lower than that of the particles which are moving in the flow they are attenuated. The necessary condition that the particle has to move 3 to 4 times faster than the reflections is also satisfied.

4. PIV Cross-correlation: using this technique a vector field of two single exposed images is obtained. Two different widow sizes are used for the complete boundary layer profile and near-wall measurements (Details in Section-5.7). For the full boundary layer, a multipass iteration method with a decreasing size is adopted. 64×64 window with weights of 1:1 and overlap of 75% for the first two passes, followed by 32×32 widows with the weights of 4:1 in the streamwise direction and overlap of 75%. The final vector resolution of the near-wall measurements is 0.2325 mm/vector

5. Vector statistics: quantities such as mean velocity, standard deviation, Reynolds stress, uncertainty and turbulent shear stress can be obtained form this option.

6. x-y plot: line plots of the properties under study are produced using this option and are then used for further studies.

5.7. Wall shear measurements

To extract higher resolution for the velocity fields near the wall, a smaller volume is extracted (Fig-5.11a). The PIV cross-correlation is applied over this volume, a multipass iteration method with the decreasing size is adopted. 64×64 window with weights of 4:1 in the streamwise direction and overlap of 75% for the first two passes, followed by 24×24 widows with the same weights but with an overlap of 87%. The final vector resolution of the near-wall measurements is 0.0872 mm/vector. With this resolution, the viscous sublayer where a linear relationship exists is easily quantified. It is also important to note that determining the location of the wall is important to obtain a perfect match in the inner scaled profiles.

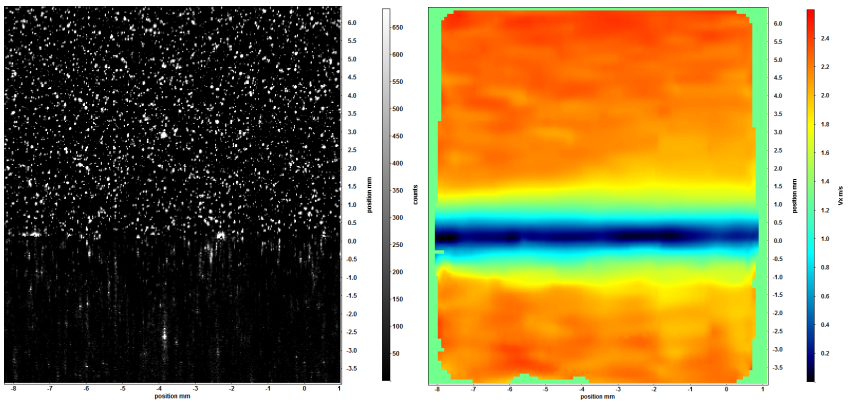

(a) Extracted volume **(b)** Instantaneous velcioty field

Figure 5.11: Extracted volume for near wall measurements

For the near-wall measurements as can be seen from Figure-5.12a, the reflections of the fog particles on the flat plate produces a symmetric velocity profile, and the point of inflection is above the zero set through calibration. Therefore a systematic error exists concerning the wall location. The slope of the velocity profile is used to determine the cutoff location. Close to the wall, the slope is constant and then tends to change upon reflection. In Figure-5.12b, the slope increases and then becomes constant at a y-coordinate of $2.8 \times 10^{-3} m$ and then a sharp drop is observed, the lowest value of y for which the slope is constant is chosen as the cutoff. Therefore the points up to which this trend is satisfied are considered as suitable data and the rest are removed (Figure-5.12c). After which a linear interpolation is performed on the points which satisfy this relationship and the line is extrapolated to determine the y-coordinate when the free stream velocity goes to zero. This length is chosen as the offset and all the data points (y-coordinates) are reduced by the offset to have the right velocity profile (Fig-5.12d). Figure-5.12d shows the linear fit curve for the points in the viscous sublayer, whose slope is used as $\left(\frac{\partial u}{\partial y}\right)_{y=0}$ for the drag reduction calculations. The same technique is also adopted for all the complete velocity profiles. The systematic error in determining wall position is about $100 - 250 \mu m$.

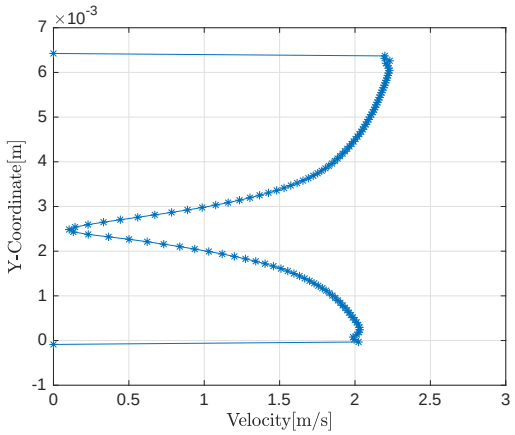

(a) BL profile with reflections from the wall

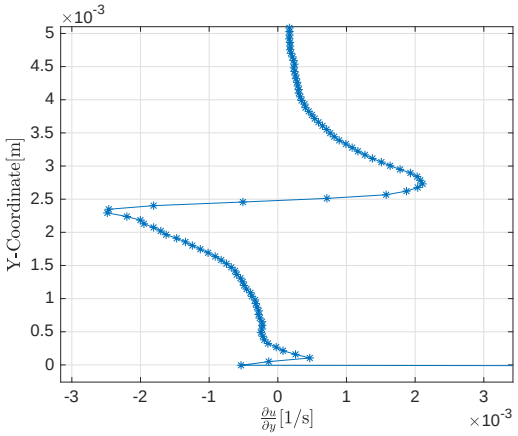

(b) Slope $\left(\frac{\partial u}{\partial y}\right)$ of the velocity profile

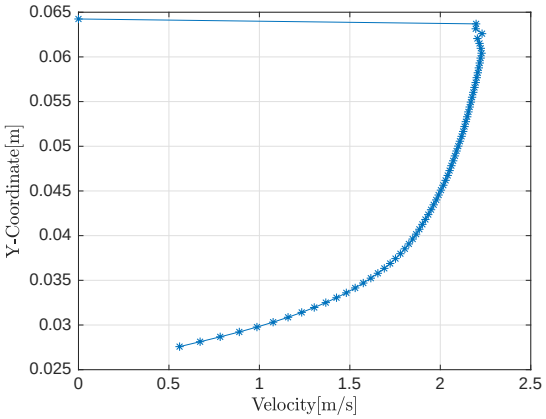

(c) Offset corrected BL profile

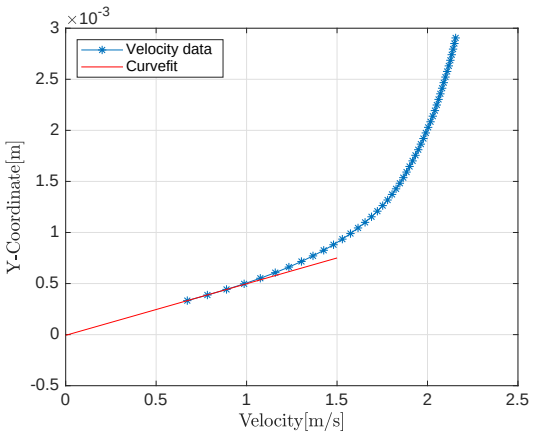

(d) Linear curve fit for slope determination

Figure 5.12: Correcting the near-wall boundary layer profile

A similar approach is adopted when correcting for the complete boundary layer pro-

files, but instead of adopting the slope to determine the cutoff, the cutoff is obtained based on the inflection of the velocity profile. Close to the wall, the slope is constant and then tends to change upon reflection. A liner fit is obtained to determine the required offset. This technique is found to be consistent for all the boundary layer profiles (Figure-5.13).

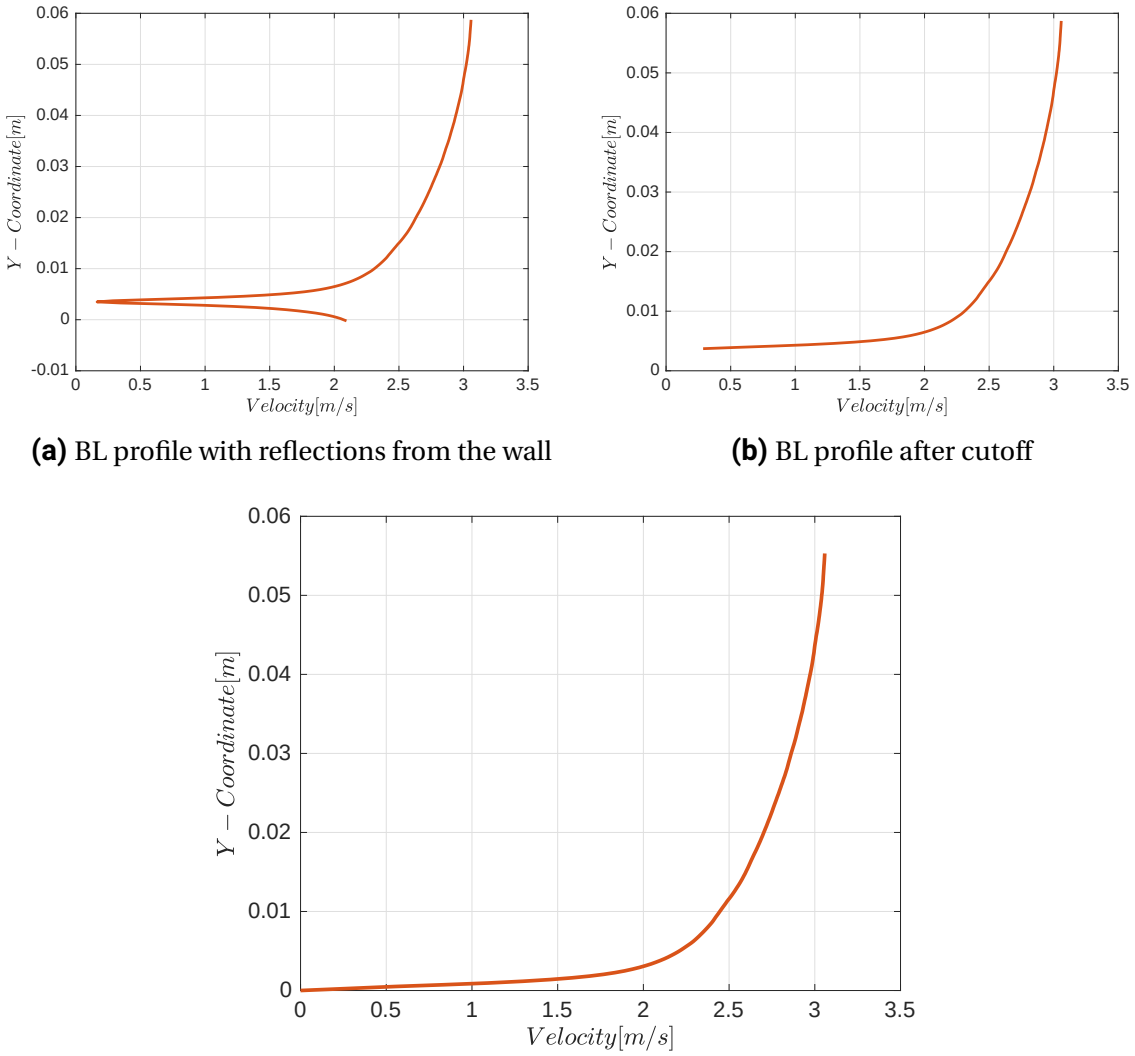

(a) BL profile with reflections from the wall

(b) BL profile after cutoff

(c) Offset corrected BL profile

Figure 5.13: Correcting the full boundary layer profile

5.8. Control volume approach

Another technique that is used to measure the reduction of drag is by adopting a control volume approach. For the current case of a planar turbulent boundary layer measurement, a control volume encompassing the boundary layer from the inlet section to the outlet is considered (Fig-5.14). The lower boundary corresponds to the wall of the flat plate, the upper surface is at δ_{99}, the inlet and outlet planes are the regions through which the mass enters and exists the control volume.

The upper surface of the control volume is selected as the edge of the boundary layer as the shear stress at δ_{99} is zero simplifying the relation. Therefore, the momentum lost by the

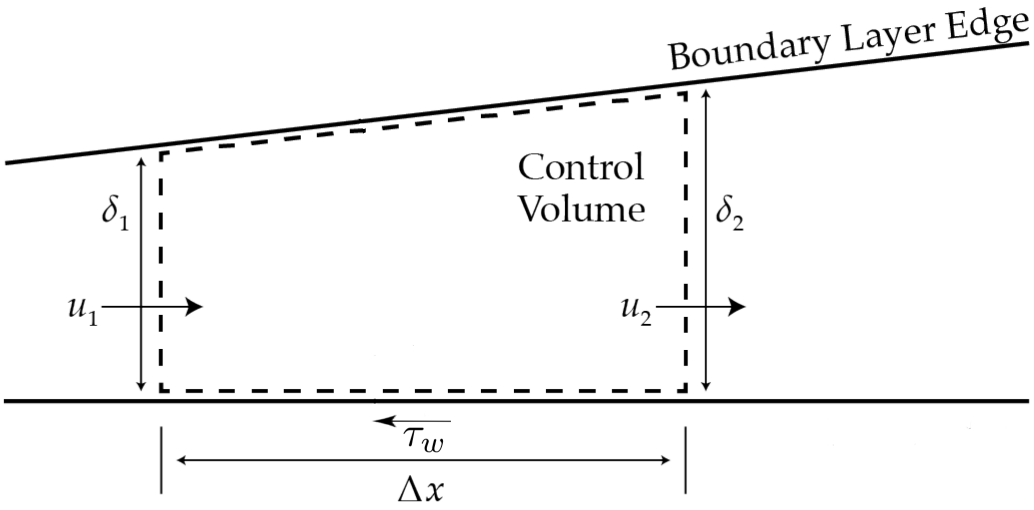

Figure 5.14: Control volume adopted

fluid from inlet(δ_1) to outlet(δ_2) is a consequence of the shear stress at the wall. The mass (Eq-5.3) and momentum (Eq-5.4) conservation for the current boundary layer analysis are as follows.

$$\int_0^{\delta_1} \rho u_1(y)dy = \int_0^{\delta_2} \rho u_2(y)dy \tag{5.3}$$

$$\int_x^{x+\Delta x} \tau_w(x)dx = \rho\left(\int_0^{\delta_1} u_1^2(y)dy - \int_0^{\delta_2} u_2^2(y)dy\right) \tag{5.4}$$

For the data of the current experimental campaign, the free stream is not captured in the FOV. Therefore when applying the above technique of momentum deficit the results are very sensitive to the height of the control volume adopted. Large variations in the drag reductions are obtained. The results corresponding to this technique are discussed in Appendix-A.

5.9. Uncertainty quantification and convergence

To provide the reader information on the uncertainty associated with the processed data, the relative uncertainty is measured using 95% confidence interval and is scaled with the mean velocity ($\bar{U}$) and is in the limits. Equations 5.5 and 5.6 are used to determine the uncertainty over the mean and variance of the velocity data. The corresponding data is reported in Table-5.3.

$$\epsilon_{\bar{u}} = 1.96\frac{\sigma_{\bar{u}}}{\sqrt{N-1}} \tag{5.5}$$

$$\epsilon_{\sigma_{u^2}} = \frac{1.96}{\sqrt{N-1}} \tag{5.6}$$

Re_θ	Number of Samples	Uncertainty Mean $\epsilon_{\bar{u}}(\%)$	Uncertainty Variance $\epsilon_{u^2}(\%)$
1000	2000	0.78	1.46
1787	2000	0.59	0.87

Table 5.3: Uncertainty of mean and variance

Statistical convergence of the mean velocity data is essential to know that the number of samples is sufficient for statistical convergence. Therefore statistical convergence of the mean velocity is analysed for N-number of samples, with the reference velocity for scaling being the mean of the 2000 samples. The location for analysis is $y^+ = 50$. Convergence is obtained with 2000 independent samples (See Figure-5.15).

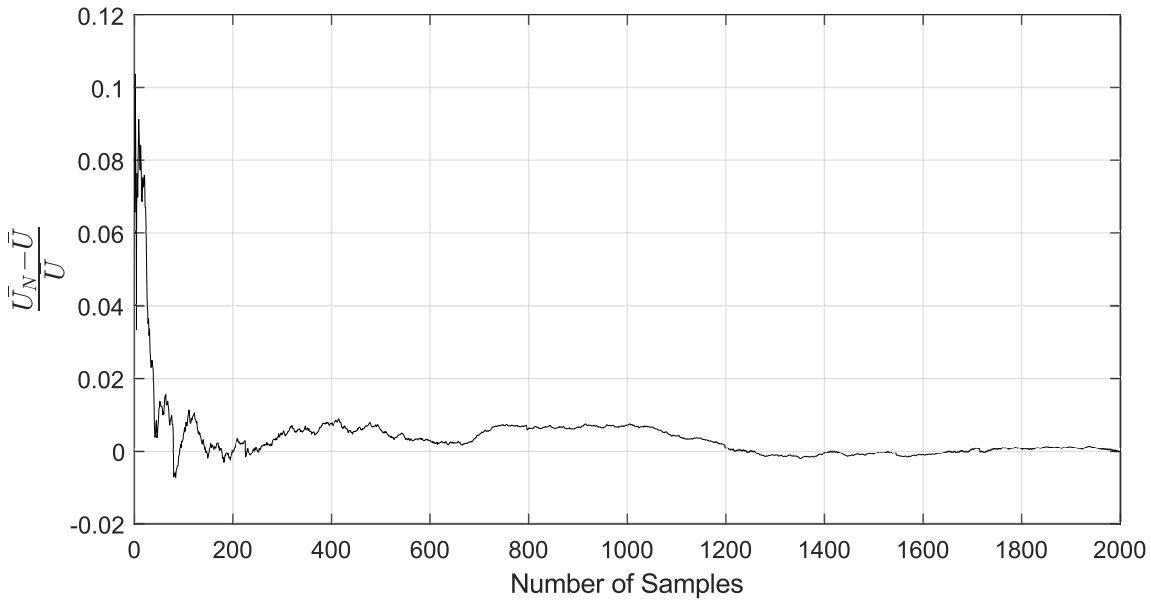

Figure 5.15: Statistical convergence of $\overline{U}$ with number of samples N at $y^+ = 50$

6

Results and discussions

The results obtained after employing the data reduction techniques (section-5.6) are discussed in detail. Starting from the presentation of turbulence statistics of the canonical zero pressure gradient turbulent boundary layer, the scaled velocity profile of the oscillated conditions, followed by an analysis of the drag reduction obtained by the different methods discussed in Section-II d. The spanwise oscillations affect vorticity near the wall (viscous sublayer thickened), the unsteady events near the wall (ejections and sweeps) are also affected. The changes quantified in vorticity, Reynolds stress and turbulence production, quadrant decomposition are also reported.

6.1. Turbulent boundary layer characteristics

The boundary layer obtained during the experiments first needs to be verified, this is done by comparing the non-dimensionalised mean streamwise velocity profiles available in theory (Spalding's relation) and DNS simulations at the corresponding Reynolds numbers (Re_θ) (Schlatter and Örlü, 2010). The mean streamwise boundary layer profile and the root mean square (RMS) components of the velocity fluctuations are calculated by averaging the instantaneous PIV fields acquired at the inlet section over the flat plate (See Figure-5.9). As explained both the Spalding curve and the DNS results are used to validate the results obtained.

Re_θ	u_∞ [m/s]	δ_{99} [mm]	δ^* [mm]	θ [mm]	u_τ [m/s]	y^+ [mm]	H
1000	3	59.2	6.68	4.925	0.145	0.10	1.356
1787	5	59.6	6.98	5.380	0.220	0.06	1.296

Table 6.1: Boundary layer properties

For $Re_\theta = 1000$, the non-dimensional velocity profile begins from within the viscous-sublayer ($y^+ = 1.937$) where a linear relationship exists between the scaled velocity and wall-normal distance. There is a good agreement between the PIV data and that of DNS. The data points extend up to the edge of the outer layer ($y^+ = 540$), where a logarithmic relation exists between u^+ and y^+. There is a good distribution of data points throughout the boundary layer. This distribution is also attributed to the low wall friction velocity ($u_\tau =$

$0.145m/s$), due to which $1y^+ = 0.1mm$. Figure-6.1, 6.2 depict the non-dimensionalised velocity profiles for both the Reynolds number under investigation.

For $Re_\theta = 1787$, the velocity profile begins from within the viscous-sublayer ($y^+ = 3.184$) but only one data point is available with the cross-correlation performed. The non-dimensionalised profile matched well with DNS. It can be observed that due to the higher Reynolds number of the flow the extent of the logarithmic region is more, due to a larger scaled separation. Specifications of TBL are provided in Table-6.1.

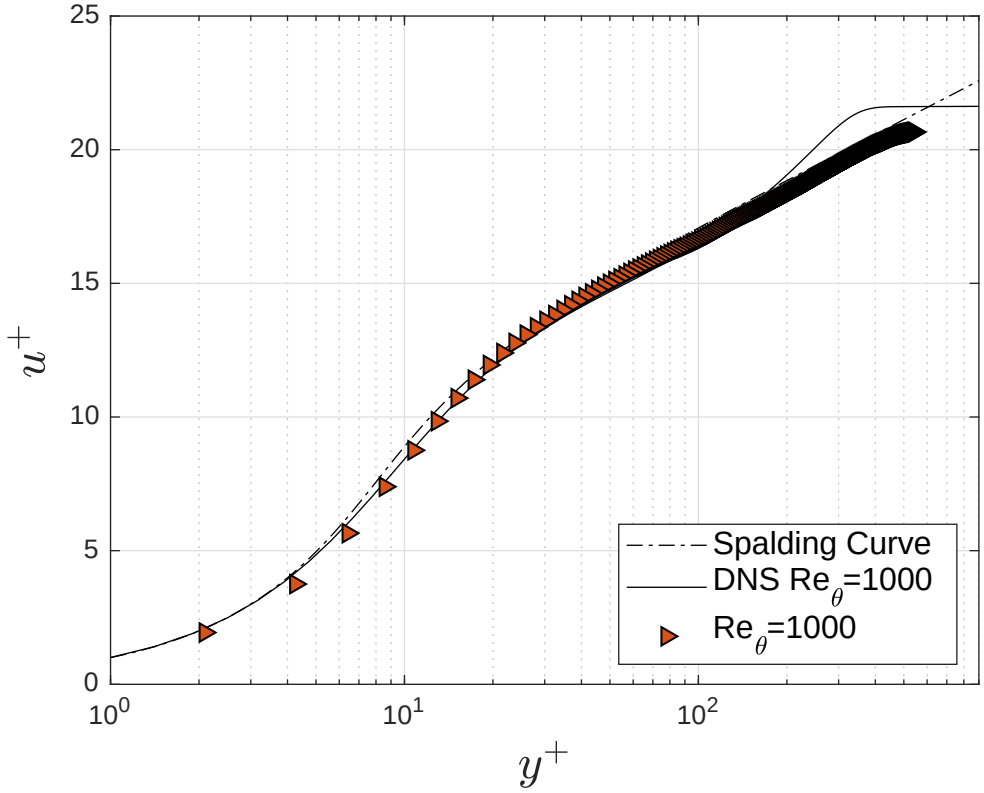

Figure 6.1: Mean stream-wise velocity profile scaled with inner variables (viscous scaling) for a turbulent boundary layer at $Re_\theta = 1000$

The Reynolds stress is also compared to DNS data at similar Reynolds number(Figure-6.3,6.4), the data is non-dimensionalised with near-wall coordinates(ν, u_τ). For $Re_\theta = 1000$, the streamwise Reynolds stress ($\langle u'u' \rangle$) is in good agreement with some deviations in the outer region. The magnitude of the Reynolds stress in the streamwise direction is more due to the gradient of the streamwise velocity profile due to shear. In the event of an ejection or a sweep, the low speed fluid moves away from the wall thus causing a larger fluctuation, whereas the Reynolds stress in the wall-normal direction($\langle v'v' \rangle$) is comparable to lower magnitude as there no variation of the component and the average of wall-normal velocity(V) is zero. $\langle v'v' \rangle$ matches well with the DNS data at the desired corresponding Reynolds number. $\langle u'v' \rangle$ which is the stress developed due to a combination of streamwise and wall-normal fluctuation negative in magnitude, this is because sweep and ejection events are more common in a turbulent boundary layer and the fluctuations have opposite signs.

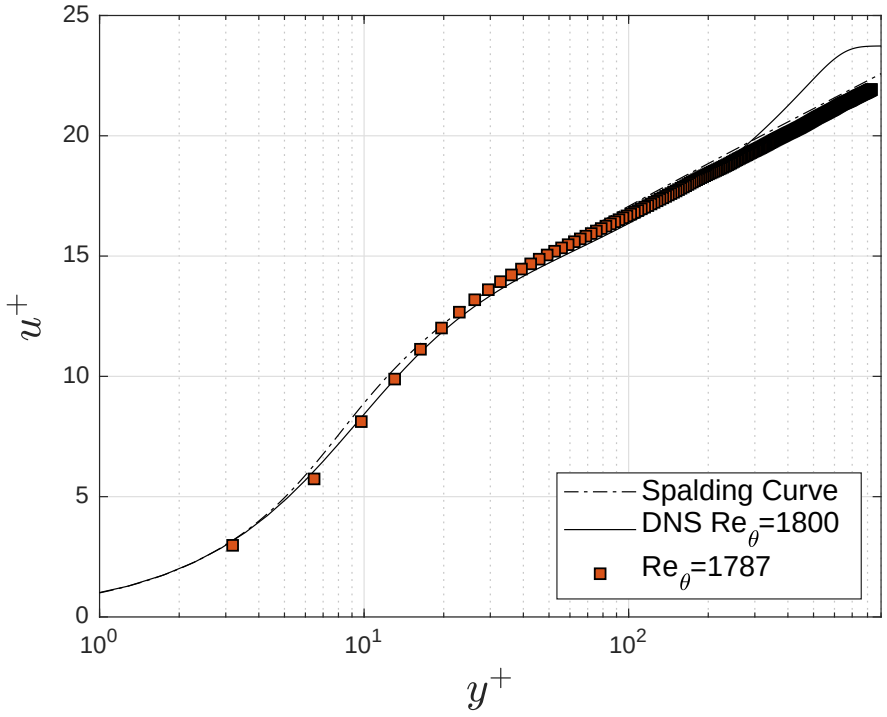

Figure 6.2: Mean stream-wise velocity profile scaled with inner variables (viscous scaling) for a turbulent boundary layer at $Re_\theta = 1787$

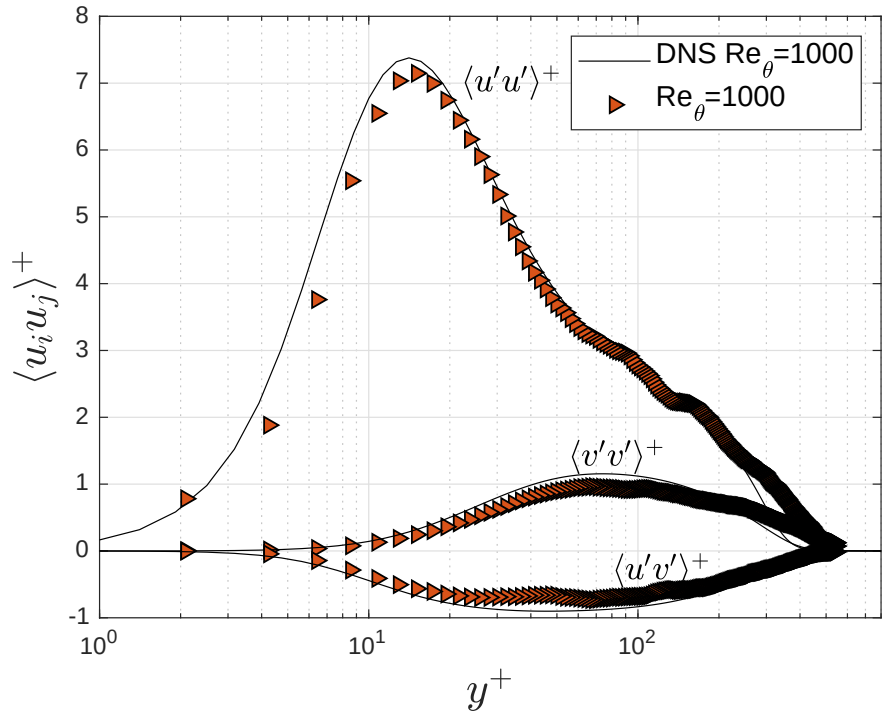

Figure 6.3: Reynolds stress profile scaled with inner variables (viscous scaling) for a turbulent boundary layer at $Re_\theta = 1000$

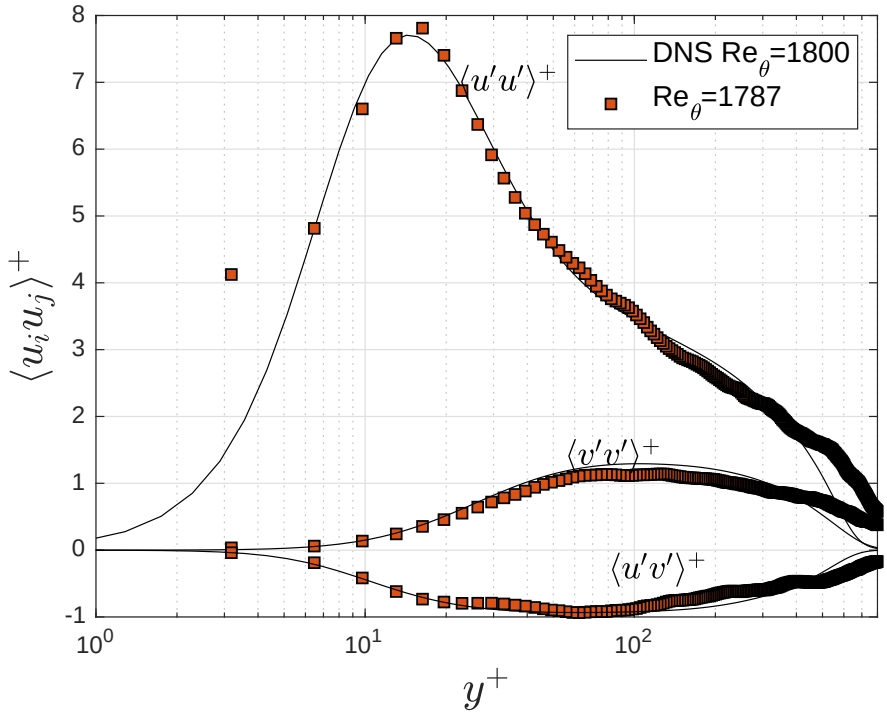

Figure 6.4: Reynolds stress profile scaled with inner variables (viscous scaling) for a turbulent boundary layer at $Re_\theta = 1000$

The current comparison of the TBL data with DNS shows that the boundary layer is indeed canonical with that reported in the literature. Further analysis is performed in the subsequent sections to extract more quantitative information.

6.2. Wall shear measurements

The shear stress at the wall(τ_w), calculated from the slope of the mean streamwise velocity in the the wall-normal direction($\tau_w = \nu \left(\frac{\partial u}{\partial y}\right)_{y=0}$) is quantified for various oscillating frequencies(T^+_{osc}) and amplitudes(Z^+_{osc}). The data reduction technique employed is detailed in Sec-5.7. The oscillations applied for $Re_\theta = 1000$, lie in the optimum range($T^+_{osc} = 100$) discussed in literature due to the low wall friction velocity (Table-6.1), this, also, makes it possible to obtain more data points within the viscous sublayer. Peak reduction of 14.63% is obtained at $T^+_{osc} = 94$ and $A^+_{osc} = 100$ for $Re_\theta = 1000$. The non-dimensional wall velocity (W^+_m) corresponding to the above case is 3.34 and the reported reduction from literature (Quadrio and Ricco, 2004) for a similar condition at $T^+_{osc} = 100$ and $W^+_m = 4.5$ is 17%. For $Re_\theta = 1787$, the lowest non-dimensionalised time period that could be reached was $T^+_{osc} = 215$, the limitation arising due to the mechanical system which actuates the plate could only reach a frequency of 15Hz. At this time period of oscillation and amplitude of $A^+_{osc} = 146$ reduction of 1.97% is obtained. The reductions quantified for the sweep of frequencies and amplitudes for both the Reynolds number of the flows is tabulated in Table-6.2.

Analyzing the trends of the drag reduction for the sweep of frequencies shows that, reductions in skin-friction are obtained for the frequency range of 8 to 15Hz for the boundary

layer at $Re_\theta = 1000$. The corresponding range of T^+_{osc} is $[95-175]$. For the TBL corresponding to $Re_\theta = 1787$ on the other hand, the reduction is quantified only for frequency of 15Hz ($T^+_{osc} = 215$), and an increase is seen for the other frequencies.

The behaviour exhibited can be attributed to the thickness of the stokes layer created due to the oscillations. As explained in section-4.2.4 the stokes layer whose thickness is given by $\delta = \sqrt{\frac{\nu}{\pi f}}$ is transmitted up to the buffer layer for the above frequencies which result in a positive reduction. The range of oscillatory conditions enforced leads to the reduction which is both favourable and unfavourable. Table-6.2 also reports the thickness of the stokes layer along with the non-dimensionalised wall-normal distance. It is clear that for stokes layer thickness (δ^+) less than 10, reductions in skin friction drag is observed. Apart from the case at $Re_\theta = 1787$, $T^+_{osc} = 248$ and $Z^+_{osc} = 146$ where an increase of drag by 7.8% is quantified for a δ^+ of 8.88. This shows that for stokes layer thickness below $y^+ < 10$, leads to favourable changes in the skin-friction drag.

Reynolds number Re	T^+_{osc}	A^+_{osc}	D.R(%)	Stokes layer thickness(δ^+)
1000	95 (15Hz)	100 (10 mm)	+14.63	5.454
	107 (13Hz)		+9.90	5.858
	140 (10Hz)		+8.71	6.679
	175 (8Hz)		+4.60	7.468
	350 (4Hz)		-1.21	10.561
	700 (2Hz)		-4.15	14.935
1787	215 (15Hz)	146 (10 mm)	+1.97	8.274
	248 (13Hz)		-7.80	8.888
	322 (10Hz)		-4.88	10.134
	403 (8Hz)		-7.76	11.330
	806 (4Hz)		-10.20	16.024
	1613 (2Hz)		-7.32	22.661

Table 6.2: Drag reductions obtained from wall shear measurements ('+' indicates reduction)

The trends obtained are depicted in Figure-7, the variations seem to follow a trend. They reduce as the frequency of oscillation is decreased. The velocity profiles corresponding to maximum reductions in skin friction drag at $Re_\theta = 1000, 1787$ are scaled with the outer variables (δ, u_∞) and plotted with linear coordinates in Fig-6.7. The increase of velocity in the wall-normal direction is reduced, for both the cases. These reductions are in agreement to that reported by Choi et al. (1998) and Laadhari et al. (1994).

To provide a more complete understanding of the effect of wall oscillations to the entire boundary layer, the velocity profile with and without oscillations is shown in Fig-6.6a. Due to a decrease in skin-friction, the slope at the wall is reduced (Figure-6.6b) because of which the mass flow rate is also reduced. To compensate for this reduction in mass the profile away from the wall is fuller(higher velocity when compared to no wall oscillation, Fig-6.6c) in comparison to the non-oscillating case. The enlarged views of these regions are shown in Figure-6.6b and 6.6c. A fuller boundary layer profile implies that more momentum is present in the fluid, meaning the deficit due to drag is lower.

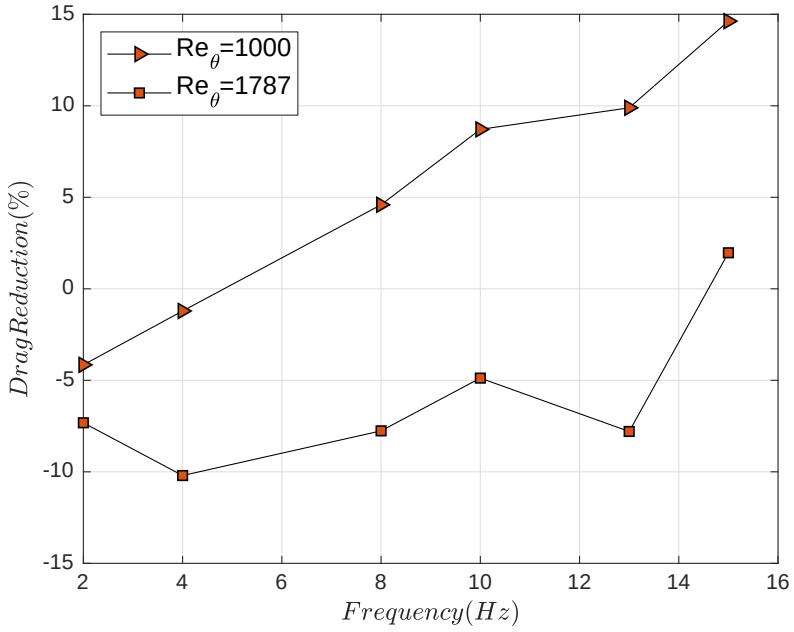

Figure 6.5: Drag reductions from near-wall measurements

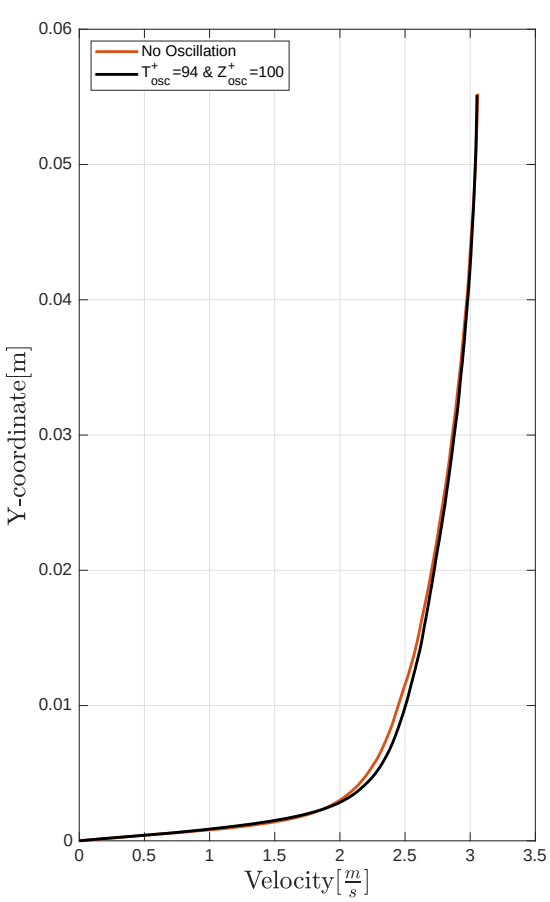

(a) Complete TBL

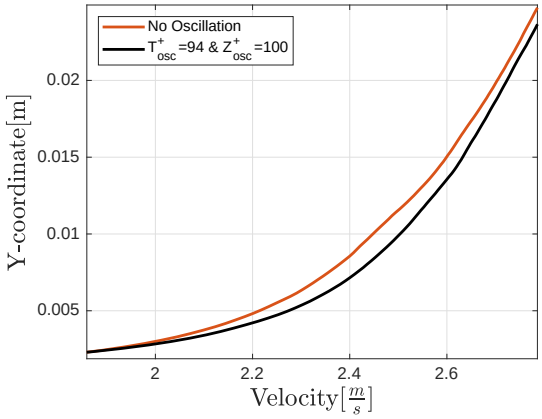

(b) Away from the wall

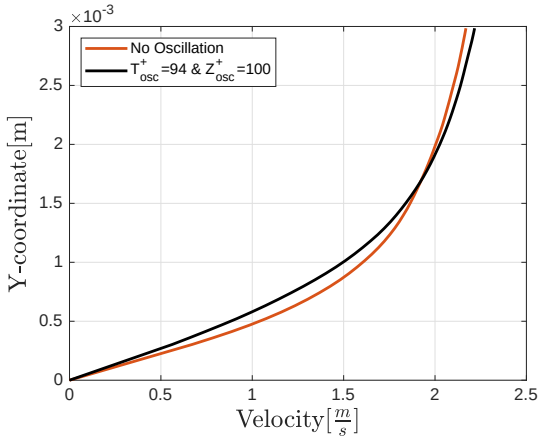

(c) Near Wall

Figure 6.6: Mean streamwise velocity profile comparison for drag reduced oscillations

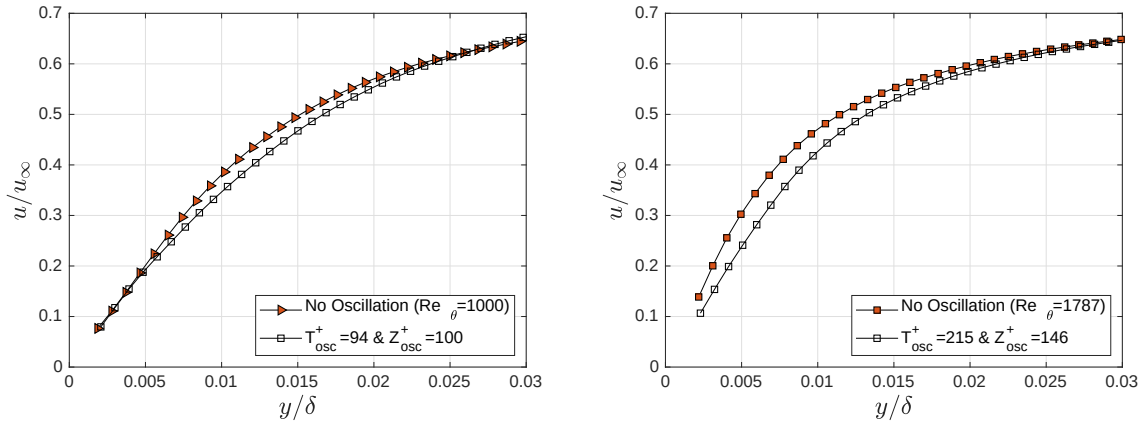

(a) $Re_\theta = 1000$ **(b)** $Re_\theta = 1787$

Figure 6.7: Outer scaled velocity profiles

6.3. Turbulence structure and budget

In addition to mean profile behaviour, it is essential to understand the behaviour of the fluctuations present in the TBL. Fluctuations in the streamwise (u') and wall-normal (v') directions contribute to the Reynolds stress, which is a mathematical construct obtained as a by-product during Reynolds decomposition of the flow variables. These fluctuations are tied with coherent structures (Discussed in Section-2.2). Information related to the dynamic variation in the boundary layer can be derived like the production of turbulence, quantitative information about ejections and sweeps. Ejections and sweeps as discussed in sec-4.6 play a pivotal role in the sustenance of turbulence. A sweep brings high-speed fluid near the wall and ejection lifts low-speed fluid away from the wall, maintaining the energy cascade necessary for turbulence. The Reynolds stresses R_{xx}, R_{xy}, R_{yy} provide quantitative information about the magnitudes of these fluctuations at different wall-normal distances. Through this section, the effect of the wall oscillations individually on each of these properties is looked at in detail.

6.3.1. Reynolds shear stress

The wall oscillations corresponding to the highest reduction in skin friction is analyzed for the variation in Reynolds stress. The stress in the streamwise direction ($\langle u'u' \rangle^+$) is reduced, with a peak to peak reductions of 23%. The reductions of $\langle v'v' \rangle^+$ and $\langle u'v' \rangle^+$ are lower in magnitude. These large reductions in $\langle u'u' \rangle^+$ suggest that wall oscillations dampen these fluctuations, leading to a reduction in movement of high and low-speed fluid (Figure-6.8). Close inspection of figure-6.8 shows that the peak of the streamwise Reynolds stress occurs between y^+ 10 and 20, and thickness of the stokes layer set up by the wall oscillations when lower than 10 lead to reductions. This implies that the lift-up of the streaks or the ejections from the hairpins which occurs near the wall are damped when the effect of the oscillations are confined with this region. Apart from the reduction in the peak of the streamwise stress, the peak is shifted towards the right. Indicating that the thickness of the viscous sublayer is increased., although literature suggests that the shift is expected to be towards the wall due to a reduction in boundary layer thickness (Choi et al., 2002).

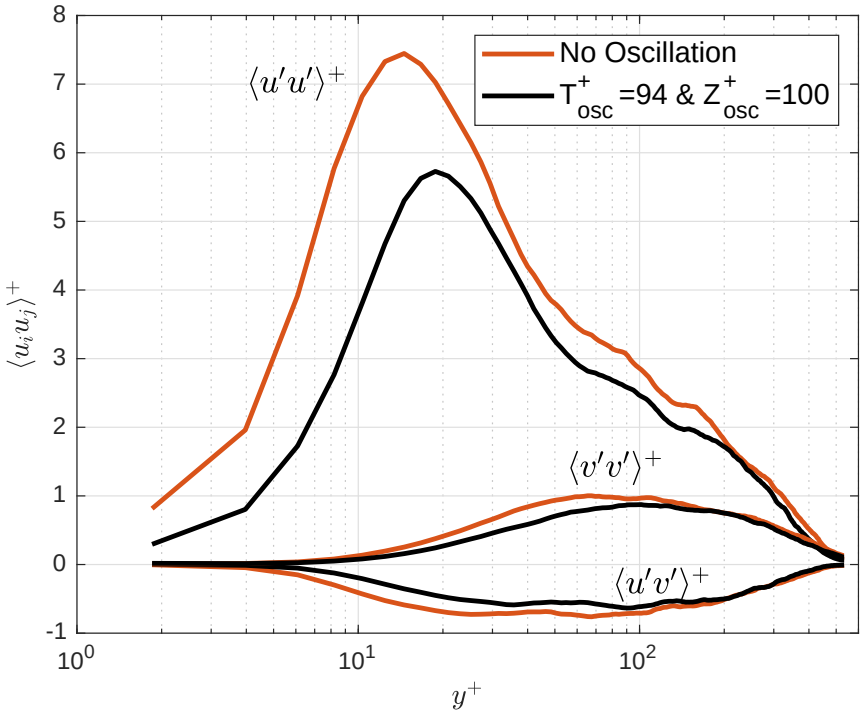

Figure 6.8: Reynolds stress distribution for $Re_\theta = 1000$, drag reduction

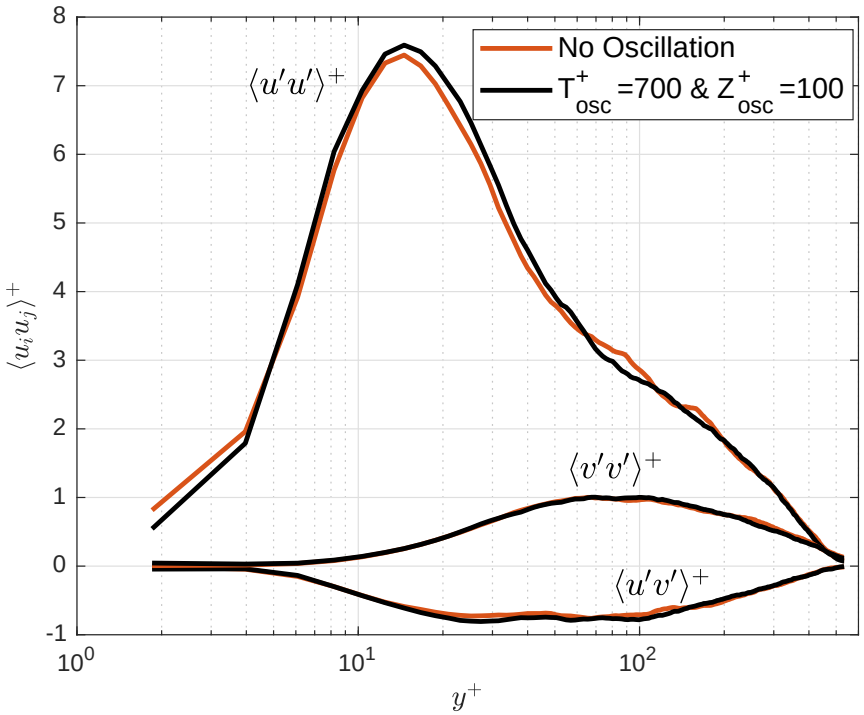

Figure 6.9: Reynolds stress distribution for $Re_\theta = 1000$, drag increase

For cases where an increase in drag is quantified, the peak of all three components of the Reynolds stress is higher. An increase in Reynolds stress in the streamwise direction is observed from y^+ of 7 to 50. This is due to increased disturbances induced by the stokes layer whose depth in wall units is 15. Therefore, the lift up of the streaks are not damped but other disturbances are introduced in the flow. The effect of the favourable oscillation on the Reynolds stress is seen up to a $y^+ = 200$, showing that the region up to the edge of the logarithmic layer is affected by the induced oscillations.

The data presented point in the direction that, the oscillations directly impact the generation/production of turbulence. The magnitudes of these fluctuations are damped with suitable oscillating frequencies. An increase in the amplitude will further increase the vorticity that is produced in the stokes layer due to the higher wall velocity as a consequence of which higher drag reductions will be obtained. Plots corresponding to the other oscillating conditions are present in Appendix-1, and the peak gradually increases from $T^+_{osc} = 94$ to 700, which is consistent with the drag reductions quantified. The following section looks directly at the production of turbulent kinetic energy from the planar data of the current experimental campaign.

6.3.2. Near-wall production

The production of turbulent kinetic energy (TKE) which is calculated by $\frac{\delta}{u_\infty^3}\overline{u'v'\frac{\partial u}{\partial y}}$, is non-dimensionalised by the inner (u_τ, ν) and outer variables (δ_{99}, u_∞). For the plot with inner scaling, it is clear that the observations made in the Reynolds stress plots, where peak reduction was observed between wall distances 10 and 20. The production of turbulent kinetic energy is reduced considerably. The reduction is a consequence of a decrease in the stress $\langle u'v' \rangle^+$ and the slope near the mean streamwise wall velocity. For the unfavourable oscillatory case, the production is increased from y^+ 1 up to 11, which is consistent as the slope near the wall is increased and so is the stresses near the wall. The outer scaled plots for $T^+_{osc} = 94$ and 700 are also compared, for the drag-reducing case($T^+_{osc} = 94$), peak of the production curve is reduced by 35% (Figure-6.10b). In addition to the decrease observed the production becomes zero as the distance from the wall reaches 0.5δ.

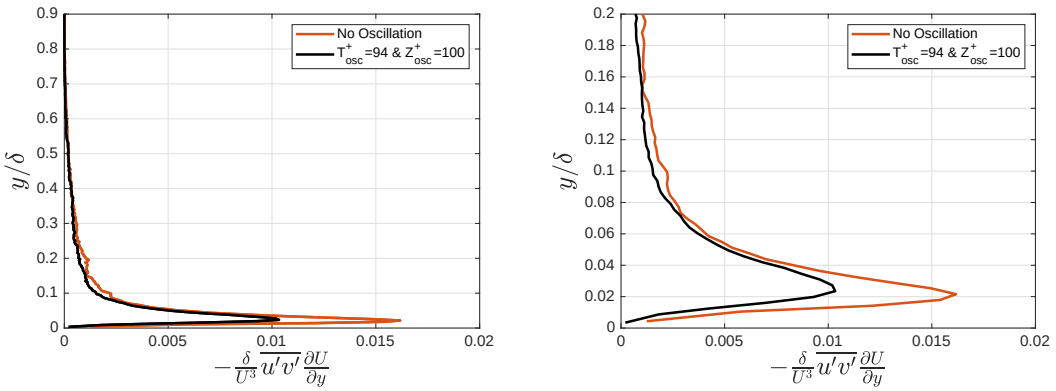

(a) Complete profile at $T^+_{osc} = 94$ **(b)** Enlarged profile at $T^+_{osc} = 94$

Figure 6.10: Outer scaled turbulent kinetic energy production for $Re_\theta = 1000$ (drag reduction)

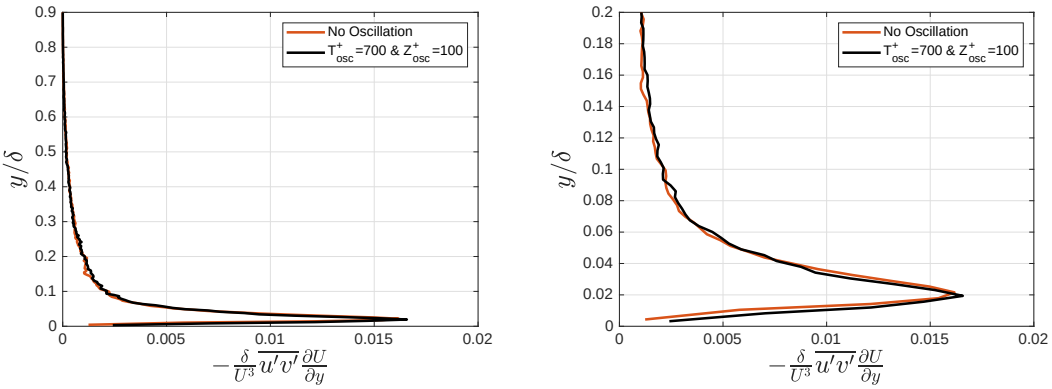

(a) Complete profile at $T^+_{osc} = 700$ **(b)** Enlarged profile at $T^+_{osc} = 700$

Figure 6.11: Outer scaled turbulent kinetic energy production for $Re_\theta = 1000$ (drag increase)

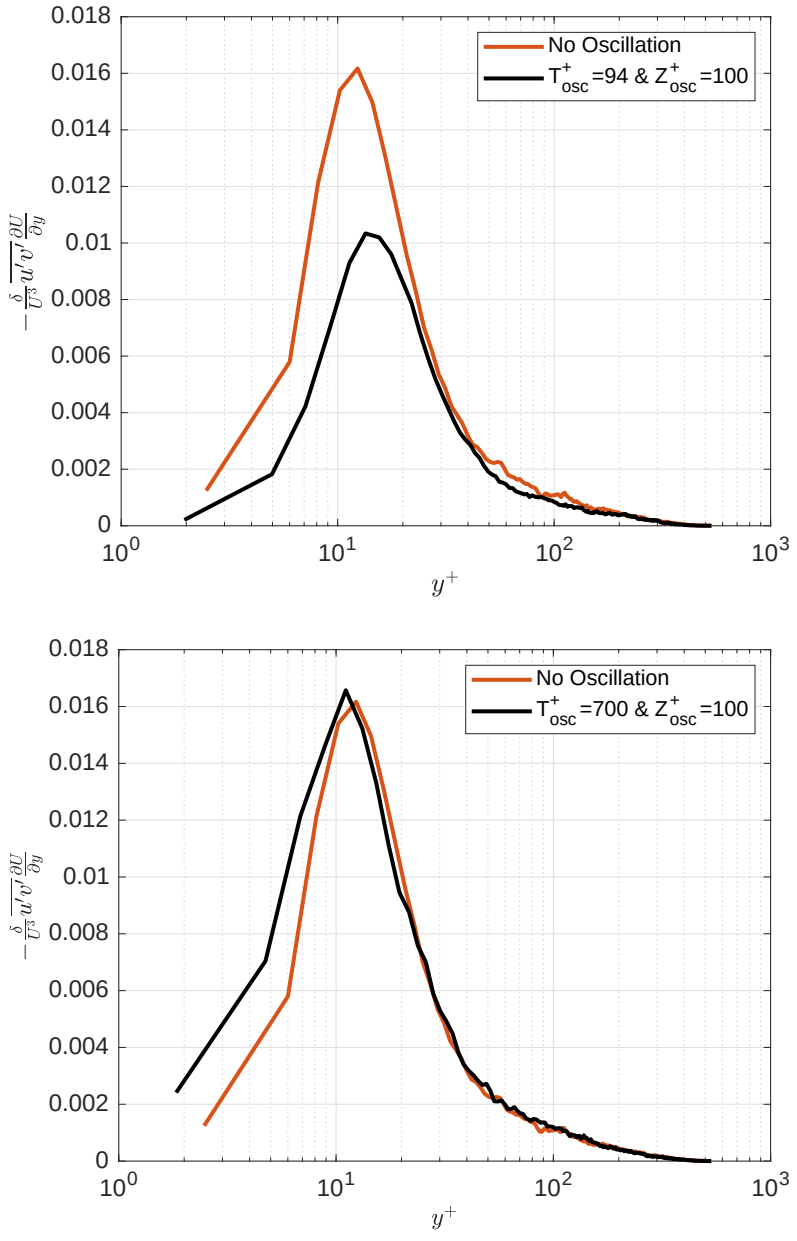

Figure 6.12: Near-wall production wall scaled units

6.3.3. Quadrant decomposition

The damping observed in the Reynolds stresses, turbulent kinetic energy production can be understood by studying the probability density function (PDF) of the streamwise (u') and wall-normal (v') velocity fluctuations at different wall-normal distances. The variation of the PDF along y indicates if the effect of the wall oscillation is confined to regions close to the wall or is seen throughout. It is important to note however that the fluctuations seen in the outer regions of the boundary layer are due to the ejection and sweep events that occurred upstream of the acquisition location. The fluctuations in the outer region are the history of the events that took place earlier. For this reason $y^+ = 10$ and $y^+ = 350$ are chosen for comparison in Figures-6.13a and 6.14a. Close to the wall, the curve is broader due to a larger range of fluctuations between -1.0 to 1.0 m/s in the streamwise velocity, but with the wall oscillations, the peak becomes tighter. Indicating that the wall oscillations cause damping to these larger streamwise variations. For the case with drag increase. the PDF is slightly wider when compared to the non-oscillating case indicating an increase in u' fluctuations.

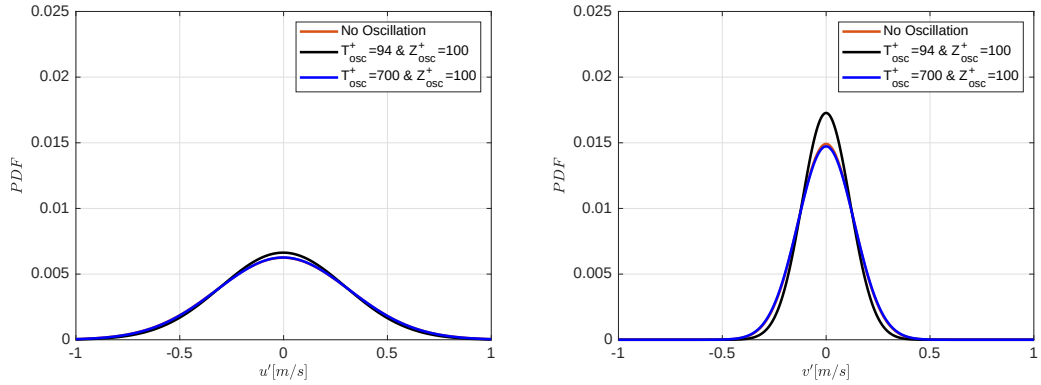

(a) $Re_\theta = 1000$, Streamwise fluctuations(u') **(b)** $Re_\theta = 1000$,Streamwise fluctuations(v')

Figure 6.13: PDF of velocity fluctuations in streamwise and wall-normal direction at $y^+ = 10$

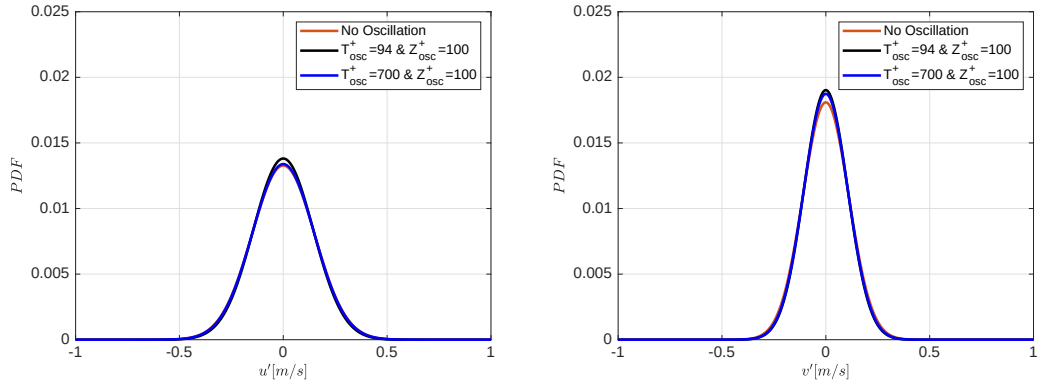

(a) $Re_\theta = 1000$, Streamwise fluctuations(u') **(b)** $Re_\theta = 1000$,Streamwise fluctuations(v')

Figure 6.14: PDF of velocity fluctuations in streamwise and wall-normal direction at $y^+ = 350$

The magnitude of the wall-normal fluctuations, on the other hand, are of lower magnitude between -0.5 to 0.5 m/s but the effect of the damping is more prominent close to the wall. The oscillations tend to dampen the larger positive and negative wall-normal fluctuations. This reduction in the magnitude of the wall-normal fluctuations directly leads to a reduction in large streamwise fluctuation ultimately causing a reduction in the Reynolds stresses observed as lower and high-speed fluid in the shear layer are not displaced by a large distance. Away from the wall however, the peaks are curves are very similar but the peaks of the oscillated case are slightly higher.

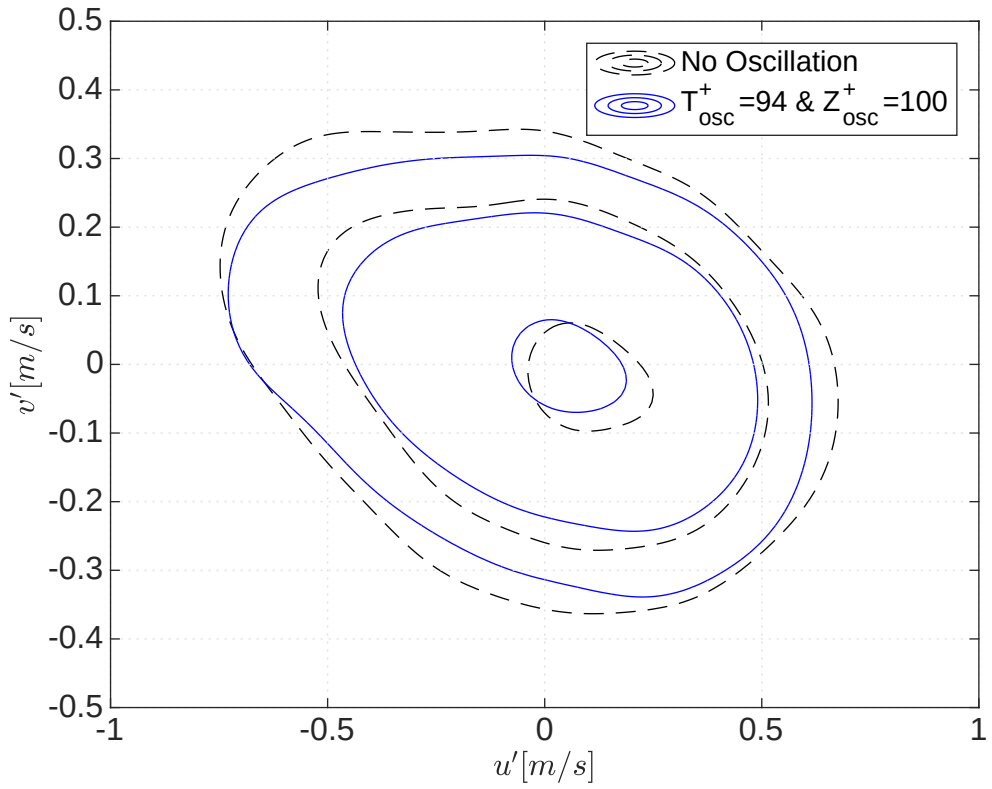

Figure 6.15: Quadrant decomposition PDF indicating the the 10,70 and 90% of maximum probability level at $y^+ = 10$)

The contours of joint PDF of u' and v' for contour levels indicating 10, 70 and 90% levels show that the oscillations tend to compress the contour. supporting what is observed in the one dimensional PDF explained earlier. Though the literature suggests that the contours will be tilted horizontally when compared to the base flow. But the results were obtained for higher wall velocities(W_m^+) and much higher reductions in drag were obtained. The mechanism at work can be explained as follows, the spanwise oscillations force the streaks to turn due to the additional vorticity from the spanwise oscillations, therefore not providing the necessary time for the quasi-streamwise vortices to lift and produce the ejection and sweep events that are vital to the cycle of turbulence production. The two-dimensional quadrant decomposition of these velocity fluctuations provides a more detailed perspective of the mechanism at play.

6.4. Instantaneous flow organization

Quantitative data on the slope of the streamwise velocity at the wall, the trends associated with the Reynolds shear stress and turbulent kinetic energy all indicate that spanwise wall oscillations at the right oscillating frequency and amplitude produce skin-friction reduction. Therefore, can the effects of oscillation also be seen qualitatively by analyzing the instantaneous flow organization of the full field. The data of the TBL at $Re_\theta = 1000$ with($T^+_{osc} = 94, Z^+_{osc} = 100$) and without oscillation is used. Vorticity contours and quiver plots are used to observe if there is a reduction in hairpin packet signature, the technique used for detecting hairpin packet signature is detailed by Adrian R.J.

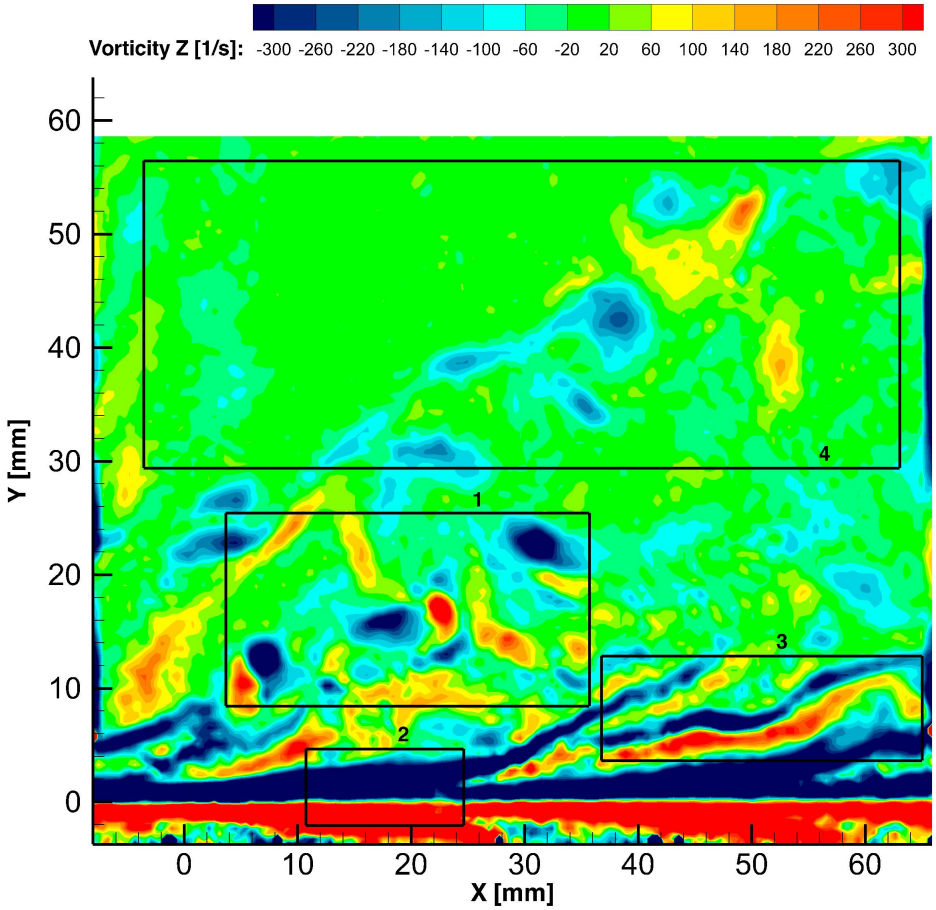

Figure 6.16: Instentaneous vorticity field for $Re_\theta = 1000$, with the 4 discernible structures

6.4.1. Vorticity

Vorticity fields provide insight into the structures that are present, although planar measurements have been performed, vorticity fields in the spanwise axis can be generated. As discussed in Chapter-4, signatures of many of the coherent structures can be identified in the vorticity fields. It is also import to note that in the current case vorticity(ω_z) is calculated as $\frac{\partial v}{\partial x} - \frac{\partial u}{\partial y}$. The boundary layer is already a region of shear, due to which there is

background vorticity that is already present but the vorticity of these structures are higher can be observed in Fig-6.16.

The structures numbered in Fig-6.16 are described as follows.

- 1: The heads of hairpins depicted by strong negative vorticity and they are inclined at an angle between 25-45°. The region enclosed in the rectangle contains a hairpin packet, which is consecutive hairpins that are generated. Figure-1.3 gives a three-dimensional visualization of the same.
- 2: The viscous sublayer, where the shear is the highest as the velocity increases from zero at the wall.
- 3: Inclined vorticity structures, can be due to ejections from near the wall. The fluid in the viscous sublayer being lifted between the legs of the horseshoe.
- 4: Vorticity signatures in the outer regions of the boundary layer.

These are some of the structures that are commonly observed in the vorticity fields analysed. Based on these 4 structures the fields with and without oscillation are compared to see if visual inspection can shed some additional information. The 200 vorticity fields obtained for the non-oscillating case and the oscillations at $T^+_{osc} = 94$ and $z^+_{osc} = 100$ at $Re_\theta = 1000$ have been qualitatively compared.

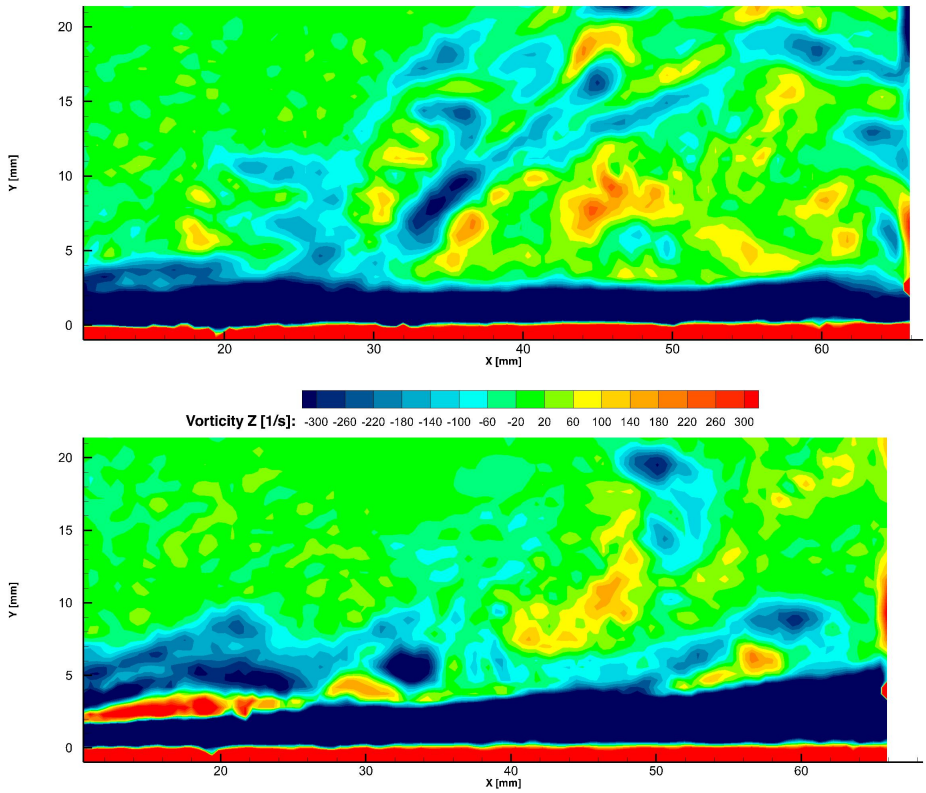

Figure 6.17: Instantaneous vorticity near the wall, oscillations (Top) and no oscillations (Bottom) oscillation

It can be observed in most of the vorticity fields (Figure-6.17) that the thickness of the viscous sublayer has increased when the plate oscillates. This can also be observed in the inner scaled velocity profile of the boundary layer. Although not quantified, the structures numbered 4 in the list which are vorticity spots in the outer layer present due to the ejections near the wall are reduced in when the wall oscillates.

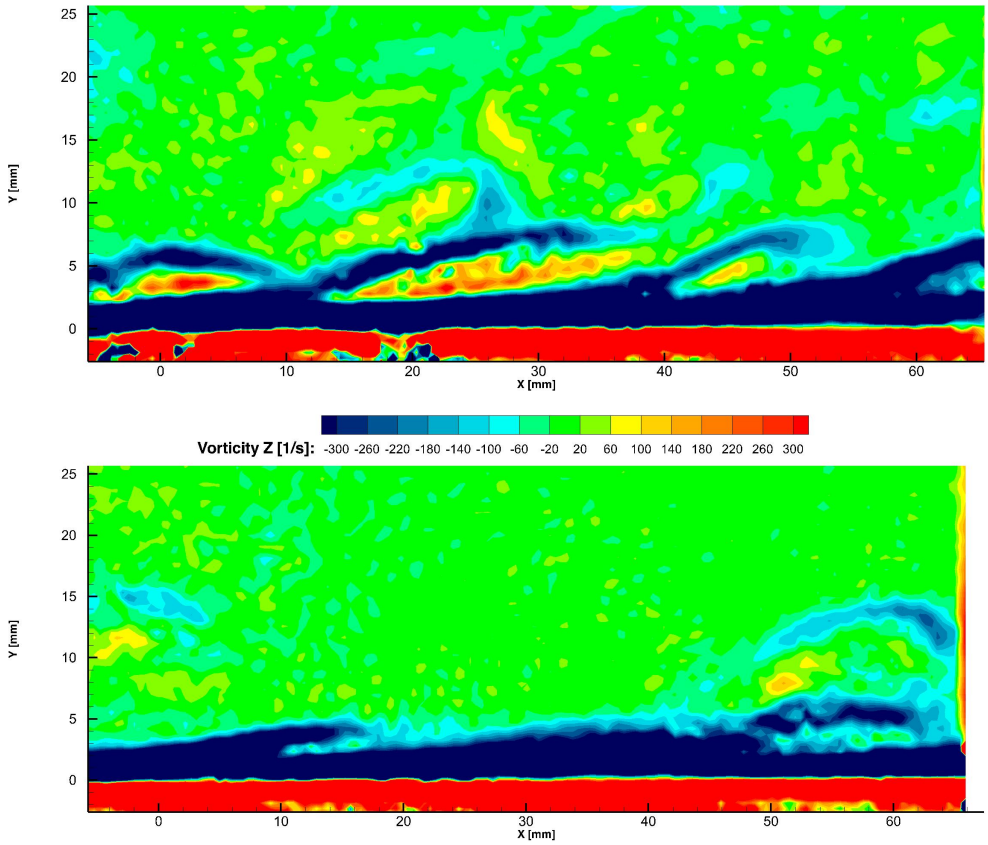

Figure 6.18: Orientation of hairpin legs, oscillations (Top) and no oscillations (Bottom) oscillation

Structures 3 are observed in both the cases, but the inclination of the vortex structures are reduced when the plate oscillates. This can be explained due to the reduction in wall-normal fluctuations, indicating that the wall-normal variations which are very essential to maintain the turbulence cascade are diminished. The hairpin vortex signatures, on the other hand, are observed in both the cases and a clear distinction cannot be made the two cases. Therefore, quantities such as Reynolds stress, TKE production provide a better understanding than the planar signature.

6.5. Discussions

From the results described above, it is clear that spanwise wall oscillations do indeed lead to a reduction in skin-friction drag as already reported in the literature. The reductions obtained agree well with the reductions reported in literature through DNS studies, although a large range of data could not be investigated to ascertain the dependence of the parameters, Planar PIV as a measurement technique is deemed suitable to quantify the reductions in skin friction through near-wall measurements.

After a review of the literature, the mechanism at play can be described as follows. In a fully developed turbulent boundary layer, there are quasi-organized structures (streaks) which play a vital role in sustaining the production of turbulence. There are many schools of thought which explain the presence of these structures, first being that there are streamwise vortices which are present near the wall which leads to the formation of the streaks and production of turbulence (Jiménez and Pinelli, 1999). Second, being that these streamwise vortices are viewed as the legs of the horseshoe vortex described earlier (Adrian et al., 2000). The third view is that a regeneration cycle where the streaks become unstable and lead to the creation of these vortical structures. These vortical structures then regenerate the streaks and this cycle continues (Hamilton et al., 1995). The presence of streaks as the main driver is said to be more prominent at higher Reynolds number and hairpins/horseshoes are more at the lower Reynolds number flows (Schlatter et al., 2014), But Jodai and Elsinga (2016) stated that both structures are observed at all Reynolds number and it cannot be attributed to one alone. Spanwise oscillation diminishes the effect of these quasi-organized structures by creating additional vorticity by setting up the stokes layer which does not allow the necessary time for these streaks to lift and produce the necessary ejections and sweep events.

With the low-speed planar data obtained in the current experimental campaign, it is difficult to visualize the response of these structures, rather only a statistical analysis in the form of Reynolds stresses, TKE production and quadrant decomposition can be performed. In the current experimental campaign $T^+_{osc} = 94$ is reached which is close to the optimum reported in the literature, this condition has been used as the basis for all comparison of the data. Cases which have increased drag have also been studied to obtain a complete understanding.

7

Conclusions and recommendations

In this chapter, the overall conclusions are drawn based on the findings of the current experimental campaign followed by recommendations for future research to help understand the physics of the fluid in response to spanwise wall oscillation.

7.1. Conclusions

The research performed was undertaken to study the suitability of PIV for the measurement of skin friction drag. PIV is currently the most common experimental technique employed for fluid flow in many industries and academia. Also, turbulent skin-friction contributes to a major share to the energy expenditure in the field of aviation, fluid transport and many others. Therefore to understand the relevance of the study the following research question was posed.

"Understand and quantify experimentally the reduction of turbulent skin-friction drag produced due to spanwise wall oscillation using Planar PIV"

To answer this, a detailed study on the fundamentals of turbulent boundary layers, with attention being paid to the scaling, empirical relations are performed. Followed by a study on the coherent structures in the TBL, which play an important role in the sustenance of turbulence in wall-bounded flows. The various schools of thought which describe these events are also looked at. The literature on techniques which reduce turbulent skin friction drag has been analyzed, with special attention being given to spanwise oscillations. The literature reviewed lead to the design of an experimental setup capable of achieving the research objective. The setup was manufactured to oscillate a section of a flat plate of length $0.4m$ up to a frequency of $15Hz$ and peak to peak amplitude of $10mm$, the oscillating section was downstream of a flat plat plate TBL tripped using LEGO blocks. An experimental campaign using planar PIV is performed. Velocity vectors at a resolution of 0.0872 mm/vector is obtained, these high-resolution measurements aid in the measurement of the slope of the mean streamwise velocity near the wall. Reductions in skin friction of 14.63% is obtained at T^+_{osc} = 94 and Z^+_{osc} = 100. Reynolds shear stress is reduced as a result of favourable wall oscillations, whereas a slight increase is for the unfavourable case. The stokes layer setup due to oscillations corresponding to a T^+_{osc} = 700 penetrate the log layer thus causing more disturbance than desired. Turbulence production is reduced considerably when the wall oscillates. This further strengthens the argument that

wall oscillations prevent the streaks to lift i.e. there is not enough time for them to lift. As a consequence of which the fluctuations are reduced. Quadrant decomposition and PDF of the fluctuations (u', v') are analyzed and they corroborate the explanation provided.

Apart from statistical data, PIV provides velocity fields at different acquisition times. With this data, instantaneous flow organization is qualitatively analyzed. Structures like hairpin packet signatures, ejections and vortical structures in the outer layer are observed. Reductions in structures in the outer layer are discerned. But more detailed conclusions could not be obtained from qualitative data because it was low speed and planar data.

In conclusion, the objectives stated earlier have been achieved. Reductions in skin-friction have been quantified, using the desired techniques with the limitations of each reported. Trends of derived quantities elaborated and a good understanding of the current state of literature is obtained. With future research in mind, more points of investigations have been arrived at. The research performed has opened up many questions which need to be answered in future studies.

7.2. Recommendations

In the course of the thesis, several additional ideas and questions have been developed which needs to be further studied. With the current setup, it is possible to achieve an optimum $T^+_{osc} = 100$ for $Re_\theta = 1000$, where maximum drag reductions are obtained. Time-resolved measurements can be performed over the length of the plate. These measurements will provide a better insight into the instantaneous flow organization which could not be obtained from the low-speed measurements of the current campaign. The measurements were only performed in the x-y plane, but more details on the behaviour of the streaks could be obtained by performing the experiment in the x-z plane at different wall-normal distances.

3D Tomographic PIV will provide more quantitative and qualitative data on the response of the vortical structures to the wall oscillations in 3-dimensions. The maximum drag reductions recorded in literature is said to be dependent on the Reynolds number of the flow. As the Re_θ is increased the maximum reduction is lowered and is reported to be due to the effect of the outer scaled structures on the smaller scales (Touber and Leschziner, 2012). But to be able to perform experiments at higher Reynolds number the use of mechanical systems is not feasible as required oscillation frequency is high. The alternative in the form of dielectric barrier discharge plasma actuators can be implemented to perform experimental studies at these elevated Reynolds numbers.

In the author's opinion, the focus of future research on turbulent drag reduction should be more on understanding the fundamentals as to why a technique is effective rather than on optimizing the reductions. This understanding when obtained can be used to design more efficient techniques using passive means. Importance should also be placed on understanding advances already made in literature, so that future work can look to add additional insights.

A

Momentum deficit analysis

As discussed in Section-5.8, adopted a methodology to compute the deficit in momentum between the inlet and the outlet profile (Figure-5.9) from the planar measurements. The technique, however, did not provide results which supported the findings from that of near-wall measurements. This was attributed to the following reasons.

1. The outer edge of the boundary layer profile was not captured in the field of view.
2. Simultaneous acquisition of the inlet and the outlet profile was not made.

Due to the unavailability of the edge of the boundary layer profile, the control volume (CV) would need to be altered. The upper surface of the CV which was assumed to be void of any shear stress due to the free stream velocity being constant is not valid. Leading to the results being very sensitive to the height of the CV adopted. Some results for the flow condition at $Re_\theta = 1000$ are depicted. A brief description of the procedure is as follows.

- First for a given inlet boundary layer height(δ_1), corresponding outlet BL height is determined by using conservation of mass.
- Following this the deficit in momentum is calculated.
- Difference in the deficit between the oscillated and non-oscillated case is used to estimate the skin-friction reduction.

The results obtained for two chosen inlet boundary layer heights $\delta_1 = 50,55mm$ at $Re_\theta = 1000$ are detailed in Tables-A.1,A.2 ,ΔM is the difference in mass between the inlet and the outlet. From the results, it is clear that the reductions are sensitive to inlet height. Positive reductions are obtained for the optimum case, but any conclusions drawn from this momentum deficit study detailed is questionable. Therefore another alternate approach is adopted, where the difference in momentum of the boundary layer profile at the "over plate" location (Figure-5.9) is compared for the plate with and without oscillations. The trends obtained for this case should be similar to that obtained for the near-wall measurements (Figure-6.5). The deficit is calculated as the difference in momentum, where osc is for the oscillated profile and $nosc$ is for the non-oscillated case.

$$\Delta M = \rho\Big(\int_0^\delta u_{osc}^2(y)\,dy - \int_0^\delta u_{nosc}^2(y)\,dy\Big)$$

T^+_{osc}	A^+_{osc}	D.R(%)	$\Delta M[\frac{Kgm}{s^2}]$	$\delta_2[mm]$
95 (15Hz)	100 (10 mm)	+4.12	2.3×10^{-4}	50.4366
107 (13Hz)		-12.73	4.86×10^{-4}	50.4009
140 (10Hz)		-0.53	3.15×10^{-4}	50.4417
175 (8Hz)		-1.22	2.91×10^{-4}	50.4557
350 (4Hz)		-18.50	2.32×10^{-4}	50.6114
700 (2Hz)		-6.19	3.97×10^{-5}	50.4027

Table A.1: Drag reductions obtained from momentum deficit analysis ('+' indicates reduction) for $\delta_1 = 50mm$

T^+_{osc}	A^+_{osc}	D.R(%)	$\Delta M[\frac{Kgm}{s^2}]$	$\delta_2[mm]$
95 (15Hz)	100 (10 mm)	+4.47	2.2×10^{-4}	55.364
107 (13Hz)		-0.69	1.64×10^{-4}	55.4410
140 (10Hz)		+0.70	2.411×10^{-4}	55.3698
175 (8Hz)		-2.40	2.9×10^{-4}	55.3838
350 (4Hz)		-22.00	3.1×10^{-4}	55.5395
700 (2Hz)		-8.44	4.4×10^{-5}	55.3308

Table A.2: Drag reductions obtained from momentum deficit analysis ('+' indicates reduction) for $\delta_1 = 55mm$

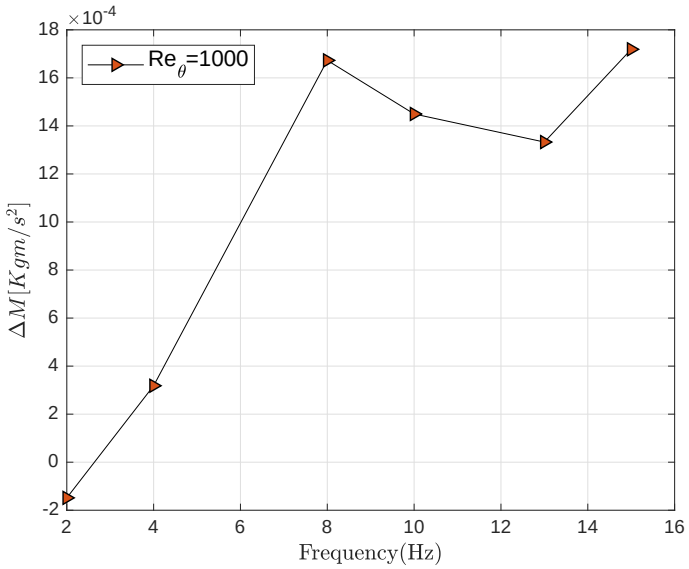

Figure A.1: Difference in the momentum between the oscillated and non oscillated profiles

The trend observed in Figure-A.1, are similar to that of near-wall measurements. But more detailed analysis is required to be performed.

B

Near wall vorticity contours

The near wall vorticity plots for all the frames are attached as a movie for reference, the oscillation conditions are also mentioned in the following movies.

(Loading 0Hz.gif)

Figure B.1: No Oscillations

(Loading 15Hz.gif)

Figure B.2: Oscillations $T^+_{osc} = 94, Z^+_{osc} = 100$

Bibliography

Ronald J Adrian. Hairpin vortex organization in wall turbulence. *Physics of Fluids*, 19(4): 041301, 2007.

Ronald J Adrian, Carl D Meinhart, and Christopher D Tomkins. Vortex organization in the outer region of the turbulent boundary layer. *Journal of fluid Mechanics*, 422:1–54, 2000.

John David Anderson Jr. *Fundamentals of aerodynamics*. Tata McGraw-Hill Education, 2010.

Arturo Baron and Maurizio Quadrio. Turbulent drag reduction by spanwise wall oscillations. *Applied Scientific Research*, 55(4):311–326, 1995.

DW Bechert, M Bruse, W vd Hage, JG Th Van der Hoeven, and G Hoppe. Experiments on drag-reducing surfaces and their optimization with an adjustable geometry. *Journal of fluid mechanics*, 338:59–87, 1997.

P Bradshaw and NS Pontikos. Measurements in the turbulent boundary layer on an 'infinite'swept wing. *Journal of Fluid Mechanics*, 159:105–130, 1985.

Yunus A Cengel. *Fluid mechanics*. Tata McGraw-Hill Education, 2010.

Jung-Il Choi, Chun-Xiao Xu, and Hyung Jin Sung. Drag reduction by spanwise wall oscillation in wall-bounded turbulent flows. *AIAA journal*, 40(5):842–850, 2002.

Kwing-So Choi, Jean-Robert DeBisschop, and Brian R Clayton. Turbulent boundary-layer control by means of spanwise-wall oscillation. *AIAA journal*, 36(7):1157–1163, 1998.

Kwing-So Choi, Timothy Jukes, and Richard Whalley. Turbulent boundary-layer control with plasma actuators. *Philosophical Transactions of the Royal Society A: Mathematical, Physical and Engineering Sciences*, 369(1940):1443–1458, 2011.

Thomas C Corke and Flint O Thomas. Active and passive turbulent boundary-layer drag reduction. *AIAA Journal*, 56(10):3835–3847, 2018.

Thomas C Corke, Y Guezennec, and Hassan M Nagib. Modification in drag of turbulent boundary layers resulting from manipulation of large-scale structures. 1981.

PA Davidson. Turbulence. an introduction for scientists and engineers oxford university press, 2004.

AP Dowling. The effect of large-eddy breakup devices on oncoming vorticity. *Journal of Fluid Mechanics*, 160:447–463, 1985.

David M Driver and Sheshagiri K Hebbar. Experimental study of a three-dimensional, shear-driven, turbulent boundary layer. *AIAA journal*, 25(1):35–42, 1987.

John K Eaton. Effects of mean flow three dimensionality on turbulent boundary-layer structure. *AIAA journal*, 33(11):2020–2025, 1995.

S Ersoy and JDA Walker. Viscous flow induced by counter-rotating vortices. *The Physics of fluids*, 28(9):2687–2698, 1985.

RE Falco. Coherent motions in the outer region of turbulent boundary layers. *The Physics of Fluids*, 20(10):S124–S132, 1977.

Mohamed Gad-el Hak and Ron F Blackwelder. Selective suction for controlling bursting events in a boundary layer. *AIAA journal*, 27(3):308–314, 1989.

Ricardo García-Mayoral and Javier Jiménez. Drag reduction by riblets. *Philosophical Transactions of the Royal Society A: Mathematical, Physical and Engineering Sciences*, 369 (1940):1412–1427, 2011.

Kevin Gouder, Mark Potter, and Jonathan F Morrison. Turbulent friction drag reduction using electroactive polymer and electromagnetically driven surfaces. *Experiments in fluids*, 54(1):1441, 2013.

James M Hamilton, John Kim, and Fabian Waleffe. Regeneration mechanisms of near-wall turbulence structures. *Journal of Fluid Mechanics*, 287:317–348, 1995.

Richard JA Howard and Neil D Sandham. Simulation and modelling of a skewed turbulent channel flow. *Flow, turbulence and combustion*, 65(1):83–109, 2000.

N Hutchins, JP Monty, B Ganapathisubramani, HCH Ng, and I Marusic. Three-dimensional conditional structure of a high-reynolds-number turbulent boundary layer. *Journal of Fluid Mechanics*, 673:255–285, 2011.

IATA. Future of the airline industry 2035. *URL: https://www. iata. org/policy/Documents/iata-future-airline-industry. pdf*, 2018.

H Jeff. The boeing 787 dreamliner: More than an airplane. In *Presentation to AIAA/AAAF Aircraft Noise and Emissions Reduction Symposium*, 2007.

Javier Jiménez and Alfredo Pinelli. The autonomous cycle of near-wall turbulence. *Journal of Fluid Mechanics*, 389:335–359, 1999.

Y Jodai and GE Elsinga. Experimental observation of hairpin auto-generation events in a turbulent boundary layer. *Journal of Fluid Mechanics*, 795:611–633, 2016.

WJ Jung, N Mangiavacchi, and R Akhavan. Suppression of turbulence in wall-bounded flows by high-frequency spanwise oscillations. *Physics of Fluids A: Fluid Dynamics*, 4(8): 1605–1607, 1992.

Stephen J Kline, William C Reynolds, FA Schraub, and PW Runstadler. The structure of turbulent boundary layers. *Journal of Fluid Mechanics*, 30(4):741–773, 1967.

F Laadhari, L Skandaji, and R Morel. Turbulence reduction in a boundary layer by a local spanwise oscillating surface. *Physics of Fluids*, 6(10):3218–3220, 1994.

Taegee Min and John Kim. Effects of hydrophobic surface on skin-friction drag. *Physics of Fluids*, 16(7):L55–L58, 2004.

Ronald Lee Panton. *Self-sustaining mechanisms of wall turbulence*, volume 15. Computational Mechanics, 1997.

Jeongyoung Park and Haecheon Choi. Effects of uniform blowing or suction from a spanwise slot on a turbulent boundary layer flow. *Physics of Fluids*, 11(10):3095–3105, 1999.

Maurizio Quadrio and Pierre Ricco. Critical assessment of turbulent drag reduction through spanwise wall oscillations. *Journal of Fluid Mechanics*, 521:251–271, 2004.

Markus Raffel, Christian E Willert, Fulvio Scarano, Christian J Kähler, Steve T Wereley, and Jürgen Kompenhans. *Particle image velocimetry: a practical guide*. Springer, 2018.

Ruben Rathnasingham and Kenneth S Breuer. Active control of turbulent boundary layers. *Journal of Fluid Mechanics*, 495:209–233, 2003.

Pierre Ricco and Shengli Wu. On the effects of lateral wall oscillations on a turbulent boundary layer. *Experimental Thermal and Fluid Science*, 29(1):41–52, 2004.

Stephen K Robinson. Coherent motions in the turbulent boundary layer. *Annual Review of Fluid Mechanics*, 23(1):601–639, 1991.

AM Savill and JC Mumford. Manipulation of turbulent boundary layers by outer-layer devices: skin-friction and flow-visualization results. *Journal of Fluid Mechanics*, 191:389–418, 1988.

Philipp Schlatter and Ramis Örlü. Assessment of direct numerical simulation data of turbulent boundary layers. *Journal of Fluid Mechanics*, 659:116–126, 2010.

Philipp Schlatter, Q Li, Ramis Örlü, Fazle Hussain, and Dan Stefan Henningson. On the near-wall vortical structures at moderate reynolds numbers. *European Journal of Mechanics-B/Fluids*, 48:75–93, 2014.

Hermann Schlichting and Klaus Gersten. *Boundary-layer theory*. Springer, 2016.

G Schrauf. Status and perspectives of laminar flow. *The aeronautical journal*, 109(1102): 639–644, 2005.

Olav Sendstad. *The near wall mechanics of three-dimensional turbulent boundary layers*. Stanford University, 1992.

SESAR. Exploring the boundaries of air traffic management, a summary of sesar exploratory research results. 2018.

William Sheridan, Michael McCune, and Michael Winter. Geared turbofan™ engine: Driven by innovation. *Encyclopedia of Aerospace Engineering*, pages 1–7, 2010.

Martin Skote. Temporal and spatial transients in turbulent boundary layer flow over an oscillating wall. *International Journal of Heat and Fluid Flow*, 38:1–12, 2012.

CR Smith, JDA Walker, AH Haidari, and BK Taylor. Hairpin vortices in turbulent boundary layers: the implications for reducing surface drag. In *Structure of Turbulence and Drag Reduction*, pages 51–58. Springer, 1990.

Theodore Theodorsen. Mechanisms of turbulence. 1952.

Emile Touber and Michael A Leschziner. Near-wall streak modification by spanwise oscillatory wall motion and drag-reduction mechanisms. *Journal of Fluid Mechanics*, 693: 150–200, 2012.

Steven Trujillo, David Bogard, Kenneth Ball, Steven Trujillo, David Bogard, and Kenneth Ball. Turbulent boundary layer drag reduction using an oscillating wall. In *4th Shear Flow Control Conference*, page 1870, 1997.

Olaf W van Campenhout, Michiel van Nesselrooij, Leo L Veldhuis, Bas van Oudheusden, and Ferry Schrijer. An experimental investigation into the flow mechanics of dimpled surfaces in turbulent boundary layers. In *2018 AIAA Aerospace Sciences Meeting*, page 2062, 2018.

M Van Nesselrooij, LLM Veldhuis, BW Van Oudheusden, and FFJ Schrijer. Drag reduction by means of dimpled surfaces in turbulent boundary layers. *Experiments in Fluids*, 57 (9):142, 2016.

B.W. van Oudheusden. Lecture notes in Viscous Flows, November 2017.

Leo Veldhuis and Erik Vervoort. Drag effect of a dented surface in a turbulent flow. In *27th AIAA Applied Aerodynamics Conference*, page 3950, 2009.

CM White, VSR Somandepalli, and MG Mungal. The turbulence structure of drag-reduced boundary layer flow. *Experiments in fluids*, 36(1):62–69, 2004.

Indra Yudhistira and Martin Skote. Direct numerical simulation of a turbulent boundary layer over an oscillating wall. *Journal of Turbulence*, (12):N9, 2011.